



HAL
open science

Functionalization of epitaxial graphene by metal intercalation and molecules

Maya Narayanan Nair

► **To cite this version:**

Maya Narayanan Nair. Functionalization of epitaxial graphene by metal intercalation and molecules. Other [cond-mat.other]. Université de Haute Alsace - Mulhouse, 2013. English. NNT : 2013MULH4133 . tel-01064523

HAL Id: tel-01064523

<https://theses.hal.science/tel-01064523>

Submitted on 16 Sep 2014

HAL is a multi-disciplinary open access archive for the deposit and dissemination of scientific research documents, whether they are published or not. The documents may come from teaching and research institutions in France or abroad, or from public or private research centers.

L'archive ouverte pluridisciplinaire **HAL**, est destinée au dépôt et à la diffusion de documents scientifiques de niveau recherche, publiés ou non, émanant des établissements d'enseignement et de recherche français ou étrangers, des laboratoires publics ou privés.

UNIVERSITE DE HAUTE ALSACE

2013

THESE

Présentée pour l'obtention du grade de

DOCTEUR DE L'UNIVERSITE DE HAUTE ALSACE

par

Maya NARAYANAN NAIR

**Functionalization of epitaxial graphene
by metal intercalation and molecules**

UMR n°7361

Institut de Sciences des Matériaux de Mulhouse

Soutenue le 24 Septembre 2013

devant la commission d'examen composée de :

Rapporteur	Pr T. ANGOT	Prof à l'université d'Aix-Marseille, Marseille
Rapporteur	Dr B. GREVIN	Chargé de recherche, CNRS, CEA, INAC, Grenoble
Examineur	Dr A. LOISEAU	Directrice de Recherche, CNRS, LEM, Chatillon
Directeur de thèse	Dr L. SIMON	Directeur de recherche, CNRS, IS2M, Mulhouse
Co-directeur de thèse	Dr J. P. MALVAL	Maître de conférences, UHA, IS2M, Mulhouse

Acknowledgements

Acknowledgements

I am really thankful to Dr. Cathie Vix, director of Institut de Science des Matériaux de Mulhouse , for giving me an opportunity to work in this laboratory.

I would like to thank my thesis committee: Prof. Thierry Angot, Professeur à l'université d'Aix-Marseille, Dr. Benjamin Grevin, Chargé de recherche, CNRS, CEA, INAC, Grenoble, and Dr. Annick Loiseau, Directrice de Recherche, LEM, CNRS, Onera for kindly agreed to be as reporters and reviewer of this thesis despite their other professional commitments.

I would like to express my sincere gratitude to my supervisor Dr. Laurent Simon for providing me an opportunity to join in his research group. This dissertation would not have been possible without his motivation, encouragement, guidance and support. I really thank him for his excellent supervision and many fruitful discussions that helped me to understand the complex physics. Also I really wanted to thank him for being an awesome mentor.

I also sincerely thank to Dr. Jean-Pierre Malval, my second supervisor for his great support and help in photo physical measurements that used in this thesis work. Also I really thank him for his timely effort to correct my thesis.

I wish to thank my dearest colleague and pedagogic tutor Dr. Dominique Aubel for his continued support on both professionally and personally for the past three years of my research life. Also I am really thankful to other colleagues Dr. Marion Cranney and Dr. Francois Vonau for sharing with me their practical knowledge in working with Scanning Tunneling Microscopy (STM).

Also I take this opportunity to thank all our collaborators; especially I am really grateful to Dr. Marie-Laure Bocquet, ENS Lyon for providing us the calculated STM images. I am really thankful to Dr. Françoise Serein-Spirau, Dr. Jean-Pierre Lère-Porte from Institut Charles

Acknowledgements

Gerhardt, Ecole Nationale Supérieure de Chimie de Montpellier and Ms. Cristina Mattioli, Dr. André Gourdon from CEMES, Toulouse for synthesizing molecules for this research work.

I would like to thank my colleague Dr. Wael Hourani for helping me to take room temperature Scanning Tunneling Microscopy (STM) measurements. Also I am really thankful to Mr. Denys Emmanuel and Mr. Florentin Alban for their technical support. My sincere appreciation to all other members in our lab.

Last but not least, my family, friends and the one above all of us, the omnipresent God, for answering my prayers and for giving me the strength, thank you so much Dear Lord.

This thesis work was financially supported by ANR ChimigraphN.

Table of contents

Table of Contents

General Introduction.....	1
1. Introduction.....	5
1.1. Graphene.....	5
1.2. Band structure of Graphene.....	6
1.3. Synthesis of graphene.....	9
1.3.1. Mechanical exfoliation from graphite.....	9
1.3.2. Reduction of graphene oxide.....	9
1.3.3. Chemical vapor deposition (CVD) on metal substrates.....	9
1.3.4. Epitaxial growth on Silicon Carbide (SiC).....	10
1.4. Defects in Graphene.....	11
1.5. Metal intercalations on Graphene.....	11
1.5.1. Graphite intercalations.....	12
1.5.2. Intercalations of metals on graphene on metals.....	13
1.5.3. Metals intercalation on Epitaxial Graphene (EG).....	14
1.6. Challenges.....	15
1.7. Goal and strategy of the work.....	16
2. Experimental Techniques.....	19
2.1 Scanning Tunneling Microscopy (STM).....	19
2.1.1 Basic Theory of STM.....	20
2.1.2 Principles of operation.....	26
2.1.3. Measurement types.....	28
2.1.4. Measurement of dI/dV using lock-in amplifier.....	30
2.2. Photoelectron Spectroscopy (PES).....	32
2.2.1. Principle of photoelectron spectroscopy (PES).....	33

Table of contents

2.2.2. Angle resolved Photoemission spectroscopy (ARPES).....	36
2.2.3. X-ray photoelectron spectroscopy (XPS)	40
2.2.4. Experimental set up.....	42
2.3. One-Photon (1PA) and Two-Photon (2PA) Absorption techniques.....	45
2.3.1. UV-Visible absorption spectroscopy	45
2.3.2. Fluorescence spectroscopy	48
2.3.3. Two-photon absorption spectroscopy (2PA)	52
3. Intercalation of gold on Epitaxial Graphene (EG)	59
3.1. Method of gold intercalation on EG	60
3.2. Modes of gold intercalation on EG.....	60
3.3. Characterization of film phase (FP)	62
3.4. Characterization of diluted phase (DP).....	65
3.5. Position and number of intercalated Au atoms.....	66
3.6. Scanning Tunneling Spectroscopy (STS) measurements on ML, DP and FP	69
3.7. Free standing nature of intercalated gold clusters	70
3.7.1. Differential charge density	71
3.7.2. Projected Density of States (PDOS).....	71
3.7.3. X-ray photoelectron spectroscopy (XPS)	72
3.8. Standing wave patterns on diluted phase (DP)	81
3.8.1. Joint Density of States (JDOS)	85
3.9. ARPES measurements on Pristine and Gold intercalated graphene.....	88
3.9.1. VFs extension, effective mass enhancement and superconductivity	93
3.10. Decoupling of monolayer graphene by intercalated gold clusters.....	101
3.10.1. Roughness analysis	101
3.10.2. Calculation of charge transfer.....	102
3.11. Conclusion	105

Table of contents

4. Molecules on Epitaxial Graphene (EG)	108
4.1. TTFm molecules on Epitaxial graphene	108
4.1.1. TTFm molecules on pristine epitaxial graphene on SiC(0001)	111
4.1.2. TTFm molecules on gold intercalated epitaxial graphene on SiC (0001).....	117
4.1.3. TTFm molecules on graphite	119
4.2. Photochromic molecules on graphene.....	120
4.2.1. Diarylethene molecules.....	121
4.2.2. TBT-diarylethene-TBT (FC62) molecules.....	124
4.3. Conclusion	130
5. Photophysical properties of molecules	132
5.1. Photophysical properties of an oligothiophene series	132
5.1.1 Ground state properties of an Oligo (phenylenethienylene) s series	133
5.1.2 Fluorescence properties of nTBT : Dependence on Solvent and Temperature.	142
5.1.3. Two-photon absorption (2PA) measurements.....	146
5.1.4. Conclusion	149
5.2. Photophysical properties of TBT-Switch-TBT (FC62).....	150
5.3. Conclusion	153
Summary	154
References	156

General Introduction

General Introduction

Graphene is a zero gap semiconductor material with outstanding properties such as high carrier mobilities, massless charge carriers, chemically inert, high thermal conductivity, the thinnest material ever made still visible to naked eye and the strongest material than all allotropes of carbon [1, 6 and 16]. Owing to these peculiar properties, graphene is a most promising material for the nanotechnology applications and the subject for intense research.

Graphene can be synthesized in different ways such as mechanical exfoliation from graphite [16], reduction of graphene oxide [17,18], chemical vapor deposition (CVD) of hydrocarbons on transition metal surfaces [19,20], epitaxial growth on silicon carbide (SiC) [51-54], unzipping carbon nanotubes [13,14], dispersion of graphite in organic solvents [15]. Among all these techniques, epitaxial growth of graphene layer on SiC substrate deserves more attention, due to its large scale production and uniform graphene layers and its high charge carrier mobilities of up to $20000\text{cm}^2/\text{V.s}$. Moreover, epitaxial graphene (EG) is intrinsically n doped due to the charge transfer from the substrate.

Due to the interaction with the substrate and the n-type doping, several strategies have been involved to modify the position of the Fermi level by doping with an external source, or by decoupling the graphene from its substrate. First studies on graphene demonstrated that the deposition of metal is able to modify the position of the Fermi level. This charge transfer was historically and widely studied for graphite intercalation, or intercalation in nanotube of even C60. Finally and logically, intercalation of metals was also observed for EG on metallic substrates and EG grown on SiC substrates as discussed in chapter1. Intercalants have the ability not only to decouple the graphene layer from the substrate, but also to functionalize the graphene layer while preserving its inherent properties. This is the main context of this thesis work. In chapter 2, we describe the experimental techniques used in this thesis, Scanning Tunneling Microscopy (STM) and spectroscopy (STS), and photoemission spectroscopy measurement techniques such as X-ray photoelectron spectroscopy (XPS) and Angle-resolved photoemission spectroscopy

General Introduction

(ARPES). In the last part of this chapter, the method of optical characterization (absorption, fluorescence, two photon absorption) will be also described. In chapter 3, we discuss the of intercalation of gold on EG grown on SiC(0001) and evidenced different gold intercalated structures. A detailed study of one of these gold intercalated structures called diluted phase (DP) which consists of an aggregates of individual atoms is performed. By using Angle-resolved photoemission spectroscopy (ARPES), we show that these intercalated atoms preserve the linear dispersion of quasiparticles of graphene and increase their Fermi velocities. They also strongly modify the band structure around the Van Hove singularities with a charge transfer, which is compensated by a renormalization of the Fermi velocity around the Dirac point. These results will give a new insight on the role of intercalants in the renormalization of the bare electronic band structure of graphene usually observed in graphite and graphene intercalation compounds. Extend to this research, to obtain an extended Van Hove singularity, as such a strong Van Hove extension is associated to a superconducting property and an increase in the critical temperature, in the frame work of graphite intercalation compounds, we have studied “Graphene Based Hybrid Structure” where the graphene is functionalized on both sides. On one side the band structure is modified, on the other side we have used donor molecules for an over doping. We have studied the deposition of TetraThiofullvalene (TTF) molecules which are highly electron donor, on gold intercalated graphene. This is the object of the chapter 4. The dependence of charge transfer of these molecules with their conformation is discussed. The role of the lateral alkyl chain, their interdigitation and the balance with the molecule-substrate interaction is discussed in this chapter. In the last part of this chapter, we discuss the reactivity of photochromic molecules along with the conjugated one on graphene. Also studied the structural properties of these conjugated molecules and photochromic molecules along with the conjugated one using photophysical measurements, discussed in chapter 5.

Abstract: Chapter 1. Introduction

Ce chapitre introduit les propriétés physiques du graphène, la structure de bande et les différentes méthodes de synthèse, telles que l'exfoliation mécanique à partir de graphite, la réduction de graphène oxydé, les méthodes de dépôt CVD sur des substrats métalliques, ou à partir de substrat de carbure de silicium. Il est présenté une revue bibliographique complète sur l'état de l'art dans les processus d'intercalation de métaux sous des couches de graphène différemment supportées et les enjeux et perspectives dans lequel ce travail de recherche s'est vu projeté.

1. Introduction

This chapter presents the basics of graphene which include band structure, synthesis, defects and then it discusses graphite intercalations, intercalation of metals on graphene on metallic substrate and epitaxial graphene grown on silicon carbide substrate. Finally it concludes with main challenges in the field of graphene and also the goal and strategy of this thesis work.

1.1. Graphene

Graphene-a single layer of carbon atoms arranged in a honeycomb lattice-is an ideal candidate for the next generation of nanoelectronic devices. Graphene can be wrapped up into 0D fullerenes, rolled into 1D nanotubes or stacked into 3D graphite. This truly two-dimensional material possesses high crystalline quality and unusual electronic properties such as zero band gap and its charge carriers are massless relativistic quasiparticles with an effective speed of light, also known to be thermodynamically stable under ambient conditions [1]. In 1947, Wallace first introduced graphene as a theoretical model for three-dimensional graphite [2]. After 40 years, Semenoff, Divincenzo and Mele point out theoretically the massless nature of charge carriers in graphene [3, 4]. In 1987, Mouras and co-workers first mentioned the name “graphene” to describe the graphite intercalation compounds (GICs) and the term has been used extensively in the work of carbon nanotubes. Although known as an integral part of 3D materials, graphene was presumed not to exist in the free state. This is because for long years, it was believed that 2D crystals were thermodynamically unstable and could not exist [5]. However, in 2003, Geim and Novoselov succeeded in producing the first isolated graphene flakes which lead to a drastic revolution in this field and they were awarded the 2010 Nobel Prize in physics.

1.2. Band structure of Graphene

The carbon atom in graphene has six electrons in which two electrons are lying in the inner shell and the other four electrons occupy the outer shell of 2s and 2p orbitals. The three out of four valence electrons i.e. one 2s and two 2p electrons ($2p_x$ and $2p_y$) make three sp^2 -hybridized planar orbitals that connect three neighbouring atoms through strong in-plane σ bonds. These σ bonds are responsible for the rigidity of graphene sheets. The fourth electron in out of plane $2p_z$ orbital form π bond with neighbouring carbon atoms. These π electrons are delocalized over the whole structure and responsible for the electrical conductivity in graphene.

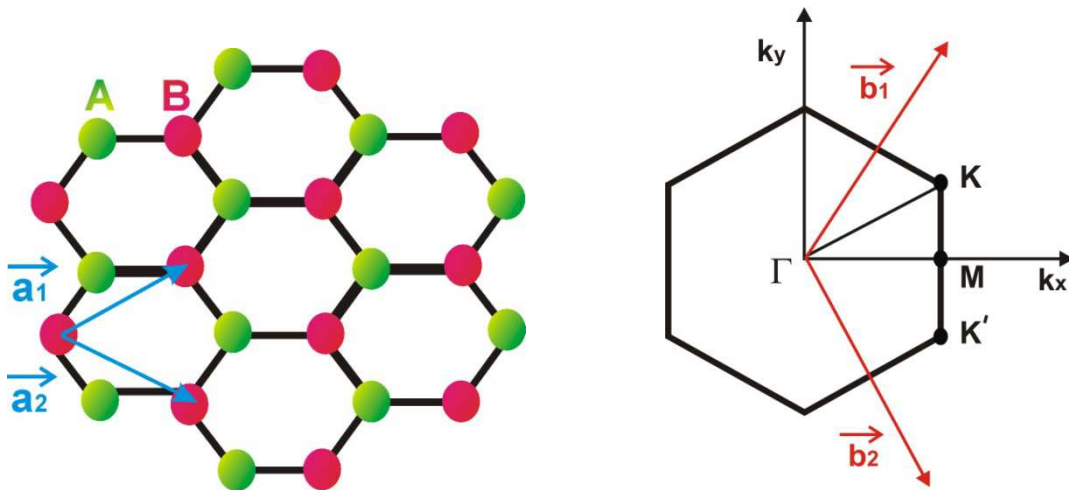


Figure.1.1: Honeycomb lattice structure of graphene (left) and its corresponding Brillouin zone (right). The unit cell lattice vectors of the real space ($\mathbf{a}_1, \mathbf{a}_2$) and the reciprocal space ($\mathbf{b}_1, \mathbf{b}_2$) are remarked.

Graphene's honeycomb lattice consists of two equivalent triangular sublattices A and B as shown in Figure 1.1. The lattice vectors can be written as

$$\mathbf{a}_1 = \frac{a}{2}(3, \sqrt{3}) \text{ and } \mathbf{a}_2 = \frac{a}{2}(3, -\sqrt{3}) \quad (\text{Eq.1.1})$$

where, $a \approx 1.42 \text{ \AA}$ is the carbon-carbon distance. The reciprocal lattice vectors are given by

Chapter 1.Introduction

$$\mathbf{b}_1 = \frac{2\pi}{3a}(1, \sqrt{3}) \quad \mathbf{b}_2 = \frac{2\pi}{3a}(1, -\sqrt{3}) \quad (\text{Eq.1.2})$$

The corresponding Brillouin zone of the reciprocal lattice is shown in Figure 1.1 (right). The two points K and K' are the inequivalent corners of the Brillouin zone (BZ) of graphene and are called Dirac points. These are known to play a crucial role in the electronic transport in graphene and their positions in the momentum space are given by

$$\mathbf{K} = \left(\frac{2\pi}{3a}, \frac{2\pi}{3\sqrt{3}a}\right) \quad \mathbf{K}' = \left(\frac{2\pi}{3a}, -\frac{2\pi}{3\sqrt{3}a}\right) \quad (\text{Eq.1.3})$$

The electronic band dispersion of graphene's π band was first calculated by Wallace [2], within the tight binding approximation, which leads to the following energy momentum relation [6].

$$E_{\pm}(\mathbf{K}) = \pm t\sqrt{3 + f(\mathbf{K})} - t'f(\mathbf{K}) \quad (\text{Eq.1.4})$$

$$f(\mathbf{K}) = 2 \cos(\sqrt{3}k_y a) + 4 \cos\left(\frac{\sqrt{3}}{2}k_y a\right) \cos\left(\frac{3}{2}k_x a\right)$$

where, ' \pm ' sign represent to the upper conduction (π^*) and lower valence (π) bands respectively. The parameter t (≈ 2.8 eV) is the nearest -neighbor and the parameter t' (≈ 0.1 eV) is the next nearest-neighbor hopping energy. The band structure of graphene is shown Figure 1.2.

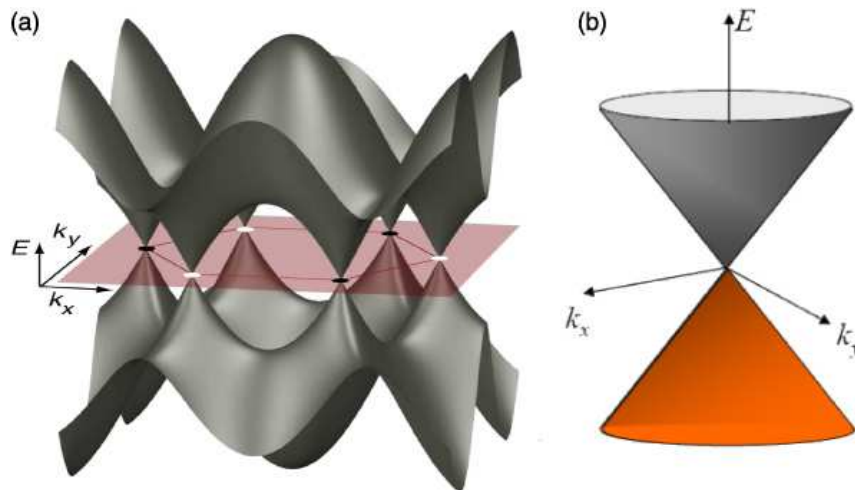


Figure.1.2: (a) shows the three dimensional electronic band structure of graphene and (b) shows the zoom of the conical dispersion around the Dirac points. Figure adapted from Andrei *et al* [7].

Chapter 1.Introduction

The valence band and conduction band meet only at the Dirac points (K, K') of the (BZ) exactly at the Fermi level. Around this crossing point the bands can be approximated by a conical dispersion as shown Figure1.2b. Hence, graphene can be described as a zero gap semiconductor. The dispersion relation (Eq.1.4) in the vicinity of the Dirac points is given by:

$$E_{\pm} = \pm\hbar V_F \mathbf{K} \quad (\text{Eq.1.5})$$

where, $V_F = \frac{3ta}{2\hbar}$ is the Fermi velocity is in the order of $\approx 1 \times 10^6$ m/s and \mathbf{K} is 2D electron wave vector relative to one of Dirac points. The \pm symbol in (Eq.1.5) corresponds to the holes and electrons respectively. From equation (1.5), we can see that the low energy dispersion relation is linear in graphene in contrast to other more conventional material (metal, semi-conductor). This means that the effective mass tends to zero. The low energy quasi-particles formally described by the Dirac-like Hamiltonian;

$$H = -i\hbar V_F \boldsymbol{\sigma} \nabla \quad (\text{Eq.1.6})$$

Where, $\boldsymbol{\sigma} = (\sigma_x, \sigma_y)$ is the vector of Pauli matrices and Fermi velocity V_F plays the role of speed of light.

In graphene, the existence of two equivalent sub-lattices A and B leads to the description of charge carriers in terms of 2D with a supplementary quantum state index σ which indicates the sub-lattice and called as pseudospin [8] for its analogy with the spin of the electron. One can further bring a quantity called chirality, which is formally a projection of pseudospin on the direction of particle's motion and is positive (negative) for electrons (holes) [5]. In other words, an electron with energy E and momentum K and holes with energy - E and momentum - K originating from the same branch of electronic spectrum have pseudospin σ pointing in the same direction, i.e. parallel to the momentum for electrons and antiparallel for holes. Pseudospin and Chirality are the two important concepts in graphene because, many electronic processes such as half integer quantum hall effect, Klein tunneling etc can be understood due to the conservation of these quantities [9-12].

1.3. Synthesis of graphene

There are several methods for the preparation of graphene such as mechanical exfoliation from graphite, reduction of graphene oxide, chemical vapor deposition (CVD) of hydrocarbons on transition metal surfaces, epitaxial growth on silicon carbide (SiC), unzipping carbon nanotubes [13,14], dispersion of graphite in organic solvents [15] . Some of the most widely employed methods are described in the following section.

1.3.1. Mechanical exfoliation from graphite

This method is also known as scotch-tape technique, first reported in 2004 [16]. Here graphene flakes are produced from bulk graphite crystals by micromechanical cleavage and these flakes are usually lateral size up to one millimetre and provide high quality. However, this method is tedious and limited to the production of graphene on large scale. It remains in the main choice for basic research.

1.3.2. Reduction of graphene oxide

This is a promising and cost effective method to obtain graphene [17-18]. According to this method, the graphite is oxidised to graphite oxide by standard oxidation process. This upon ultrasonic treatment in presence of water results in an easy exfoliation to form stable dispersions of very thin sheets of graphene oxide. The resulted monolayer of graphene oxide can be easily deposited onto various substrates. However, the chemical reduction of graphene oxide can increase its conductivity significantly though it remains very low compared to that of pristine graphene.

1.3.3. Chemical vapor deposition (CVD) on metal substrates

This is a scalable, controllable, low cost and potential technique employed in the mass production of high quality graphene. In this method, the growth of monolayer graphene usually occurs by exposure of the transition metal surface to a hydrocarbon gas under low pressure or ultra high vacuum conditions. This is a decades-old method to grow graphene [19,20] but later it has obtained particular attention as an easy way to transfer

Chapter 1.Introduction

graphene on various metallic substrates including Ir [21-24], Pd [25], Pt [26-31], Ru [26,32-35], Cu [36,37], Rh [26,38], Ni [39-50].

1.3.4. Epitaxial growth on Silicon Carbide (SiC)

The most promising approach to synthesize high quality graphene on large-scale is epitaxial growth on silicon carbide substrate. Single and multilayer graphene can be grown on both the silicon terminated SiC(0001) and the carbon terminated face SiC(000 $\bar{1}$) of SiC substrate by thermal graphitization in ultra high vacuum (UHV). When annealing the SiC substrate at high temperature silicon atoms evaporate from the surface whereas carbon atoms remain and form graphene layers [51, 52]. On SiC(000 $\bar{1}$), the interaction between graphene and substrate is weak, the number of graphene layers is much more difficult to control than on SiC(0001) and the growth result is rotationally disordered multilayers [53]. The advantage is that rotational disorder decouples the different layers and thus carrier mobility comparable to that of exfoliated graphene has been obtained [54-56]. Therefore it is now more widely used for electronic applications; however the real impact of the rotational disorder in the whole band structure remains a subject of high controversy.

On the other hand, on SiC(0001), graphene-substrate interaction is stronger and results more uniform, wafer sized graphene films with controlled number of layers [53, 57,58]. The graphene samples are prepared in UHV by the annealing of n-doped SiC(0001) at 900K for several hours and subsequent annealing at 1500K for 30s. During the annealing at 1500K of the SiC(0001) substrate, the Si-C bonds break and the Si atoms evaporate and the remaining free carbon atoms rearrange themselves to form single layer of carbon atoms, The first formed carbon layer is called Zero layer (ZL) or buffer layer (BuL), where every third carbon atoms form a chemical bond to Si atoms in the substrate. This strong bonding is responsible for the orientation the ZL, which shows a rotation angle of 30 degree with respect to the substrate and form $(6\sqrt{3} \times 6\sqrt{3})R30^\circ$ reconstruction with respect to the substrate. The partial sp³-hybridization of the buffer

Chapter 1.Introduction

layer prevents the formation of π bands and therefore electronic properties are different from graphene [52, 54, 59-62]. Further annealing leads to the formation of monolayer graphene on top of the Buffer layer which shows the linear band structure characteristic of massless charge carriers in graphene. The epitaxial graphene is intrinsically n-doped with Dirac point at $E_D = -420\text{meV}$ due to the charge transfer from the substrate [63-66].

1.4. Defects in Graphene

Graphene is robust in nature due the strong sigma bonding among carbon atoms. As a consequence, it is very difficult for any foreign atoms to replace the carbon atoms in the honeycomb lattice. Nevertheless, graphene is not free from defects which affect the electronic properties of graphene. The defects of graphene can divided into intrinsic and extrinsic defects. The intrinsic defects include surface ripples and topological defects (pentagons, heptagons and their combinations such as Stone-Wales defect-a combination of two pentagon-heptagon pairs). The extrinsic defects are categorised into adatoms, vacancies, and extended defects such as edges and cracks [6, 67]. It is also important to produce defect free graphene or graphene with desired defects to modify the electronic properties like in conventional semiconductors.

1.5. Metal intercalations on Graphene

Graphene grown on metals by chemical vapor deposition (CVD) or epitaxially grown graphene on SiC have an influence on the underlying substrates. The underlying substrates affect the electronic properties of graphene and reduce the carrier mobility significantly. Several attempts were made to reduce/change the interaction of substrate. Most of them are largely focused on the intercalation of metals and recently hydrogen and oxygen atoms also. Another advantage of intercalation of metals on epitaxial graphene is to induce a p-type doping as it is inherently n-doped due to the charge transfer from the substrate. Such p-type doping by metal intercalation on graphite is well known and comes from graphite intercalation compounds (GICs) that are discussed in the following sections in more details.

1.5.1. Graphite intercalations

Intercalation usually occurs by inserting foreign atoms or molecules between the hexagonal two-dimensional sheets of graphite, are called Graphite intercalation compounds (GICs). GICs are well known for its famous applications i.e. lithium-ion-batteries. Introduction of metal atoms between the carbon layers can be used to tune the properties such as the interlayer spacing and charge transfer of graphite, which lead to the superconductivity. Superconductivity in GICs was studied extensively for many years until the discovery of a higher critical temperature (T_c) in fullerene (C_{60}) compounds. After several GICs were investigated with the idea of higher T_c related to the higher charge transfer to graphene from higher concentration of intercalant. However, this idea was in contrast in LiC_6 , which is not a superconductor, has large charge transfer to graphene compared to KC_8 , a superconductor with T_c of 0.14K [68]. This behaviour was encouraged to study different GICs such as C_6Yb and C_6Ca with T_c of 6.5 and 11.5K that lead to another conclusion that superconductivity in GICs was always associated with occupation of modified interlayer state lying roughly 2eV above the Fermi level and this tend to propose that its partial filling and coupling to soft intercalant phonons induces superconductivity in GICs [69]. However, the mechanism behind the superconductivity of these intercalated compounds was not well understood. It was not yet clear whether superconductivity originates in graphene plane or from the intercalants.

Recently, by using angle resolved photoemission spectroscopy study on CaC_6 , Valla *et.al.* showed that electron-phonon coupling on graphene-derived Fermi surface to graphene phonons is strong enough to explain an increase in T_c , which implies that superconductivity originates in graphene sheets whereas intercalants provide the charge for filling of the graphene π^* states. In this study, they have shown that an anomaly or a kink in dispersion of π^* band of graphene that occurs at approximately 160meV below the Fermi level is an indication of interaction of electronic states with phonons that has been attributed to a coupling to graphene in-plane high-frequency phonons. In addition, they

have made a correlation between the strength of electron phonon coupling with the filling of graphene π^* band, which is crucial for superconductivity in GICs [70]. Although it is accepted that charge transfer from intercalants triggers superconductivity, the charge balance between the π^* band and the interlayer band remains controversial.

1.5.2. Intercalations of metals on graphene on metals

The interaction with substrate is a major drawback of graphene on metals or so called graphene-metal hybrid. For example, graphene on Ir (111) is a good example of a weakly bound interface; graphene like properties are observed but the moiré pattern due to the lattice mismatch between graphene and Ir (111) give rise to Dirac cone replicas and the opening of mini gaps in the band structure [24]. This has been solved by the intercalation of potassium [71], silicon [72] and oxygen [73]. For graphene on Ni(111), due to the strong hybridization between graphene and nickel, the inherent properties of graphene are completely lost. This is solved by the intercalation of noble metals like Cu [44-45, 47, 74], Ag [45-46, 75] and Au [45, 48, 76]. These metals tend to saturate the Ni3d bonds. The chemical interaction between graphene and substrate becomes weaker that leads to ideal free standing graphene with linear dispersion and Dirac crossing energy equal to the Fermi energy (E_F). Therefore intercalation was shown to be an efficient means for tuning the graphene-substrate interaction; it also allows new properties to be imparted to graphene. For instance, graphene was strongly decoupled from the Ni substrate by the intercalation of gold, the Dirac cone of graphene was spin split, by 25meV with a Rashba effect due to the contact with high-atomic number element gold [48]. A few recent works have shown that the intercalated graphene/metals systems displaying novel magnetic properties. For instance, Cobalt films intercalated graphene on Ir(111), exhibits, an unusual strong out-of-plane magnetic anisotropy at the graphene /Co interface. Consequently, the magnetization can be maintained perpendicular to the sample surface in Co films whose thickness exceeds ten atomic layers that is thicker than the most Co films sandwiched between two metallic layers. This system is well-suited for spintronics applications [77, 78]. Rusponi *et.al.* [79] showed that the metallic clusters on

graphene/Ir(111) change the electronic properties of graphene. i.e. a reduction of the charge carrier group velocity was induced by the cluster 2D lattice.

1.5.3. Metals intercalation on Epitaxial Graphene (EG)

Epitaxially grown graphene play a significant role in the field of electronic devices due to their excellent conductivity and large scale production. However, the effect of substrate on EG reduces the charge carrier mobility [80]. Hence, numerous studies were performed on intercalations of different metals on EG in order to decouple the graphene layer from the substrate. Recently decoupling of graphene has been achieved by intercalating sodium on EG on SiC(0001). Sodium intercalates between the graphene monolayer and the interface layer also it penetrates under interfacial layer and decouples from the substrate form a second graphene layer [81]. Walter *et al.* have shown a method for decoupling EG grown SiC(0001) by intercalation of fluorine at the interface [82]. In addition, Riedl *et al.* [66] have shown that hydrogen intercalation occurs under the buffer layer, saturating the silicon dangling bonds and thus induce decoupling of the buffer layer. Historically the group from which I belong was the first to show an intercalation process with epitaxial graphene on SiC [83]. However our intercalation process is different from others where the intercalation occurs during the annealing process of carbon-rich SiC(0001) reconstruction [84]. This leads to the intercalation between the SiC substrate and the buffer layer which was associated with *p*-type doping effect. In our case the deposition of gold is done after the complete realization of the graphene monolayer leading to the intercalation between the top graphene layer and the buffer layer.

There are several other studies were performed on different intercalations such as Li [85-86], Ge[87], Bi and Sb[88]. The intercalant has significant role not only to decouple the graphene monolayer but also to modify the band structure of graphene. Such a band structure modification i.e, strong van Hove extension was observed in the case of Ca and K intercalated graphene where the graphene was strongly n-doped. Hence, the Fermi energy E_F is brought to the position of the saddle point VHS in graphene. Such a doped graphene system can achieve electronically mediated superconductivity [89]. Pan *et al.*

Chapter 1.Introduction

[90] also ascertains in their study that superconductivity originates in graphene sheets such that graphene π^* states and their coupling to graphene in-plane phonons are crucial for superconductivity and the role of intercalants is only to provide the charge for filling of the π^* states. Recently, Xue *et al.* [91] reported a successful realization of superconductivity in K doped few layer graphene with transition temperature one magnitude higher than that observed in bulk potassium graphite intercalation compound (GIC). In this study, from zero-field-cooling (ZFC) and field cooling (FC) measurements at an applied field of 50oe, when they plot the magnetic susceptibility as a function of temperature, ZFC susceptibility (χ) shows a sharp drop at $\sim 4.5\text{K}$ which is the characteristic of superconductivity. This study suggests that it should be possible to achieve superconductivity in monolayer graphene with optimal doping.

1.6. Challenges

Despite graphene has wide range of possible applications, there are still many challenges for graphene to reach its full potential. One of the main challenges is to synthesis high quality graphene in large wafer scale for electronic applications. Currently, decomposition of silicon carbide (SiC) and chemical vapor deposition (CVD) are the two methods offered for large scale growth. However, these methods are limited due to the interaction to the substrate and lack of ability to transfer epitaxial graphene onto other substrates.

In addition, the absence of band gap in monolayer graphene, which leads to low on-off ratios in graphene based field effect transistors. It has been shown that it can be achieved by quantum confinement of electrons in graphene. i.e. graphene nanoribbon formation [92].

Furthermore, the functionalization of graphene layer while preserving its inherent properties is still remains as a major challenge. Few attempts were made on the deposition of metal or molecules on top of graphene to modify the Fermi level. We have found that the intercalation of metal, opens the possibilities not only to modify the Fermi level

Chapter 1. Introduction

position but also to modify the band structure at specific points. Such methods can also open the door to functionalize graphene on both sides and to result in a Graphene-Based Hybrid structures (GBHs).

1.7. Goal and strategy of the work

One of the major drawbacks that limit the potential application of graphene is its interaction with substrate. The efficient way to minimize the interaction with substrate is intercalation. However, the role of intercalants is not only to decouple the graphene layer from the substrate but also to functionalize graphene layer while preserving its fascinating properties. Therefore the aim of this thesis was to functionalize epitaxial graphene using metals and molecules.

Our strategy was to intercalate gold on epitaxial graphene. The first goal was to induce a p-type doping effect and we have intercalated gold between buffer layer and graphene monolayer of epitaxial graphene on SiC(0001). We have evidenced different gold intercalated structures and we have found that these intercalated gold structures modify the band structure of graphene while preserving the linear dispersion of the graphene quasiparticles.

In order to put the Fermi level at the desired position, where the graphene band structure is strongly modified, we have studied the deposition of TetraThiofullvalene (TTF) molecules which are highly electron donor. We discussed the conformation of the molecule in their self-organization process and their ability to transfer a charge to the graphene layer.

Graphene is then functionalized on both sides leading to the realization of a Graphene Based Hybrid structures (GBHs).

This approach can be extended by the possibility to use photochromic molecules and to open the possibility to tune for example the doping level with the light. The molecules interaction with the graphene, how they could modify the electronic

Chapter 1.Introduction

properties, the type of grafting with graphene, the interplay with its conformation and the possible modification of the conformation in a self-assembling process consists in numerous opened questions. In the last part of the manuscript, preliminary results of photophysical studies and STM performed on photochromic molecules are presented.

Abstract: Chapter 2. Experimental techniques

Abstract: Chapter 2. Experimental techniques

Ce chapitre aborde la description des techniques de caractérisation utilisées dans ce travail, la technique de microscopie par effet tunnel (STM) et la spectroscopie (STS). La spectroscopie de photoélectron résolue en angle (ARPES). Puis les techniques de spectroscopie optiques, absorption UV-visible, fluorescence et absorption à deux photons utilisées pour caractériser les molécules photochromes.

Chapter 2. Experimental Techniques

2. Experimental Techniques

This chapter describes the experimental techniques that have been used in this thesis work. The first part is devoted to the technique of scanning tunneling microscopy (STM) and photoelectron spectroscopy (PES) which includes Angle resolved photoemission spectroscopy (ARPES) and X-ray photoelectron spectroscopy (XPS). The second part is devoted to the optical measurements.

2.1 Scanning Tunneling Microscopy (STM)

The scanning Tunneling Microscope was invented by Binnig and Rohrer in 1982, for which they shared the 1986 Nobel Prize in Physics [93]. The STM works by bringing a sharp metal tip in close proximity (\AA order) to a conducting surface. When a bias voltage is applied between the tip and sample, the electrons quantum mechanically tunnel across the gap and produce a so called tunneling current. This current has an exponential dependence on the tip and sample separation, which means that for a small change in the distance between the tip and the sample the current changes drastically.

Since its invention, STM has made a dramatic impact in diverse fields such as materials science, semiconductor physics, biology, electrochemistry, surface thermodynamics, organic chemistry etc. The reason is that STM provides three – dimensional, real space images of surfaces at high spatial resolution. Even single atoms can be imaged when a sample is clean and flat [94].

Chapter 2. Experimental Techniques

2.1.1 Basic Theory of STM

2.1.1.1 The concept of tunneling – a simple 1D model

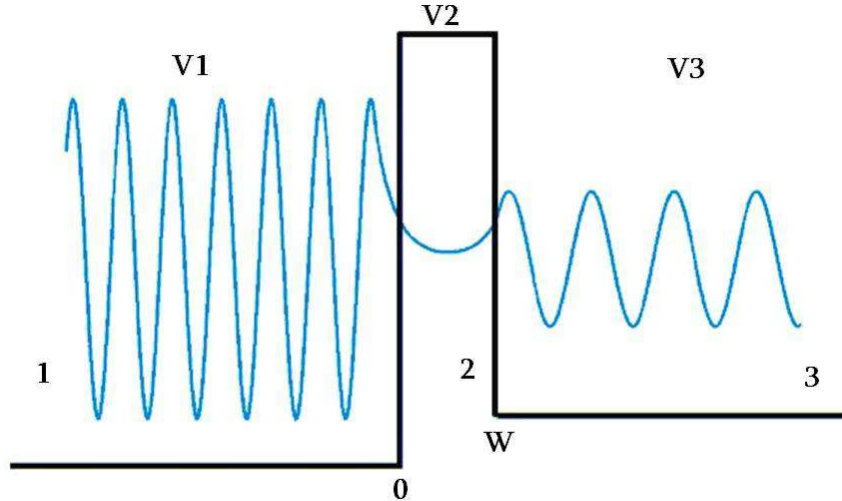


Figure.2.1: A 1D rectangular potential barrier of width w . A sketch of wave function for $E < V_2$ is shown.

In the simple 1D model the electron with mass m is considered to be incident on a rectangular potential barrier (Figure 2.1). The aim is to calculate the probability for the electron to penetrate the barrier from the left side (region 1) to the right (region 3) by solving the Schrödinger equation

$$\left(-\frac{\hbar^2}{2m} \frac{\partial^2}{\partial x^2} + V(x) \right) \Psi(x) = E\Psi(x) \quad (\text{Eq.2.1})$$

The wave function solution can be written down as

$$\Psi_n(x) = a_n e^{ik_n x} + b_n e^{-ik_n x} \quad (\text{Eq.2.2})$$

where

$$k_n = \sqrt{\frac{2m(E - V_n)}{\hbar^2}} \quad (\text{Eq.2.3})$$

Chapter 2. Experimental Techniques

Here the index $n = 1, 2, 3$ corresponds to the pre-barrier, barrier, post-barrier region respectively. If the energy of the electron, E is lower than the barrier potential V_2 , the wave function K_2 is imaginary; $k_2 = ik$ with $k = \sqrt{\frac{2m(V_2 - E)}{\hbar^2}}$, and the corresponding wavefunction decays exponentially instead of oscillating. The coefficients a_n and b_n are determined from the boundary conditions and the requirements that the wave function and the derivatives should be continuous.

The current density (flux) is defined as

$$j = \frac{\hbar}{2im} \left(\Psi^* \frac{\partial \Psi}{\partial x} - \frac{\partial \Psi^*}{\partial x} \Psi \right) \quad (\text{Eq.2.4})$$

The transmission through the barrier is defined as the ratio between outgoing flux in region 3 and the in-going flux in region 1;

$$T = \frac{j_3}{j_1} = \frac{k_3 |a_3|^2}{k_1 |a_1|^2} \quad (\text{Eq.2.5})$$

The ratio of $\frac{|a_3|^2}{|a_1|^2}$ must be calculated and this allows the transmission to be determined by matching the boundary conditions, leading to

$$T = \frac{(2k)^2 k_1 k_3}{k^2 (k_1 + k_3)^2 + (k^2 + k_1^2)(k^2 + k_3^2) \sinh^2 kw} \quad (\text{Eq.2.6})$$

where w is the width of the barrier. Since the transmission is non zero, even though the energy of the electron is smaller than energy of the barrier ($E < V_2$), contrary to classical physics, the incoming electron may tunnel through the potential barrier. In the STM tunnel junction, the barrier height is in the order of the work function and the barrier width corresponds to the tip-sample distance. For a barrier of for instance 4eV height and 5 Å width, one finds the sinh-term in the denominator leading to

$$T \propto e^{-2k\omega} \quad (\text{Eq.2.7})$$

Chapter 2. Experimental Techniques

Thus, the transmission is very sensitive to the barrier width and height. The exponential dependence on the barrier width of the leading term of T is common to all tunneling problems.

2.1.1.2 The perturbative approach of tunneling current

The above rectangular barrier model can be considered as zeroth-order approximation to the real vacuum gap barrier between the tip and the sample. However, the 1D model is in general cannot be solved for a potential barrier of arbitrary shape. Therefore, the problem can be tackled by using perturbative approach.

The Fermi's golden rule, from the first-order time-dependent perturbation theory, states that the transmission rate from the initial state $|i\rangle$ to a final state $|f\rangle$ is given by

$$R_{i \rightarrow f} = \frac{2\pi}{\hbar} |M_{fi}|^2 \delta(E_i - E_f) \quad (\text{Eq.2.8})$$

where M_{fi} is the matrix element of the perturbation potential between the initial and final states, the δ -function ensures the energy conservation. [95]. It is possible to determine the current flowing from sample to tip or vice versa by applying the bias voltage to the sample V_s . When a positive bias voltage is applied to the sample, the electrons will flow from tip to the sample.

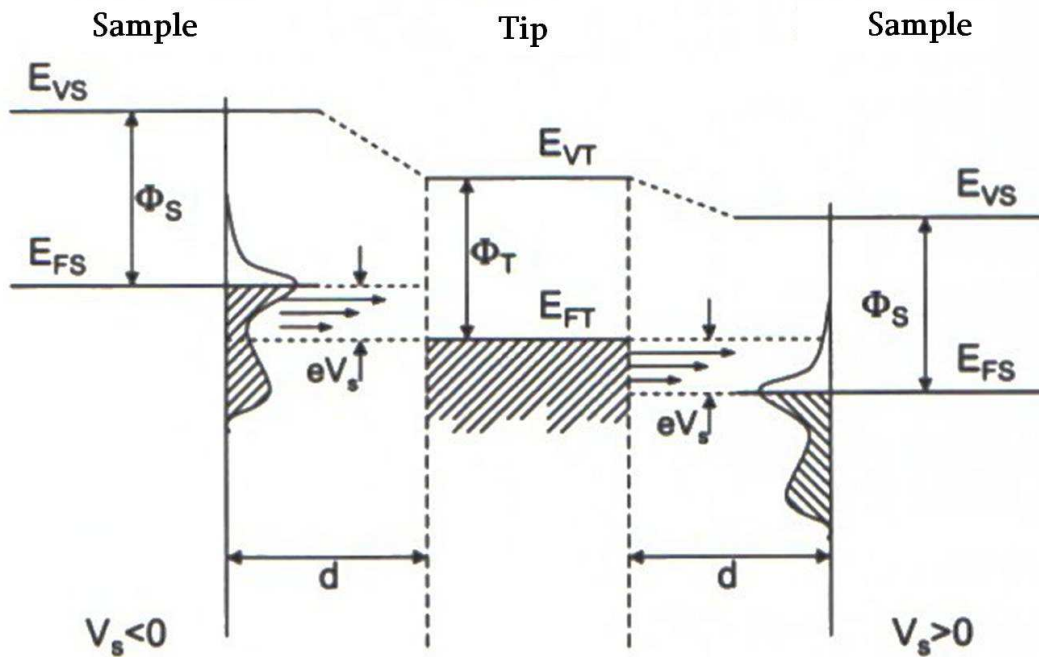


Figure.2.2: Energy diagram for the tunnel junction between two metallic electrodes. The arrows indicate the energy-dependent tunneling probability; ϕ_s and ϕ_T are the work functions for sample and tip respectively [95].

According to Fermi's golden rule, the current flowing from tip to the sample can be written as

$$I_{t \rightarrow s} = \frac{2\pi e}{\hbar} \int |M_{st}|^2 \rho_t(E + eV_s) f_t(E + eV_s) \rho_s(E) [1 - f_s(E)] dE \quad (\text{Eq.2.9})$$

Here $f(E) = \frac{1}{(e^{(E-E_F)/K_B T} + 1)}$ is the Fermi-Dirac distribution and ρ_t and ρ_s are the density of states of tip and sample respectively. The electrons from occupied tip states ($\rho_t f_t$) can tunnel into unoccupied sample states ($\rho_s [1 - f_s]$) and common energy scale is taken to be that of sample and thus the tip energy scale is shifted by eV_s .

Similarly, the current flowing from sample to tip is given by

$$I_{s \rightarrow t} = \frac{2\pi e}{\hbar} \int |M_{ts}|^2 \rho_t(E + eV_s) [1 - f_t(E + eV_s)] \rho_s(E) f_s(E) dE \quad (\text{Eq.2.10})$$

Chapter 2. Experimental Techniques

Therefore, the total current flowing from tip to sample is

$$I = I_{t \rightarrow s} - I_{s \rightarrow t} \quad (\text{Eq.2.11})$$

$$I = \frac{2\pi e}{\hbar} \int |M_{st}|^2 \rho_t(E + eV_s) \rho_s(E) [f_s(E) - f_t(E + eV_s)] \quad (\text{Eq.2.12})$$

At zero temperature, the Fermi-Dirac distribution is a step function and then (Eq.2.12) becomes,

$$I = \frac{2\pi e}{\hbar} \int_{E_F}^{E_F - eV_s} |M_{st}|^2 \rho_t(E + eV_s) \rho_s(E) dE \quad (\text{Eq.2.13})$$

Now we have to evaluate the matrix elements M_{st} . Bardeen showed that, under certain assumptions, these can be expressed as

$$M_{st} = \frac{\hbar^2}{2m} \int_S (\Psi_s^* \nabla \Psi_t - \Psi_t \nabla \Psi_s^*) ds \quad (\text{Eq.2.14})$$

where S is the surface separating tip and sample regions. To evaluate the effective matrix element, one must know the tip and sample wave functions. But the exact atomic electronic structure is unknown, one has to assume a model tip wave function and this approach was used by Tersoff and Hamann [96].

2.1.1.3 Tersoff and Hamann's model

Tersoff and Hamann developed their theory in 1983 and it is still widely used in the interpretation of the STM images [96]. In this model, the unknown electronic structure of the tip is replaced by a simple spherical model.

In the limit of low (or zero) temperature and low bias voltage the total current flowing from tip to sample can be written as (compared to (Eq.2.13));

$$I = \frac{2\pi e^2}{\hbar} V \sum_s |M_{ts}|^2 \rho_t(E_F) \delta(E_s - E_F) \quad (\text{Eq.2.15})$$

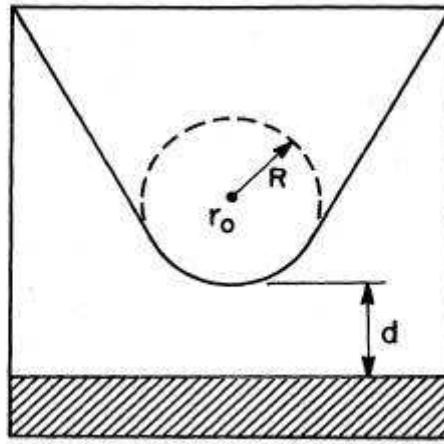


Figure.2.3: Tip geometry used in Tersoff and Hamann's model. Tip has arbitrary shape, assumed locally spherical with radius of curvature R , and centre of curvature r_0 [96].

To evaluate the matrix element, the surface wave function is written as a 2D Bloch expansion:

$$\psi_s = e^{i\mathbf{k}_{\parallel} \cdot \mathbf{r}_{\parallel}} \sum_{\mathbf{G}} a_{\mathbf{G}}(z) e^{i\mathbf{G}_{\parallel} \cdot \mathbf{r}_{\parallel}} \quad (\text{Eq.2.16})$$

where \mathbf{G} is the 2D reciprocal lattice vector. After inserting the wave function (Eq.2.14) in to the Schrödinger equation and assuming that the potential V is independent of \mathbf{r} , it was found that the wave function can be rewritten as

$$\psi_s = \sum_{\mathbf{G}} a_{\mathbf{G}}(0) e^{-\sqrt{k^2 + (\mathbf{k}_{\parallel} + \mathbf{G})^2} z} e^{i(\mathbf{k}_{\parallel} + \mathbf{G}) \cdot \mathbf{r}_{\parallel}} \quad (\text{Eq.2.17})$$

Here $k^2 = \frac{2m}{\hbar^2(V_s - E)}$. The wave function of the tip can be modeled as a spherical potential (Figure.2.3) with radius of curvature R about the centre r_0 . So the tip wave function is chosen to have the form of s-wave.

$$\Psi_t(\mathbf{r}) = kR e^{kR} \frac{e^{-k|r-r_0|}}{k|r-r_0|} \quad (\text{Eq.2.18})$$

If the separation surface S be a plane parallel with the surface, then the matrix element is proportional to the sample wave function evaluated at the tip centre of curvature;

Chapter 2. Experimental Techniques

$$M_{ts} \propto \Psi_s(\mathbf{r}_0) \quad (\text{Eq.2.19})$$

Then the total current flowing from tip to the sample is given by (Eq.2.15 becomes)

$$I \propto V \rho_t(E_F) \sum_s |\Psi_s(\mathbf{r}_0)|^2 \delta(E_s - E_F) \quad (\text{Eq.2.20})$$

In this expression the sum is the local density of states of the sample (LDOS) at the Fermi level, evaluated at the tip center. Then the final result of Tersoff and Hamann is

$$I \propto V_s \rho_t(E_F) \text{LDOS}(\mathbf{r}_0, E_F) \quad (\text{Eq.2.21})$$

This equation gives an easy tool for interpretation of the STM images. The basic quantity which is imaged is the local density of states (LDOS) of the sample. Scanning tunneling spectroscopy (STS) provides information about the density of states of the sample as a function of their energy and allows for local tunneling spectra to be obtained.

2.1.2 Principles of operation

Figure 2.4 shows the schematic description of a scanning tunneling microscope. The STM tip is usually made of W or Pt-Ir alloy. The tip is attached to a piezodrive, which consists of three mutually perpendicular piezoelectric transducers: x piezo, y piezo and z piezo. A piezoelectric transducer expands or contracts by applying a voltage. Up on applying a sawtooth voltage on the x piezo and a voltage ramp on the y piezo, the tip scans on the xy plane. Using the coarse positioner and the z piezo, the tip and the sample can be brought in the close proximity and thus the electron wave function in the tip can overlap with that of sample surface. A finite tunneling conductance is generated. By applying a bias voltage between the tip and the sample, a tunneling current is generated and measured.

In our system, tip is grounded and the bias voltage V is the sample voltage. If $V > 0$, the electrons are tunneling from the occupied states of tip into the empty states of the sample. If $V < 0$, the electrons are tunneling from the occupied states of sample into the empty states of the tip. The tunneling current is amplified and then converted to a voltage

Chapter 2. Experimental Techniques

by the current amplifier which is then compared with a reference value. The difference is amplified to drive the z piezo. The phase of the amplifier is designed to provide a negative feedback. If the absolute value of the tunneling current is larger (smaller) than the reference value, the tip is retracted (approached) from the sample surface and thus equilibrium z position is established through the feedback loop. A two-dimensional array of equilibrium z positions, representing a contour plot of the equal tunneling-current surface is obtained when the tip scans over the xy plane.

To obtain atomic resolution, vibration isolation is essentially required. This can be achieved by making the very rigid STM unit and by reducing the influence of environmental vibration to the STM unit. The later can be achieved by employing a suspension springs and damping mechanisms [97].

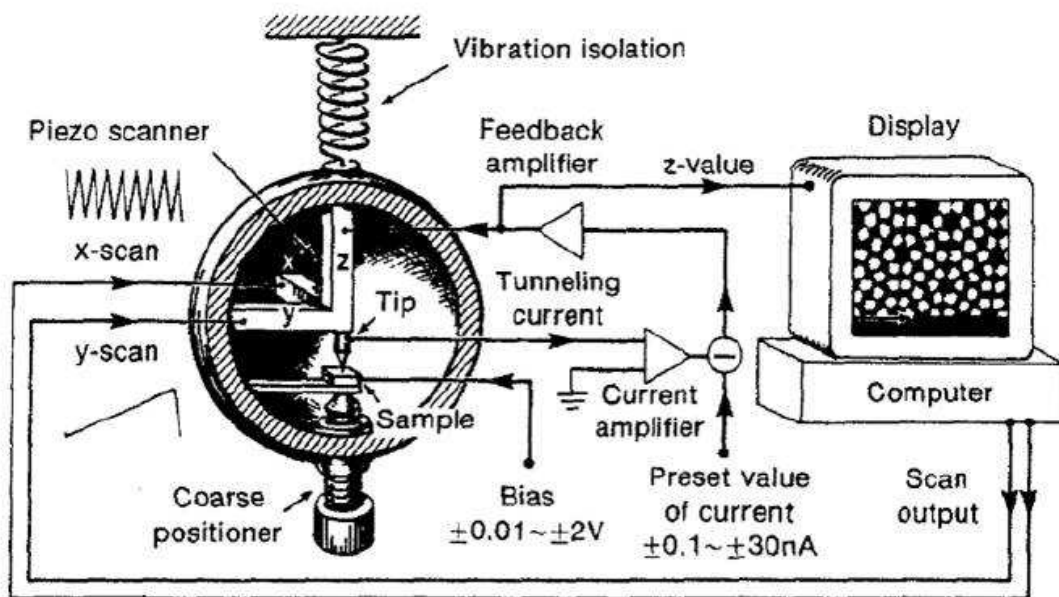


Figure.2.4: Schematic representation of STM [97].

Chapter 2. Experimental Techniques

2.1.3. Measurement types

The STM can be operated in two modes either in constant height mode or in constant current mode. In constant height mode, the tip can be scanned across a surface at nearly constant height and constant voltage while the current is monitored. In this mode, the adjustment of tip-sample separation is not required; therefore a high scan speed can be obtained. However, the constant height mode is only applicable for very flat surface and if the surface corrugation is typically larger than $5\text{-}10\text{\AA}$, cause the tip to crash. Alternatively, in constant current mode, a feedback loop is enabled that maintains a constant current while a constant bias is applied between the sample and the tip. The motion of the scanner requires more time but the high resolution image of irregular surface can be obtained.

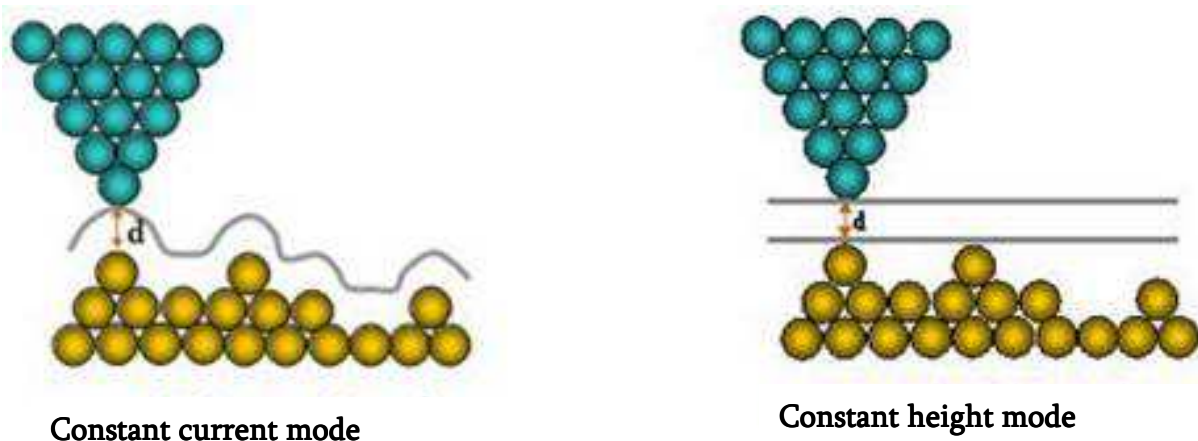


Figure.2.5: Constant current mode and height mode

In addition to reveal the geometrical structure of the sample, a more important application of STM is to resolve the local electronic structure of the sample (LDOS) as a function of energy. Scanning tunneling spectroscopy (STS) is a valuable technique to investigate the electronic properties of the sample surface. By varying the bias voltage at constant tip-sample separation, I/V spectra can be recorded. Furthermore, the tunneling conductance dI/dV can be obtained by numerical differentiation of I/V or using a lock-in technique which will be described below.

Chapter 2. Experimental Techniques

Current Imaging Tunneling Spectroscopy (CITS) is an STS technique where an I/V curve is recorded at each pixel of the scan area. As a practical concern, the number of pixels in the scan or the scan area may be reduced to prevent piezo creep or thermal drift from moving the feature of study or the scan area during the duration of the scan. Since some CITS scans can last in excess of 12 hours, low drift and creep are absolutely necessary[98].

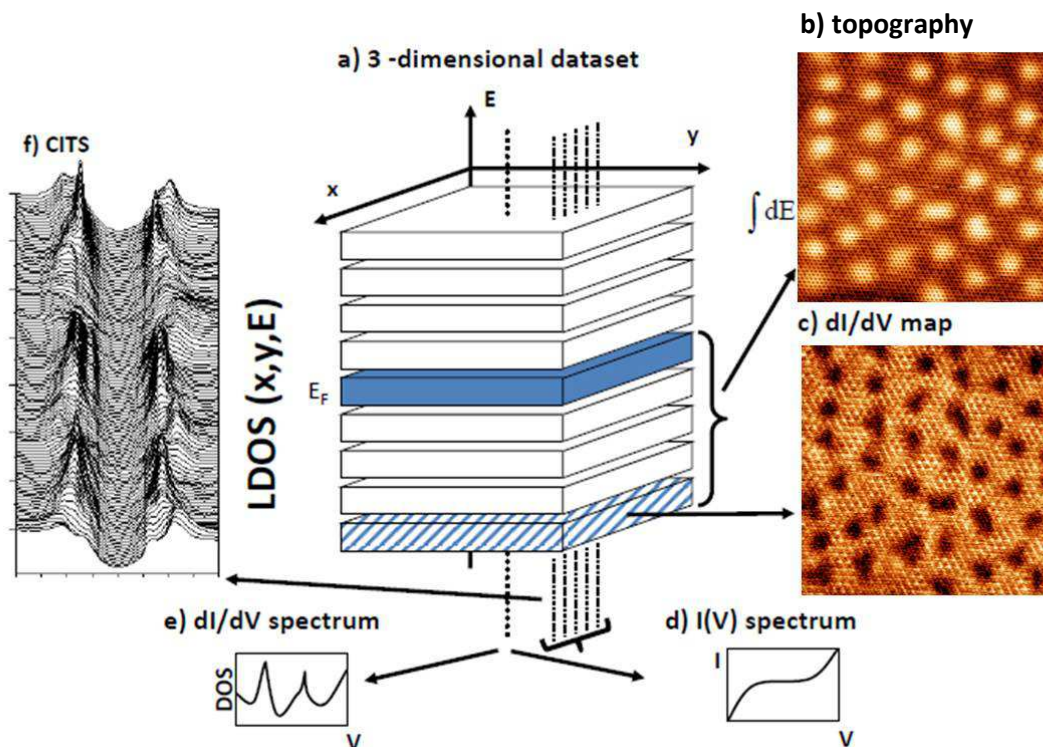


Figure.2.6: An STM has an access to an essentially 3-dimensional dataset: two spatial dimensions (x,y) and energy E . This 3-dimensional data space can be explored in different ways (b)-(f). (b) Topography: the tip is scanned across the surface at a fixed sample bias voltage V_s , while a feedback loop control the voltage on the piezo to keep the constant tunneling current I_t . (c) dI/dV map: the density of states at a fixed energy E is mapped as a function of position (x,y) on the sample surface. (d) $I(V)$ spectrum: current as a function of bias voltage is measured at a single point on the sample surface. (e) dI/dV spectrum: the density of states as a function of energy is measured at a single point on the sample surface. (f) CITS spectrum: the density of states as a function of energy is mapped at several points along a line on the sample surface. (b) and (c) indicate the topography and dI/dV map of gold intercalated clusters (DP) is shown in chapter 2. The size of the images is ($14\text{nm} \times 14\text{nm}$).

Chapter 2. Experimental Techniques

2.1.4. Measurement of dI/dV using lock-in amplifier

This section briefly describes the measurement of dI/dV using a lock-in amplifier. A lock-in amplifier only amplifies the amplitude of a signal with a given frequency, determined by a reference signal. This can be utilized to measure the dI/dV of the tunnel junction. The idea is to modulate the bias voltage around a value V_s , let $V = V_s + \Delta V(\omega)$. The frequency ω is chosen to be much larger than the bandwidth of the STM feedback loop. In that way, the z-piezo will not respond to the bias variations but the tunneling current will. Using a first order-Taylor expansion, the tunneling current is given by

$$I(V_s + \Delta V(\omega)) \cong I(V_s) + \frac{dI}{dV}(V_s)\Delta V(\omega) \quad (\text{Eq.2.22})$$

The lock-in amplifier is integrated in the STM as shown in Figure 2.7. In the case of LT-STM Omicron, it is necessary to be compensated the capacitive signals during modulation due to the length of electric cables inside the STM between the tip and pre-amplifier as indicated in Figure 2.7.

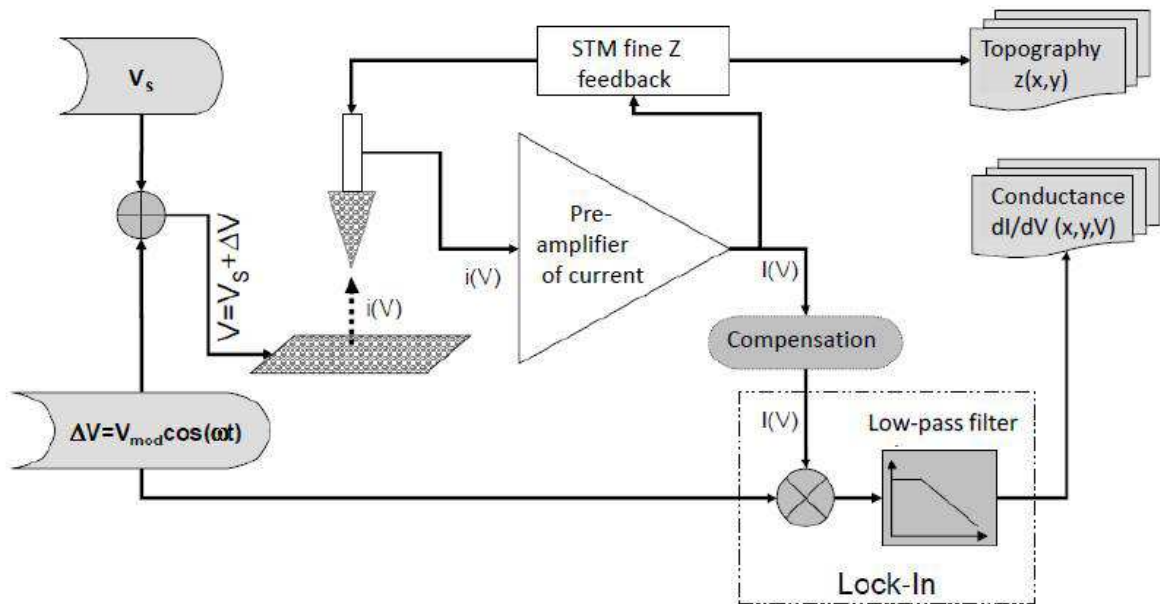


Figure.2.7: Schematic representation of measurement of dI/dV using lock-in technique.

The schematic diagram in Figure 2.8 describes the role of lock-in amplifier in detail. The tunneling current $I(V_s + \Delta V)$ is amplified and passed through a band-pass

Chapter 2. Experimental Techniques

filter while the modulation signal $\Delta V = V_{mod} \cos(\omega t)$ undergoes a phase shift θ . From Eq.2.22 the convolution of two signals provides the signal S is give by

$$S = \left[I(V_S) + \frac{dI}{dV} V_{mod} \cos(\omega t) \right] \times [V_{mod} \cos(\omega t + \theta)]$$

$$= I(V_S) V_{mod} \cos(\omega t + \theta) + \frac{1}{2} \frac{dI}{dV} V_{mod}^2 [\cos \theta + \cos(2\omega t + \theta)] \quad (\text{Eq.2.23})$$

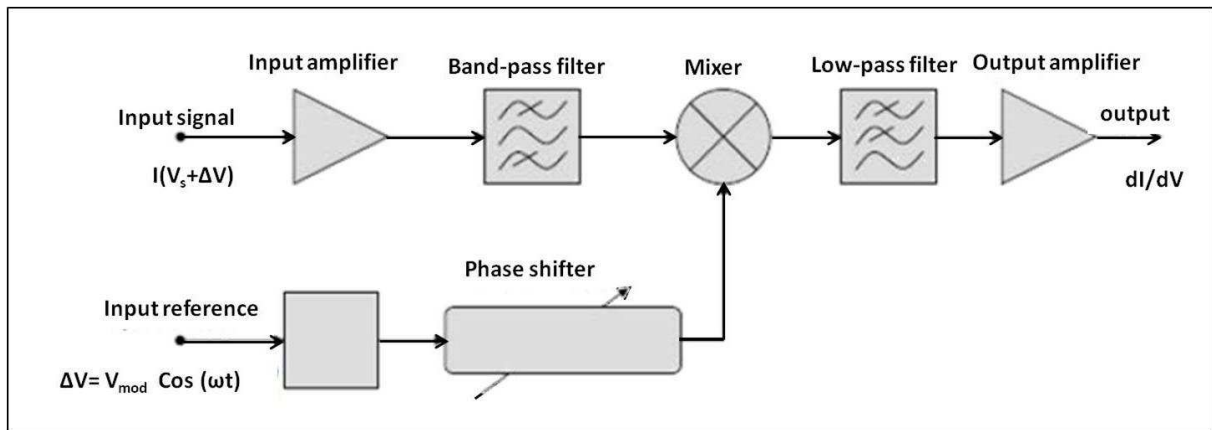


Figure.2.8: Schematic diagram of signal processing by lock-in amplifier for the determination of dI/dV .

Finally, the signal passes through a low-pass filter, where the frequencies ω and 2ω are filtered out and only the term $\frac{1}{2} \frac{dI}{dV} V_{mod}^2 \cos \theta$ in Eq.2.23 remains which is a DC signal, and the resulting signal is proportional to LDOS, i.e. $S \propto \frac{dI}{dV}$.

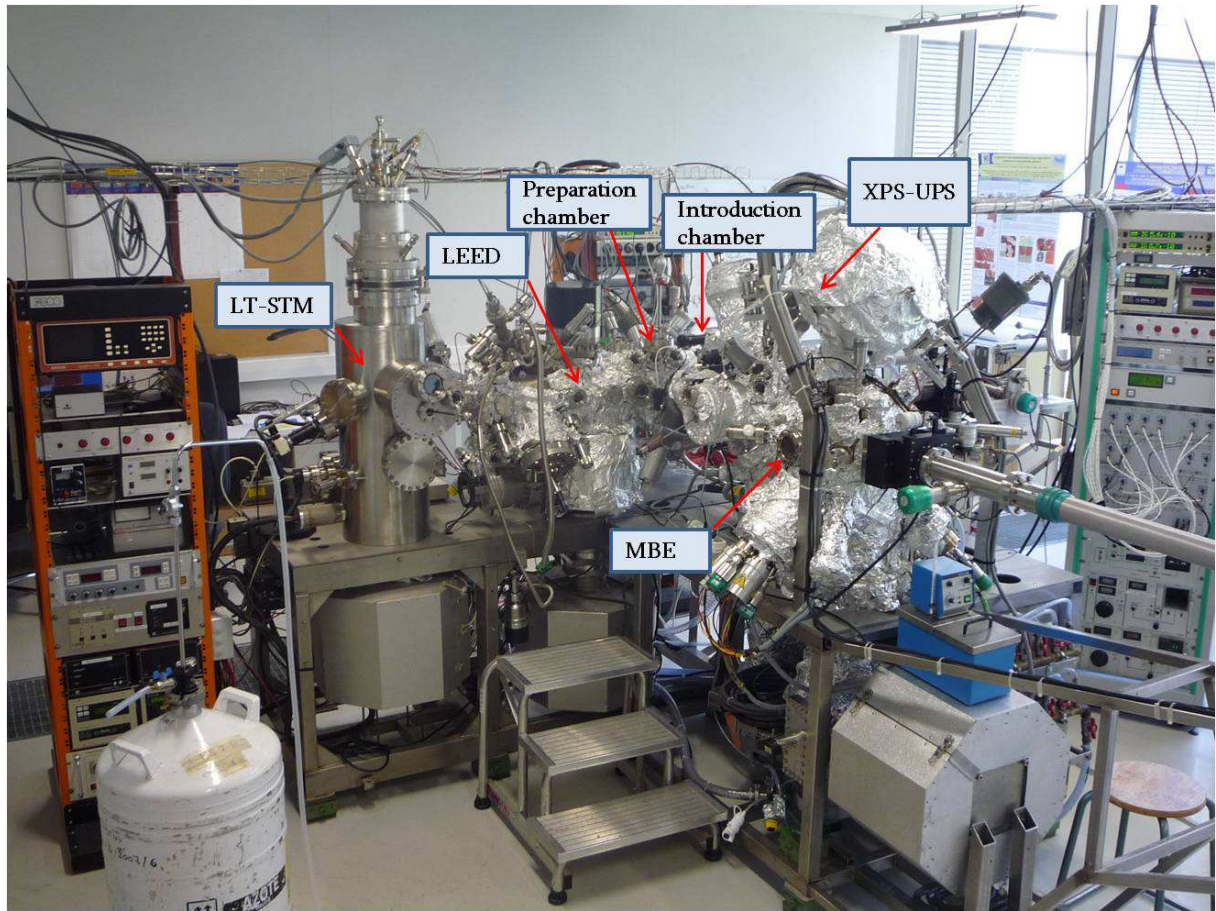


Figure.2.5: STM experimental set up in our laboratory.

2.2. Photoelectron Spectroscopy (PES)

The other main experimental technique used in this thesis was photoelectron spectroscopy (PES). Two types of PES, namely Angle resolved photoelectron spectroscopy (ARPES) and X-ray photoelectron spectroscopy (XPS) were used to study the valence band and core level electrons of pristine graphene and gold intercalated graphene respectively. The PES measurements in this thesis were carried out at the SOLEIL synchrotron radiation. The synchrotron radiation provide the radiation energy range from 5-5000eV, make such experiments surface sensitive extending from a few atomic layers down to the sub monolayer regime.

Chapter 2. Experimental Techniques

2.2.1. Principle of photoelectron spectroscopy (PES)

The photoelectron spectroscopy is based on the photoelectric effect. When a photon with energy $h\nu$ incidents on the sample, the electrons with kinetic energy E_{kin} are released from the surface if the photon energy is greater than the work function of the sample ϕ . (ϕ is a measure of potential barrier at the surface that prevents the valence electrons from escaping, typically 4-5eV in metals).

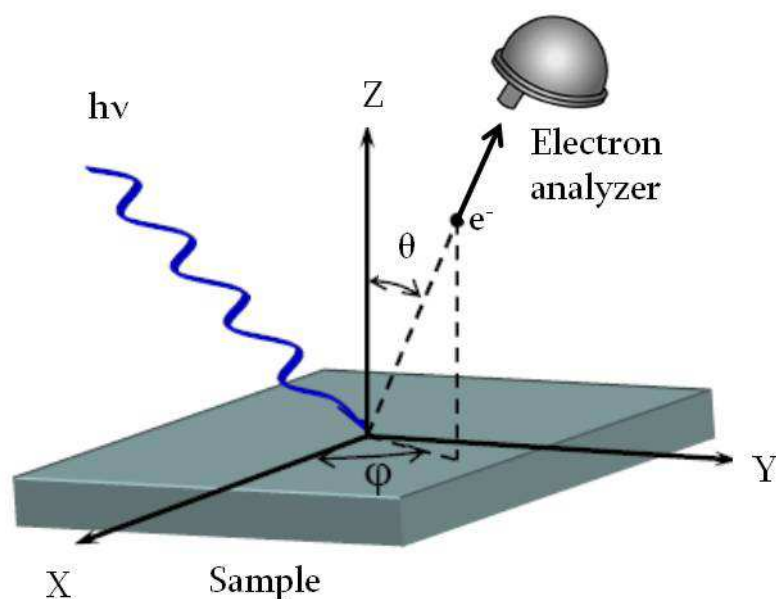


Figure. 2.6: Schematic of photoemission process.

The light source is a gas discharge, an X-ray tube or a synchrotron radiation source. Basically one can distinguish between Ultraviolet photoelectron spectroscopy (UPS), mainly for the (angle resolved) investigation of valence band states and XPS, for the investigation core-level states, based on the two different types of excitation sources. Photons in the vacuum ultra violet (VUV) range are used for the excitation of valence electrons (UPS), where as soft X-rays can excite core level electrons (XPS). When a light impinges on the sample, the electrons excited by the photoelectric effect are then analyzed with respect to their kinetic energy E_{kin} and their momentum \mathbf{P} in an electron analyzer. Note that the energy and momentum must be conserved during the

Chapter 2. Experimental Techniques

photoemission process. The polarization of the light is a useful property in an angle-resolved photoemission experiment. The direction of the photoelectron is given by the polar and azimuthal angle θ and ϕ respectively.

The kinetic energy and momentum of the outgoing electrons are detected by a detector is given by

$$E_{kin} = h\nu - |E_B| - \phi \quad (\text{Eq. 2.24})$$

$$P = \sqrt{2mE_{kin}} \quad (\text{Eq.2.25})$$

where E_B is the binding energy and ϕ is the work function of the analyzer. Since E_B is referenced to the Fermi level E_F , Eq.2.24 is independent of sample's work function. E_F is same for sample and the analyzer provided they are in electrical contact with each other.

The fundamental principle of the photoemission process is sketched in Figure.2.7. This simplified energy diagram shows the attractiveness of PES because the properties of the photoelectrons basically reflect the electronic eigenstates of the investigated system. The electrons in their initial state can be originated from the core levels or valence band. Electrons with binding energy E_B can be excited above the vacuum level E_{vac} by photons with energy $h\nu > E_B + \phi_0$. The photoelectron distribution $I(E_{kin})$ can be measured by the analyzer which is a representation of occupied density of electronic states $N(E)$ in the sample[99].

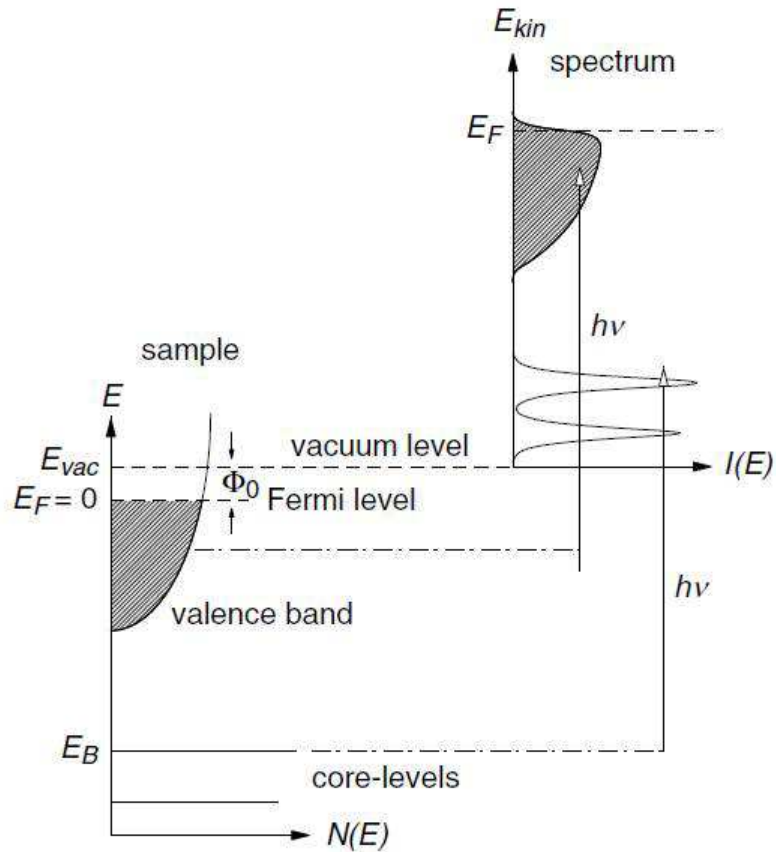


Figure.2.7: Energy diagram of the Photoemission process [100].

The main advantage of PES is its surface sensitivity. This originates from the inelastic mean free path (IMFP) λ of electrons in solids. This is defined as the mean distance electrons can travel without energy loss due to inelastic scattering. Figure 2.8 shows the “universal” electron mean free path λ in Å as a function of electron kinetic energy for a few selected metals. From the Figure 2.8, it is clear that in the kinetic energy range of interest, between about 10 and 2000 eV, the IMFP is only of the order of a few Å. This means that any spectroscopy of a solid surface involving electrons samples only electrons from a very thin layer of the sample.

Therefore, if one wishes to learn about the bulk properties of the solid, one has to work with atomically clean surfaces. Also, the investigation of surface states or adsorbed molecules requires UHV conditions to prevent interference from adsorbed contaminants.

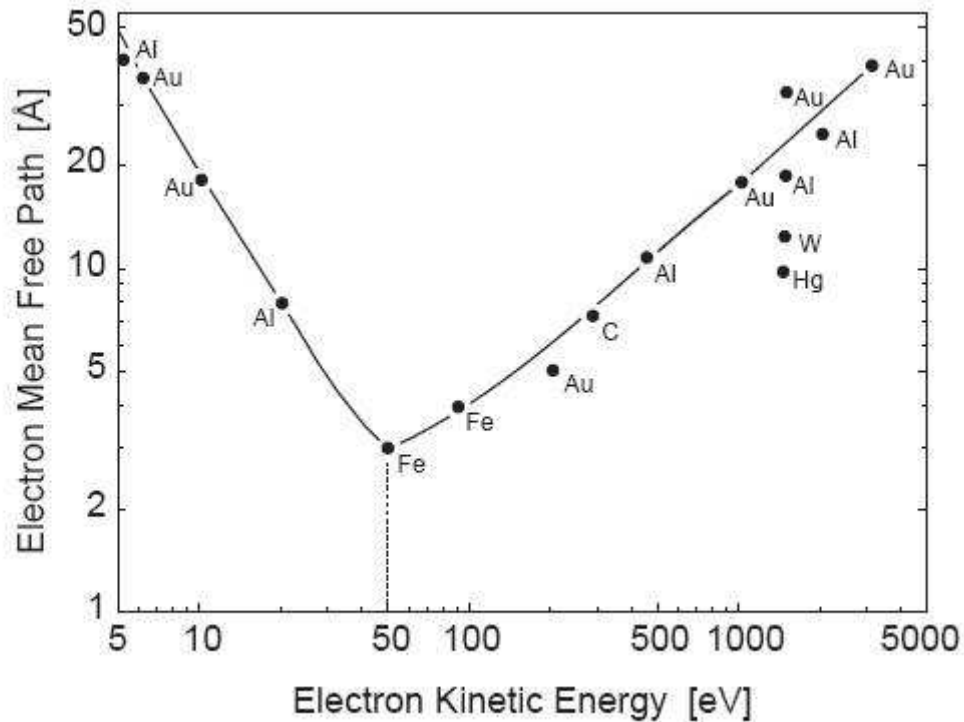


Figure.2.8: Electron mean free path λ of electrons in solids as a function of their kinetic energy for various metals. The diagram is adapted from [100].

2.2.2. Angle resolved Photoemission spectroscopy (ARPES)

ARPES is one of the most direct methods for probing the electronic structure of solids. ARPES is usually associated with valence band electrons. ARPES spectra give the information about the angular and energy distribution of photoelectrons. From the energy and momentum distribution of electrons, one can determine the electronic dispersion curves $E(K)$ in the solid. The basic principles of ARPES are briefly discussed below.

The most commonly used model for the interpretation of photoemission spectra in solids is the so called three-step model developed by Berglund and Spicer [101]. In this model, the photoemission process is divided in to three independent steps; the first step is photo excitation of an electron, the second step is propagation of an excited electron to the surface and the last step is escape of photoelectron into vacuum. However, from the quantum mechanical point of view of photoemission should not be described in terms of three independent steps but rather as a one-step process. The one-step model describes

Chapter 2. Experimental Techniques

photo excitation from an initial state (Bloch wave in the crystal) into a damped final state near the surface. This damping takes care of the short mean free path of electrons in a solid. In contrast to three-step model, where the three processes are considered as independent from each other, the one-step model takes into account interference between the three steps. A correct one-step treatment is based on Fermi's Golden Rule with proper functions for initial and final state and the dipole operator for the interaction between electron and photon. However, one-step model was not solved efficiently therefore various approximations have to be used to make it feasible and one of these approximation is so-called sudden approximation.

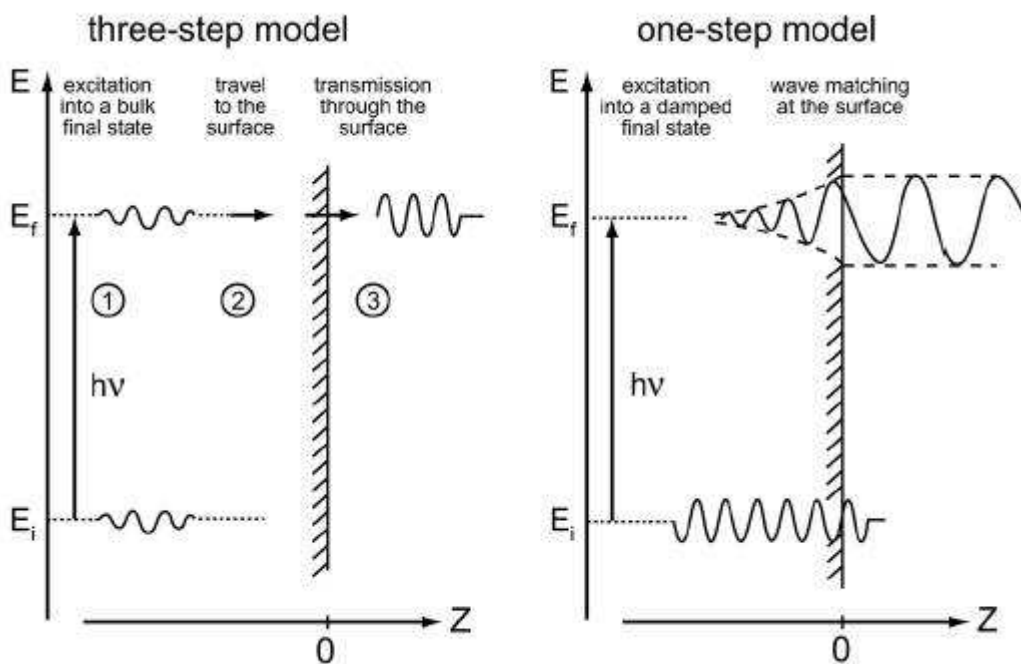


Figure.2.9 Three-step and one-step model descriptions of the photoemission process. Adapted from [102].

Chapter 2. Experimental Techniques

2.2.2.1. The sudden approximation

The photocurrent produced in the photoemission experiments results from the excitation of electrons from the initial states i with wavefunction ψ_i to the final states f with wavefunction ψ_f by the photon field having the vector potential \mathbf{A} . The photocurrent is proportional to the transition probability w and can be calculated with Fermi's Golden Rule using the dipole approximation [99]

$$I \propto \frac{2\pi}{\hbar} |\langle \psi_f | \mathbf{A} \cdot \mathbf{P} | \psi_i \rangle|^2 \delta(E_f - E_i - h\nu) \quad (\text{Eq.2.26})$$

In the simplest approximation, the initial (final) wave function can be written as the product of the orbital $\phi_{i,\mathbf{k}}$ from which the electron is excited (the wave function of the photoemitted electron, $\phi_{f,E\mathbf{k}_{in}}$) times the wave function of remaining electrons (N-1) electrons. For solids, the photocurrent I is usually written in terms of spectral function $A(\mathbf{k},E)$.

$$I \propto \sum_{f,i,\mathbf{k}} |\langle \phi_{f,E\mathbf{k}_{in}} | \mathbf{r} | \phi_{i,\mathbf{k}} \rangle|^2 A(\mathbf{k},E) \quad (\text{Eq.2.27})$$

where $A(\mathbf{k},E)$ is the so called spectral function for wave number \mathbf{k} energy E and the photo emission spectroscopy essentially measures the spectral function. The spectral function can be related to the single particle Green's function by

$$A(\mathbf{k},E) = \frac{1}{\pi} \text{Im}\{G(\mathbf{k},E)\} \quad (\text{Eq.2.28})$$

For a noninteracting system with one-electron energy $E_{\mathbf{k}}^0$,

$$G_0(\mathbf{k},E) = \frac{1}{E - E_{\mathbf{k}}^0 - i\epsilon} \quad (\text{Eq.2.29})$$

Where ϵ is a small number and $A_0(\mathbf{k},E) = \delta(E - E_{\mathbf{k}}^0)$ meaning that the spectral function is a δ function $E = E_{\mathbf{k}}^0$.

In an interacting electron system, the electron energy gets renormalized by the so called self energy

Chapter 2. Experimental Techniques

$$\Sigma(\mathbf{k}, E) = \text{Re}\{\Sigma(\mathbf{k}, E)\} + i\text{Im}\{\Sigma(\mathbf{k}, E)\} \quad (\text{Eq.2.30})$$

Yielding $G(\mathbf{k}, E) = \frac{1}{E - E_k^0 - \Sigma(\mathbf{k}, E)}$ and the corresponding spectral function is given by

$$A(\mathbf{k}, E) = \frac{1}{\pi} \frac{\text{Im}\{\Sigma(\mathbf{k}, E)\}}{[E - E_k^0 - \text{Re}\{\Sigma(\mathbf{k}, E)\}]^2 + [\text{Im}\{\Sigma(\mathbf{k}, E)\}]^2} \quad (\text{Eq.2.31})$$

The real part $\text{Re}\{\Sigma(\mathbf{k}, E)\}$ causes deviations from bare band dispersion E_k^0 while $\text{Im}\{\Sigma(\mathbf{k}, E)\}$ is responsible for intrinsic line width in photoemission spectrum and gives the lifetime broadening of a quasi particle. In fact, the spectral function is a fundamental quantity that determines all the properties of a many-body system. The various many body renormalizations of the bare dispersion can arise from either electron- phonon or electron-electron interactions.

To understand the momentum conservation, we can go back to the last step in the three-step model where electron is transmitted through the surface into the vacuum. In this transition (Figure 2.10), the electron wave vector component parallel to the surface (\mathbf{K}_{\parallel}) is conserved up to the reciprocal lattice vectors of the surface lattice \mathbf{G}_s and reciprocal lattice vector of the crystal lattice parallel to the surface \mathbf{G}_{\parallel} provided the emission is from a well ordered, crystalline surface. Therefore, $\mathbf{K}_{\parallel}^{ext} = \mathbf{K}_{\parallel}^{int} + \mathbf{G}_s + \mathbf{G}_{\parallel}$. Hence in the reduced zone scheme we can write,

$$\mathbf{K}_{\parallel}^{int} = \mathbf{K}_{\parallel}^{ext} = \mathbf{K}_{\parallel} = \sqrt{\frac{2m}{\hbar^2} E_{kin}} \sin(\theta) \quad (\text{Eq.2.32})$$

where \mathbf{K}^{int} and \mathbf{K}^{ext} are the electron wave vectors inside and outside the solid respectively. $E_{kin} = \frac{\hbar^2 K^2}{2m}$ is the kinetic energy of the photoelectron in vacuum emitted at the polar angle θ with respect to the normal. Therefore with the help of Eq. 2.24 and Eq. 2.32 the band structure is directly obtained. For a two-dimensional material such as graphene, K_{\perp} does not exist so that $E(K_{\parallel})$ represents the initial state band dispersion.

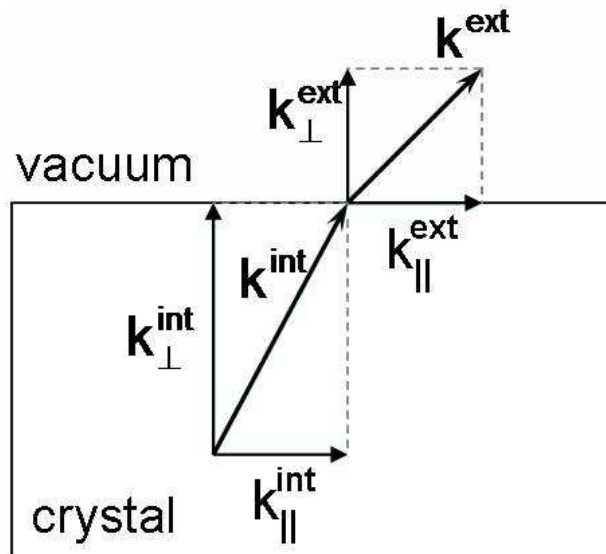


Figure.2.10: Momentum relations at the crystal vacuum interface. Only the parallel component of electron wave vector (k_{\parallel}) is conserved in this transition. The perpendicular component does not follow any lattice periodicity condition [99].

2.2.3. X-ray photoelectron spectroscopy (XPS)

XPS is also known as electron spectroscopy for chemical analysis (ESCA) or core level photoelectron spectroscopy (CLPES). The core level electrons can be excited by using incident photon of high energy. The kinetic energy of the emitted photoelectron can be calculated from Eq.2.24. For all materials, the binding energy of core level electrons lies in the range from tens of electron volts to thousands of electron volts. Hence the excitation energies of light in the region of X-rays (soft x-rays with energies below about 2KeV) are used. Therefore this method is called XPS. The name ESCA is due to the identification of chemical composition of elements in the sample. Different from ARPES where ultra violet light is used (less than 100eV), XPS radiation source is typically the $K\alpha$ X-ray radiation from Aluminum (1486.6eV) or Magnesium (1252.6eV)

A typical XPS spectrum plots the number of photoelectrons detected as a function of the binding energy. Each element produces a characteristic set of XPS peaks at characteristic binding energy values that directly identify each element that exist in or on the surface of the material being analyzed. These characteristic peaks correspond to the

Chapter 2. Experimental Techniques

configuration of electrons inside the atom, e.g. 1s, 2s, 2p, 3s etc. The different electron densities can also result in a shift of the energy of the characteristic peaks, which provides information about the particular chemical environment of the atoms on the surface. The intensity of the characteristic peaks is directly related to the amount of element within the area or volume probed and the sensitivity factor of the elements in the photoemission process. Thus XPS can yield quantitative information about the elemental composition of the surface, the empirical formula of pure materials, chemical and electronic state of the elements in the surface and the thickness of thin film on a different substrate within the probing depth ($\approx 10\text{nm}$ of the surface).

The main peak in the XPS spectrum is resulting from the photoelectron process. The characteristic background of the XPS spectrum is mainly due to the inelastically scattered electrons. Auger electrons can also be detected in the spectrum. During the excitation of photoelectron a core hole is created and this vacancy is filled by an electron from higher shell. At the same time a second electron (Auger electron) is emitted from the sample with a kinetic energy equals to the difference between the energy of the initial core hole and the doubly charged remaining atom. In addition to the photoelectron and auger electron, some additional second order features are also observed. Satellite peaks are also observed that originate from the emission spectrum of a non monochromatic X-ray source [99].

The first step in XPS data processing is identification of chemical element present at the surface by comparing the measured peak positions to reference spectra. For p,d,f peaks two peaks are observed due to the spin orbital splitting. This spin orbit splitting and peak area ratios assist in element identifications. From the accurate determination of peak position one can determine the chemical state of an atom as the chemical environmental of a particular atom affects the binding energy of its core levels. A specific chemical shift is the difference in binding energy values of one specific chemical state versus the binding energy of the pure element.

Chapter 2. Experimental Techniques

2.2.4. Experimental set up

The PES (XPS and ARPES) measurements in this thesis were carried out at the CASSIOPEE beamline at SOLEIL synchrotron radiation source using a Scienta R4000 electron spectrometer. Below a brief description about the Synchrotron radiation and CASSIOPEE beamline is given.

2.2.4.1. Synchrotron radiation

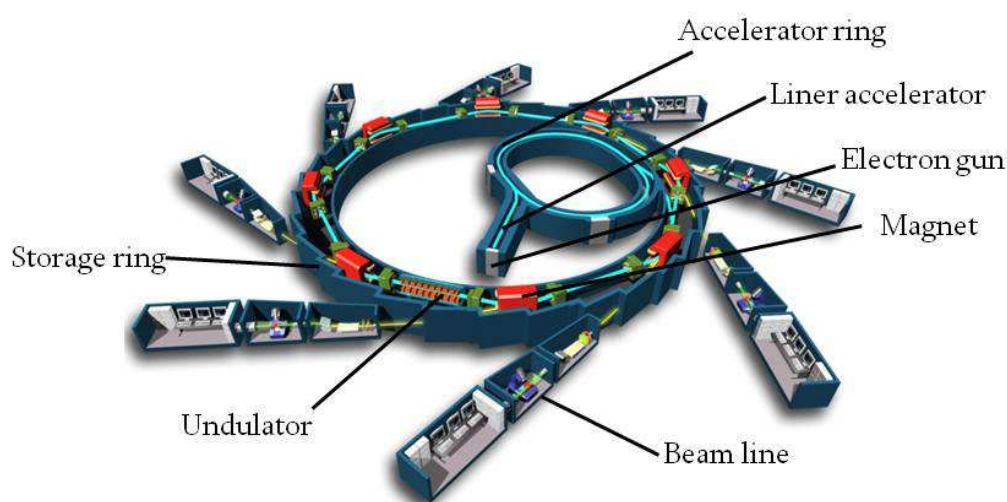


Figure.2.11: Schematic of synchrotron radiation [103].

When a charged particle is accelerated by an external electric field, the electromagnetic radiation emitted is called synchrotron radiation. Schematic of synchrotron radiation is shown in Figure 2.11. Electrons are emitted from the electron gun, which usually consists of a cathode and anode, and are then linearly accelerated. After the initial acceleration, they are further accelerated in a second accelerator ring and then guided into the storage ring. In the storage ring, the magnetic devices (dipole magnet or undulators-alternatively polarized dipole magnets), control the trajectory of electrons or make them to oscillate. Then the electrons lose its energy in the form of light, the synchrotron radiation. These emitted photons are guided through optical elements towards the experimental stations called beamlines.

2.2.4.2. CASSIOPEE beamline

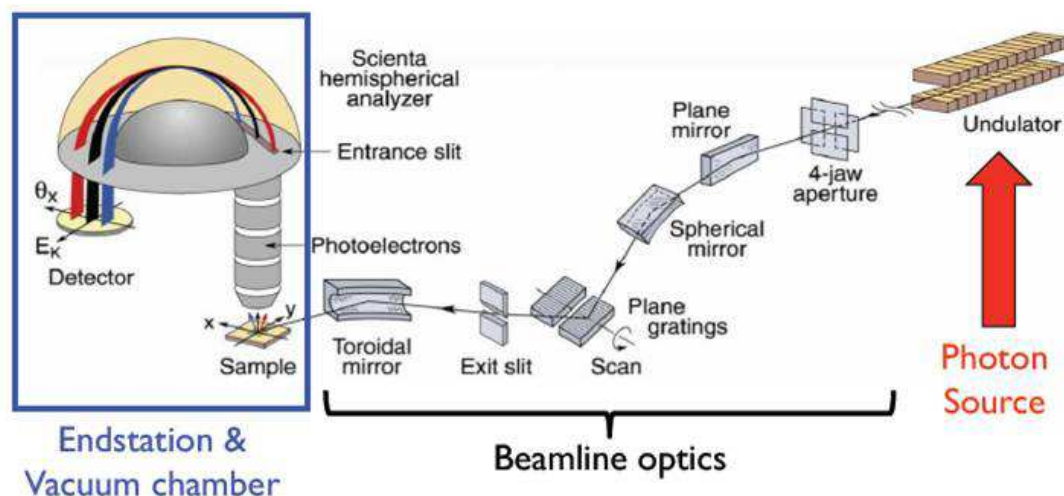


Figure.2.12: Layout of a synchrotron beamline [103].

All the measurements in this thesis were done at CASSIOPEE beamline. The energy range in this beam line is 8eV-1500eV allows both surface and bulk studies. Two undulators are used as source with high flux and adjustable polarization. The optical system consists of a plane grating monochromator with variable line spacing and variable groove depth gratings. After the monochromator, the photons are supplied to two end stations (High resolution Angle-resolved photoemission and spin-resolved photoemission) and both are connected to a Molecular Beam Epitaxy (MBE) chamber for sample growth and characterization. The temperature can vary from 4 to 400K at high resolution angle resolved photoemission set up and Scientia R4000 electron analyzer is used for detection of photoelectrons whose angular acceptance is $\pm 15^\circ$. The angle resolved photoemission setup is equipped with computer controlled 4-axis sample holder, with x,y,z translations and θ rotations. And the sample can cool down to 4K with a liquid He cryostat.

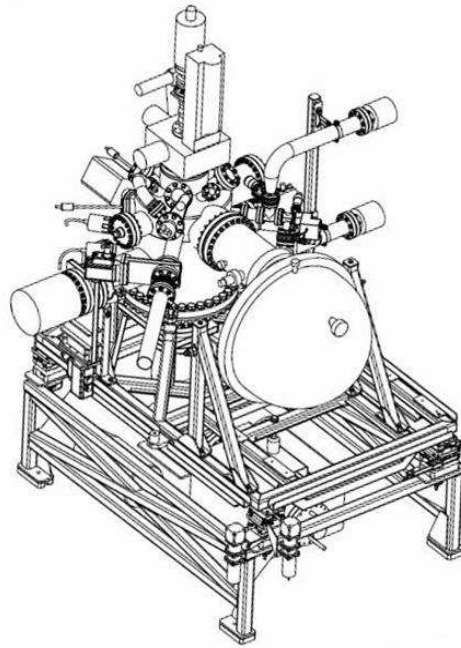


Figure.2.13: Scheme of CASSIOPEE high resolution angle resolved photoemission experimental setup [103].

The graphene samples were introduced into the preparation chamber and degassed at 600°C for several minutes and then characterized by LEED in order to verify the Γ K or Γ M direction of first Brillouin zone. After that, the sample is transferred to ARPES chamber and the spectra were recorded using a Scienta R4000 electron analyzer at photon energy of 60eV with an overall energy resolution of around 30meV at a temperature of 10K.

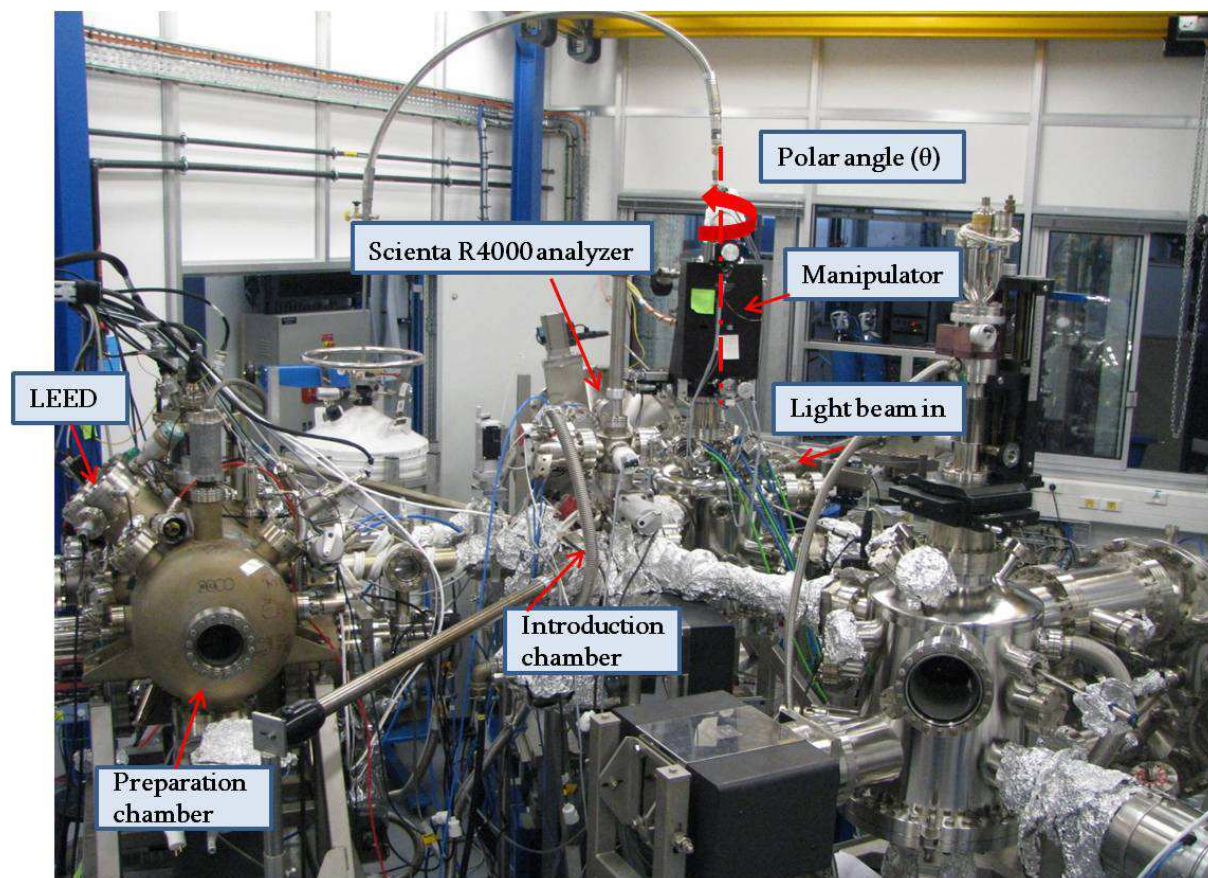


Figure.2.14: Photoemission experimental setup at the CASSIOPEE beamline at SOLEIL synchrotron radiation source in Paris.

2.3. One-Photon (1PA) and Two-Photon (2PA) Absorption techniques

To understand the intrinsic electronic and structural properties of organic chromophores (Diarylethenes and Oligothiophenes) which were deposited on the surfaces, various photochemical measurements have been carried out in solution: A brief theoretical and experimental description of these related techniques are discussed below.

2.3.1. UV-Visible absorption spectroscopy

When light interacts with matter, a number of processes can occur, including reflection, scattering, absorbance, fluorescence or phosphorescence and photochemical reaction. Absorption of light by matter causes the energy content of the molecules (or

Chapter 2. Experimental Techniques

atoms) to increase. The total potential energy of a molecule generally is represented as the sum of its electronic, vibrational, and rotational energies:

$$E_{total} = E_{electronic} + E_{vibrational} + E_{rotational} \quad (\text{Eq.2.33})$$

The amount of energy a molecule possesses in each form is not a continuum but a series of discrete levels or states. The differences in energy among the different states are in the order:

$$E_{electronic} > E_{vibrational} > E_{rotational} \quad (\text{Eq.2.34})$$

In some molecules and atoms, photons of UV and visible light have enough energy to cause transitions between the different electronic energy levels. The wavelength of light absorbed is that having the energy required to move an electron from a lower energy level to a higher energy level

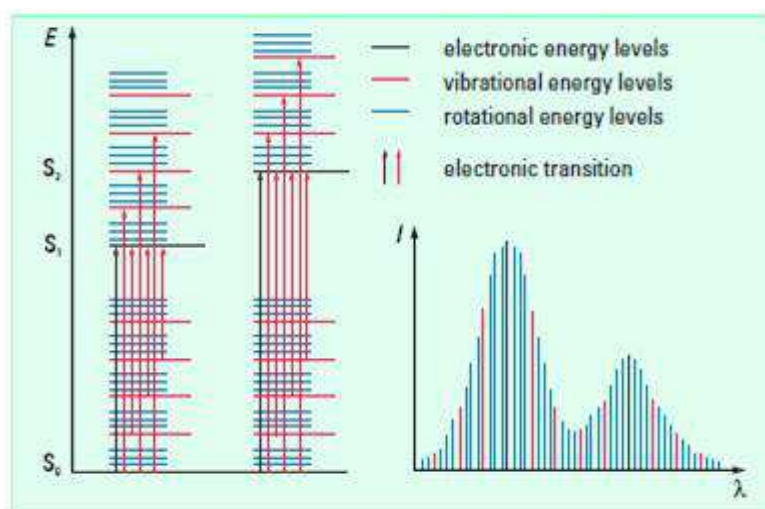


Figure.2.15: Electronic transitions and UV-visible spectra of molecules [104].

When light passes through or is reflected from a sample, the amount of light absorbed is the difference between the incident radiation (I_0) and the transmitted radiation (I). The amount of light absorbed is expressed as either transmittance or absorbance.

Chapter 2. Experimental Techniques

$$A(\lambda) = \log \frac{I_{\lambda}^0}{I_{\lambda}} = -\log T(\lambda) \quad (\text{Eq.2.35})$$

$$T(\lambda) = \frac{I_{\lambda}}{I_{\lambda}^0} \quad (\text{Eq.2.36})$$

$$A(\lambda) = \log \frac{I_{\lambda}^0}{I_{\lambda}} = \varepsilon(\lambda)cl \quad (\text{Eq.2.37})$$

where I_{λ}^0 and I_{λ} are the light intensities of the beams entering and leaving the absorbing medium, $\varepsilon(\lambda)$ is the molar absorption coefficient (commonly expressed in $\text{L mol}^{-1} \text{cm}^{-1}$) and c is the concentration (in mol L^{-1}) of absorbing species and l is the absorption path length (thickness of the absorbing medium) (in cm). This is known as the Beer–Lambert Law. For most applications, absorbance values are used since the relationship between absorbance and concentration and path length are linear [105].

For electronic transitions, the energy difference between ground and excited states is quite large. Therefore, at room temperature, most of the molecules are in the electronic ground state. Absorption and de-excitation are fast processes, and equilibrium is reached very quickly. Thus, absorption of UV-visible light is quantitatively highly accurate. The simple linear relationship between absorbance and concentration and the relative ease of measurement of UV-visible light have made UV-visible spectroscopy the basis for thousands of quantitative analytical methods.

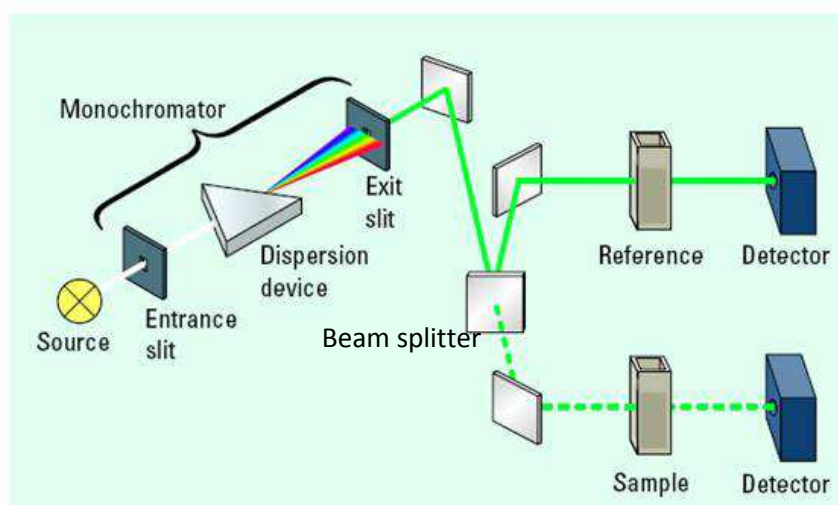


Figure.2.16: Schematic of a spectrophotometer [104].

Chapter 2. Experimental Techniques

Figure.2.16 shows a schematic diagram of spectrophotometer. A spectrophotometer is an instrument which measures the absorbance or transmittance of a sample as a function of wavelength of electromagnetic radiation. A typical spectrometer consists of a source, which is a deuterium or halogen lamp that generates a broad band of electromagnetic radiation, a dispersion device, contains a holographic grating that select a particular wavelength from a broad radiation of the source, sample area and photo-detectors to measure the intensity of radiation. After passing through the exit slit of monochromator, radiation passes to the spherical mirror and then reflected onto the beam splitter which allows 50% of the radiation pass through to a planar mirror and then reflected to the sample cuvette and focused onto sample photo-diode detector. The other half of radiation pass through another plane mirror and focused on to the reference cuvette and then passed to reference photo-diode. The transmittance or absorbance is determined by measuring both the intensity of the incident radiation I_0 (without the sample) and the transmitted intensity I (with the sample) using equations (Eq.2.35-2.37). Because most samples are measured in solution, the blank should be measured on a cuvette containing the pure solvent used to prepare the sample. This process eliminates from the sample measurement any absorbance due to the solvent. With a split-beam instrument, both cuvettes are initially filled with pure solvent, and a so-called balance measurement is performed. This measurement reflects the difference in absorbance between the two optical paths in use. The sample cuvette is then filled with the sample solution for measurement, and I_0 and I are measured virtually simultaneously. The resulting spectrum is corrected by subtracting the balance spectrum.

2.3.2. Fluorescence spectroscopy

Once a molecule is excited by absorption of a photon, it can return to the ground state by emission of fluorescence. Nevertheless many other pathways the de-excitation can occur which are internal conversion (direct return to ground state without emission fluorescence), intersystem crossing (possibly followed by emission of phosphorence),

Chapter 2. Experimental Techniques

intramolecular charge transfer and conformational change. All the radiative and non radiative transitions are represented using the Perrin-Jablonski diagram shown below.

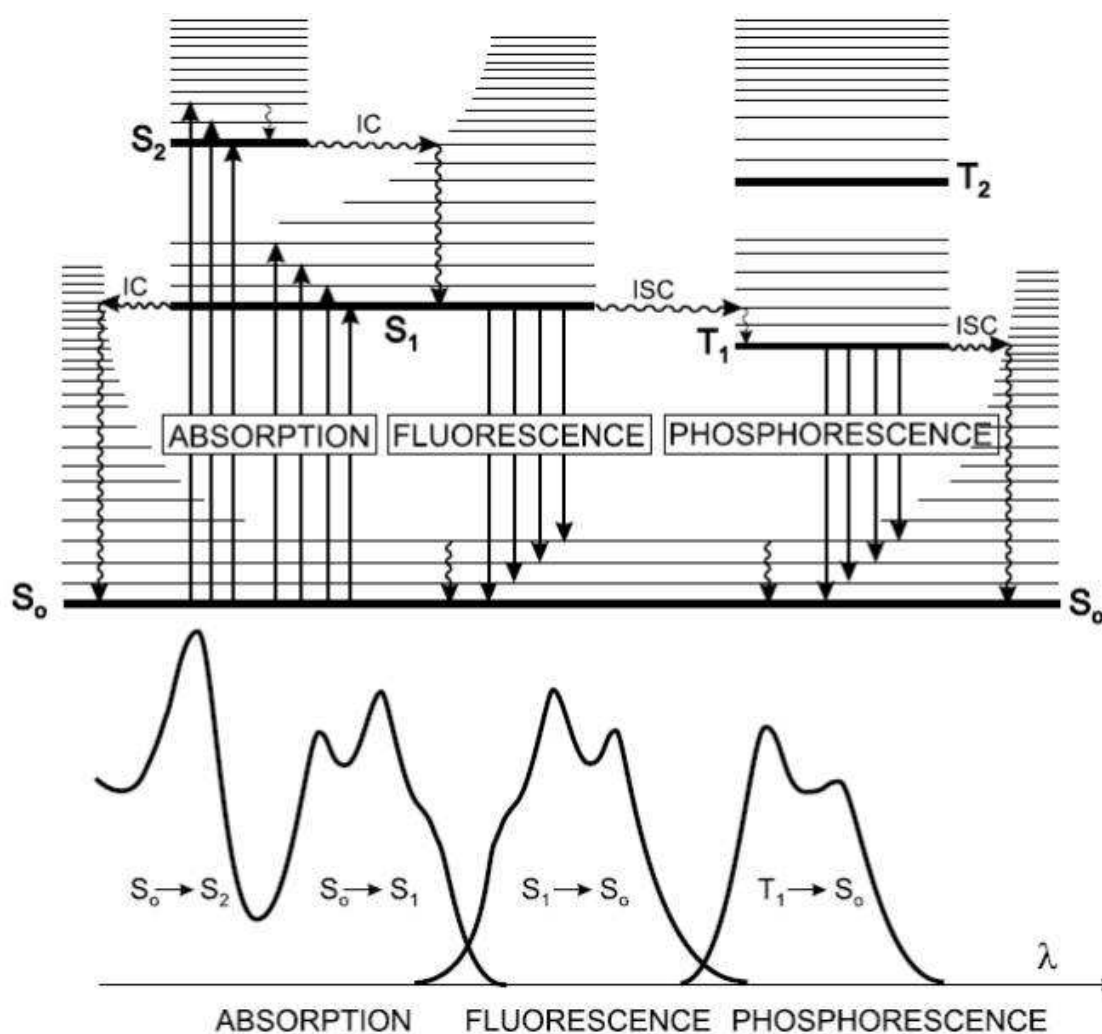


Figure.2.17: Perrin-Jablonski diagram and detail of relative positions of absorption, fluorescence and phosphorescence spectra. The singlet electronic states are denoted as S_0, S_1, S_2 and the triplet states are T_1, T_2 . Vibrational levels are associated with each electronic state [105].

When a molecule undergoes de-excitation from S_1 - S_0 with the emission of a photon is called fluorescence. Fluorescence occurs from S_1 state therefore its characteristics do not depend on the excitation wavelength. The fluorescence spectrum is located at higher wavelengths (lower energy) than the absorption spectrum. This is because of the energy loss in the excited state due to vibrational relaxation. However, in most cases, the absorption spectrum partly overlaps the fluorescence spectrum which means a part of

Chapter 2. Experimental Techniques

light is emitted at short wavelength than the absorbed light. This is because at room temperature a small fraction of molecules in a vibrational level higher than level 0 in the ground state as well as in the excited state. At low temperature, this should disappear. In general, the differences between the vibrational levels are similar in the ground states and the excited states, so the fluorescence spectrum resembles the first absorption band. This is called mirror image rule. The difference between the maximum of first absorption band and the maximum of fluorescence band is called Stokes-Shift. However molecules lose the mirror symmetry due to the change in the conformation which will be discussed in chapter 5. However the emission of a photon is as fast as absorption of a photon ($\approx 10^{-15}$ s), the molecules stay in the excited state for a certain time (a few tens of picoseconds to a few hundreds of nanoseconds) before de-excitation. Thus after excitation of a population of molecules by a very short pulse of light, the fluorescence decreases exponentially with a characteristic time, reflecting the average lifetime of molecules in the excited state referred to as excited-state life time. Such intensity decay is comparable with radioactive decay with a characteristic time called the radioactive period, indicating the average lifetime of a radioelement before disintegration. Therefore τ_s , the lifetime of a molecule in excited state S_1 is given by $\tau_s = \frac{1}{k_r^s + k_{nr}^s}$, where k_r^s is the rate constant for radiative deactivation (S_1-S_0) with emission of fluorescence. k_{nr}^s is the rate constant for non-radiative deactivations from S_1 which includes intersystem crossing (k_{isc}) and internal conversion (k_{ic}^s). Therefore ($k_{nr}^s = k_{ic}^s + k_{isc}$). Intersystem crossing (Isc) is a non-radiative transition between two isoenergetic vibrational levels of electronic states with different multiplicities (Figure.2.17). For instance, an excited state molecule in the 0 vibrational level of the S_1 state can move to the isoenergetic vibrational level of the T_n triplet state. Then the vibrational relaxation brings it into the lowest vibrational level of T_1 . Crossing between states of different multiplicity is forbidden, however spin-orbit coupling can be large enough to make it possible. Internal conversion is also a non-radiative transition between two electronic states of the same spin multiplicity. When a molecule is excited to an energy level higher than the lowest vibrational level of the first electronic state, vibrational relaxation (and internal conversion if the singlet excited state is higher than

Chapter 2. Experimental Techniques

S₁) leads the excited molecule towards the 0 vibrational level of the S₁ singlet state with a time-scale of 10⁻¹³–10⁻¹¹ s. From S₁, internal conversion to S₀ is possible but is less efficient than conversion from S₂ to S₁, because of the much larger energy gap between S₁ and S₀. Therefore, internal conversion from S₁ to S₀ can compete with emission of photons (fluorescence) and intersystem crossing to the triplet state from which emission of photons (phosphorescence) can possibly be observed.

Therefore, one can obtain the fluorescence quantum yield if we know the excited-state life time. The fluorescence quantum yield is the fraction of excited state molecules that return to the ground state S₀ with the emission of photons, which is give by

$$\phi_F = \frac{k_r^S}{k_r^S + k_{nr}^S} = k_r^S \tau_S \quad (\text{Eq.2.38})$$

In other words, ϕ_F is the ratio of number of emitted photons to number of absorbed photons.

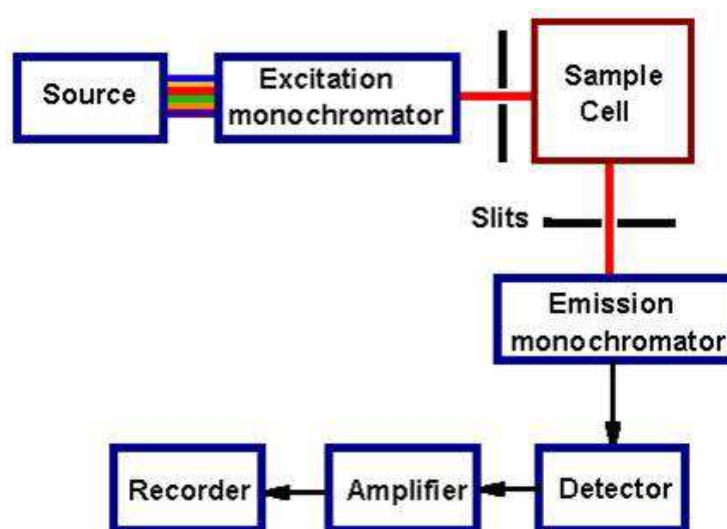


Figure.2.18: Schematic of a spectrofluorometer.

A typical spectrofluorometer contains an excitation source, a sample cell and a fluorescence detector. The excitation source is usually a deuterium or xenon lamp. The broad -band excitation light from the lamp passes through a monochromator, which only passes a selected wavelength. The fluorescence is dispersed by another monochromator and

Chapter 2. Experimental Techniques

detected by a detector. Scanning the excitation monochromator gives the excitation spectrum while scanning the fluorescence monochromator gives the fluorescence spectrum.

2.3.3. Two-photon absorption spectroscopy (2PA)

The principle of simultaneous absorption of two photons by the same chromophore was originally predicted in the 30s by the physicist Maria Göppert-Mayer [106]. Thirty one years later, after the invention of first laser device, Kaiser and Garrett reported the first observation of a 2PA-induced fluorescence of crystals $\text{CaF}_2:\text{Eu}^{2+}$ [107].

Two types of absorption process are occurred. A process called ‘non-degenerate’ corresponding to the absorption of two photons of different energies and the process ‘degenerate’ into which the two photons have same energy. This second process is the most commonly used one.



Figure.2.19: Non-degenerate and degenerate two photon absorption process.

At the macroscopic scale, the two-photon absorption is a nonlinear optical property of the material that must be connected to the imaginary part of the tensor components of the third order electric susceptibility $\text{Im}(\chi^{(3)})$. Indeed, if we recall that, under the influence of an external electric field \mathbf{E} , the polarization \mathbf{P} of a material is described by the expression

$$\mathbf{P} = \mathbf{P}_0 + \epsilon_0 \left(\underbrace{\chi^{(1)} \mathbf{E}}_{\text{Linear Polarization}} + \underbrace{\chi^{(2)} \mathbf{E} \cdot \mathbf{E} + \chi^{(3)} \mathbf{E} \cdot \mathbf{E} \cdot \mathbf{E} + \dots}_{\text{Non linear Polarization}} \right) \quad (\text{Eq.2.39})$$

where ϵ_0 is free-space permittivity, the odd-order susceptibilities ($\chi^{(1)}, \chi^{(3)} \dots$) involved in the dissipative process, which is the energetic exchange between the electric fields and the material. The imaginary part of each tensor then corresponds to absorption phenomenon. Therefore, one (1PA) and two (2PA) photon absorption is described by $\chi^{(1)}$ and $\chi^{(3)}$.

General relationship between the two-photon absorption cross section (δ) and imaginary part $\chi^{(3)}$ is given by

$$\delta = \frac{8\pi^3 h \nu^2}{\epsilon_0 n^2 c^2} \text{Im}(\chi^3) \quad (\text{Eq.2.40})$$

where h, c and n are the plank's constant, velocity of light and refractive index of the material. The unit of 2PA cross section is GM, the abbreviation of Göppert-Mayer and defined by $1\text{GM} = 10^{-50} \text{cm}^4 \cdot \text{s} \cdot \text{photons}^{-1} \cdot \text{molecule}^{-1}$.

At the molecular scale, the local field of the chromophore \mathbf{F} differs from the external electric field \mathbf{E} . This is explained by the additional perturbations induced by the neighboring dipoles. The effects of \mathbf{F} on the dipole moment of the chromophore are described by

$$\boldsymbol{\mu} = \boldsymbol{\mu}_0 + \epsilon_0 \left(\underbrace{\alpha \cdot \mathbf{F}}_{\text{Induced linear polarization}} + \underbrace{\frac{1}{2} \beta \cdot \mathbf{F} \cdot \mathbf{F} + \frac{1}{6} \gamma \cdot \mathbf{F} \cdot \mathbf{F} \cdot \mathbf{F} + \dots}_{\text{Induced nonlinear polarization}} \right) \quad (\text{Eq.2.41})$$

where α is the linear polarizability, β and γ are the hyperpolarizabilities of the first and second order (tensor of rank 3 and 4). Similarly, the cross section of two-photon

Chapter 2. Experimental Techniques

absorption will be described by the imaginary part of the tensor components. This leads to the general relation.

$$\delta = \frac{8\pi^3 h\nu^2}{\epsilon_0 n^2 c^2} L^4 \text{Im}(\gamma) \quad (\text{Eq.2.42})$$

where L is the local field factor, $\mathbf{F} = L\mathbf{E}$. In the so called Lorentz-Lorentz approximation [108] (polar and non-isotropic material), $L = (n^2 + 2)/3$.

The hyperpolarizability γ of a chromophore can be theoretically evaluated by the method of perturbations called sum-over-states (SOS) which provides a general expression based on summation over all excited states [109]. This calculation requires knowledge of energies (E_{0i}), dipole moments (μ_i) and transition moments (M_{ij}) associated with each excited state considered. These parameters are calculated by quantum methods of configuration interaction from the optimized structure of the chromophore kind. The SOS method allows determining the contribution of each excited state to the nonlinear response of the chromophore. Depending on the geometry and structure of the chromophore, one can observe that the second order hyperpolarizability can reduce the contribution of two or three states. The address of the electronic and geometric structure of the chromophore allows to exalting the properties of the two photon absorption.

The measurements of two photon absorption have been performed using the two photon induced fluorescence technique (2PIF). The diagram of the experimental setup is shown in Figure 2.20.

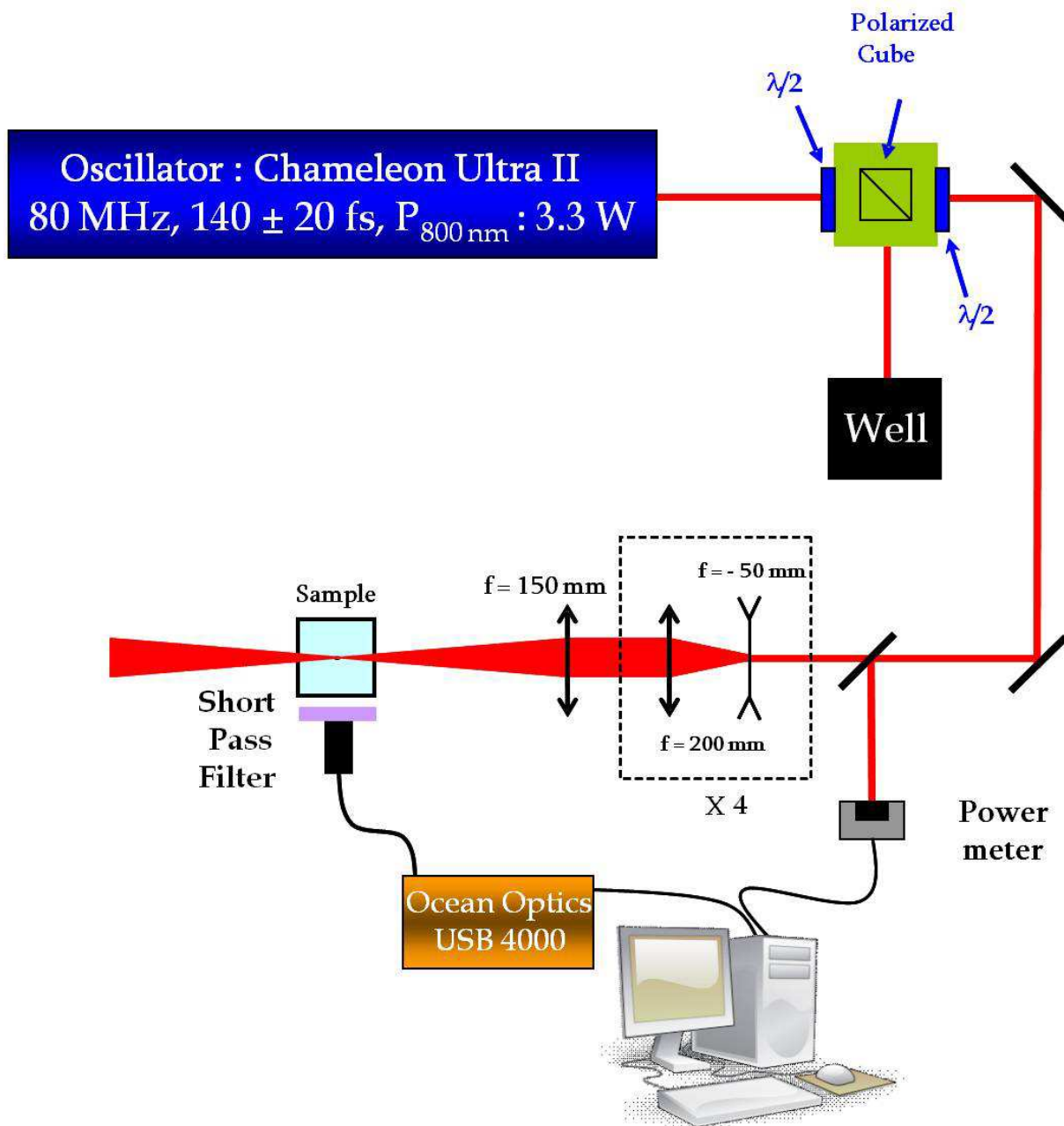


Figure.2.20: Experimental setup of 2PA.

The two-photon absorption measurements were performed with femtosecond mode-locked laser pulse using a Ti: Sapphire laser (Coherent, Chameleon Ultra II: pulse duration: ~ 140 fs; repetition rate: 80 MHz; wavelength range: 680-1080 nm). A relative two-photon-induced fluorescence (2PIF) method [110] was employed to measure the two-

Chapter 2. Experimental Techniques

photon absorption cross-sections δ . A 10^{-4} M solution of fluorescein [111] in water at pH = 11 was used as the reference (r). The value of δ for a sample (s) is given by:

$$\delta_S = \frac{S_S \Phi_r \eta_r C_r}{S_r \Phi_S \eta_s C_S} \cdot \delta_r \quad (\text{Eq.2.43})$$

where S is the detected two-photon induced fluorescence integral area, c the concentration of the chromophores, and Φ is the fluorescence quantum yield of the chromophores. η is the collection efficiency of the experimental set-up and accounts for the wavelength dependence of the detectors and optics as well as the difference in refractive indices between the solvents in which the reference and sample compounds are dissolved. The measurements were conducted in a regime where the fluorescence signal showed a quadratic dependence on the intensity of the excitation beam, as expected for two-photon induced emission. For the calibration of the two-photon absorption spectra, the two-photon induced fluorescence signal of each compound was recorded at the same excitation wavelength (λ_{exc} : 782 nm) as that used for fluorescein.

Abstract: Chapter 3. Intercalation of gold on Epitaxial Graphene

Abstract: Chapter 3. Intercalation of gold on Epitaxial Graphene

Dans ce chapitre nous présentons les résultats concernant l'intercalation d'or. Le dépôt d'or sur une ML de graphène suivi de cycles de recuits conduit à l'intercalation d'atomes d'or sous la couche de graphène et au dessus de la couche tampon. La position exacte de l'intercalation faisait encore l'objet d'une controverse qui est maintenant levée dans ce chapitre. Différents types d'intercalation sont observés, soit sous la forme d'une monocouche d'or avec une structure Moiré 13x13 donnant un dopage de type p, soit sous la forme de clusters dilués. D'autres formes d'intercalation plus complexe sont également présentées mais n'ont pas fait l'objet d'une étude détaillée. Dans ce chapitre, par photoémission et la confrontation d'images STM avec des images calculées DFT, nous montrons sans ambiguïté que ces clusters correspondent à des atomes d'or individuels. Ces atomes d'or ne sont ni liés à la couche de graphène, ni à la couche tampon au dessous. Ils génèrent des figures d'interférence d'onde stationnaire interprétée comme des effets d'écrantage avec les électrons provenant du substrat avec le dopage intrinsèque du graphène épitaxié. Ces ondes ont été dans un premier temps associées à une modification importante de la structure de bande du graphène au niveau des singularités de van Hove par l'interprétation en densité d'états joint des transformé de Fourier des figures d'interférence. Ces résultats sont décrits ici. Des mesures de photoémission résolue en Angle réalisées sur le synchrotron Soleil ont permis de mesurer toute la dispersion de bande et la surface de Fermi autour du point M. Une extension importante des singularités de Van Hove a été confirmée. Les mesures de dispersions montrent que le graphène garde ses propriétés électroniques fondamentales avec une dispersion linéaire et de façon inattendue une augmentation de la vitesse de Fermi de plus de 20% par rapport à la vitesse de Fermi initiale avant intercalation d'or. Confirmant les mesures de spectroscopie locales en STS aucun dopage n'est observé dans le cas des atomes d'or isolés, nous observons par contre une forte renormalisation des vitesses de Fermi au voisinage du point de Dirac. Nous discutons tous ces aspects en terme de transfert de charge. Par analogie

Abstract: Chapter 3. Intercalation of gold on Epitaxial Graphene

avec les graphites intercalés et l'observation de la supraconductivité pour ces structures hybrides, nous tentons d'évaluer la constante de couplage attendue par l'extension des singularités de van Hove observée si on arrivait à doper fortement le système et à amener le niveau de Fermi autour des singularité en supposant que les bandes soient suffisamment robustes. Nous estimons la température de transition supra qui pourrait être observée dans le cadre d'un tel système. Le fait que le système n'est pas dopé malgré la présence des atomes d'or est expliqué par une compensation du niveau de dopage par la normalisation des cônes de Dirac. Nous montrons enfin comment les atomes de clusters dilués découplent la couche de graphène du substrat et suppriment efficacement l'effet de rugosité induite par la couche tampon sous jacente.

Chapter 3. Intercalation of gold on Epitaxial Graphene

3. Intercalation of gold on Epitaxial Graphene (EG)

A prerequisite for the development of EG based nanoelectronics is the precise control of carrier type and concentration. This can be achieved externally by applying gate [112-113] and internally by doping. P-type doping of epitaxial graphene layer on silicon carbide substrate by adsorption of bismuth, antimony or gold was first reported by Gierz *et al.*, in 2008 [88]. Then, the next year, our group evidenced the gold intercalation process on epitaxial graphene on SiC [83]. During the same year, hydrogen intercalation on EG on SiC was also reported, for decoupling the buffer layer from the SiC substrate [66]. Following us, several other intercalation processes were performed on EG. Many intercalations such as Na [81], F [82], Bi, Sb and Au [84] were performed at the interface of G/SiC. In these cases, intercalation occurs during the annealing process of carbon-rich SiC(0001) reconstruction. However our intercalation process is different from above. In our case, the deposition of gold is done after the formation of the graphene monolayer leading to the intercalation between the top graphene layer and the buffer layer. McChesney *et al.* [89] also reported Ca and K intercalation under monolayer graphene using the same procedure of us.

This chapter is organized as followed. The first part discuss the process of intercalation and presents different types of intercalation depending on the preparation conditions. We will then focus on the “diluted phase” and “film phase”, the position of the intercalated gold atoms and their “free standing nature” with the help of calculated projected density of states (PDOS) in comparison with X-ray photoelectron spectroscopy (XPS). We will then show, how the gold intercalation modifies the band structure of the top graphene layer, in the vicinity the Dirac point and around the Van Hove singularities (M points). The Fermi surface at different energies was obtained by Angle Resolved Photoemission Spectroscopy (ARPES) done on synchrotron Soleil; results will be compared to previous interpretation of Fourier Transform Scanning Tunneling Spectroscopy measurement (FT-STs). Finally, the decoupling of monolayer graphene from SiC(0001) substrate is demonstrated.

Chapter 3. Intercalation of gold on Epitaxial Graphene

3.1. Method of gold intercalation on EG

Preparation of EG on SiC(0001) was discussed in chapter 1. After the graphene sample preparation, gold (~ 60 Å) was deposited at room temperature using a homemade Knudsen cell and calibrated with a quartz crystal microbalance. The measured deposition rate was 0.2 Å per minute. After gold deposition, the sample was annealed at 1000 K for 2 minutes. Further, physical characterization of the sample was performed using a Low Temperature-Scanning Tunneling microscopy (LT-STM) from Omicron at 77 K at a base pressure in the 10^{-11} mbar range. The images were acquired using a lock-in amplifier and a modulation voltage of ± 20 mV.

3.2. Modes of gold intercalation on EG

After the gold deposition and annealing of the sample, large 3D islands of gold atoms were observed on the sample surface as shown in Figure 3.1a. These islands were not stable and we got a lot of difficulties to image them. After several cycles (≈ 15) of annealing at 750°C , these large gold islands almost disappeared and completely different structures were observed on the surface. These new structures were attributed to the intercalation of gold atoms due to the diffusion of gold through step edges and ripples of EG. Indeed, the area of graphene with intercalated gold is always surrounded by rims. These rims are connected to large islands which are probably pinned by structural defects. Gold islands appear to be the source of gold, which is provided by the rims and the diffusion starts and occurs from the step edges. The main conclusion concerning the intercalation process of gold is that gold needs defects to reach the intercalation space between the top graphene layer and the substrate.

For the first stage of intercalation, without further addition of gold, we observed two intercalation modes. One consists of pseudo-regularly dispersed aggregates of gold which looks like an Ostrich leather (OL) or also called as diluted phase (DP). The second seems to consist of a continuous monolayer of gold called as film phase (FP) as shown in Figure 3.1b-c.

Chapter 3. Intercalation of gold on Epitaxial Graphene

For the second stage, two other phases are obtained by the addition of gold atoms and annealing cycles, which are stripe phase (SP) and half balls phase (HP) are depicted in Figure 3.2. All these structures are strongly related to the liquid phase transition in 2D solid. However, these patterns are quite similar in [114] but the phenomenology is beyond the scope of this thesis.

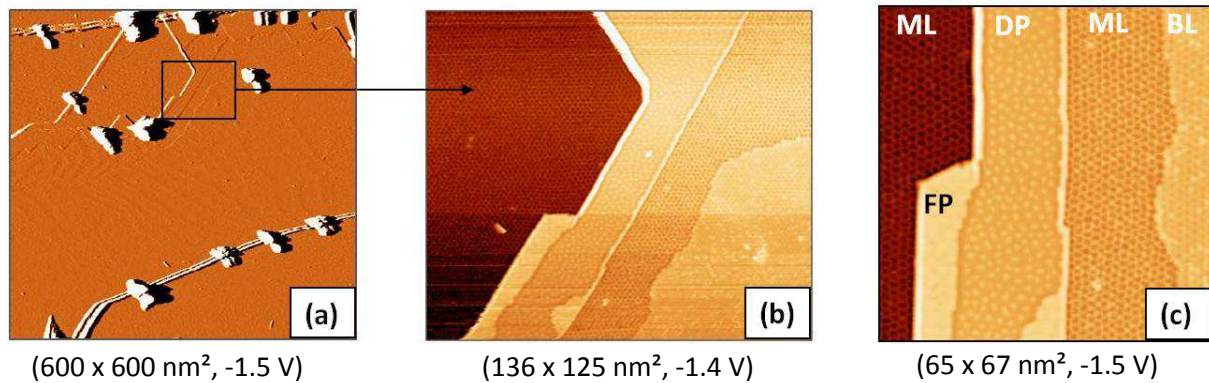


Figure.3.1: STM images of gold intercalated EG. (a) shows the large 3D islands of gold on the surface ($\frac{\partial z}{\partial x}$ -derivative representation of topography), (b) shows the zoom in (a) where the new gold intercalated structures are formed, (c) shows the two different modes of intercalation, diluted phase (DP) and film phase (FP). Monolayer (ML) and bilayer (BL) of graphene are also marked.

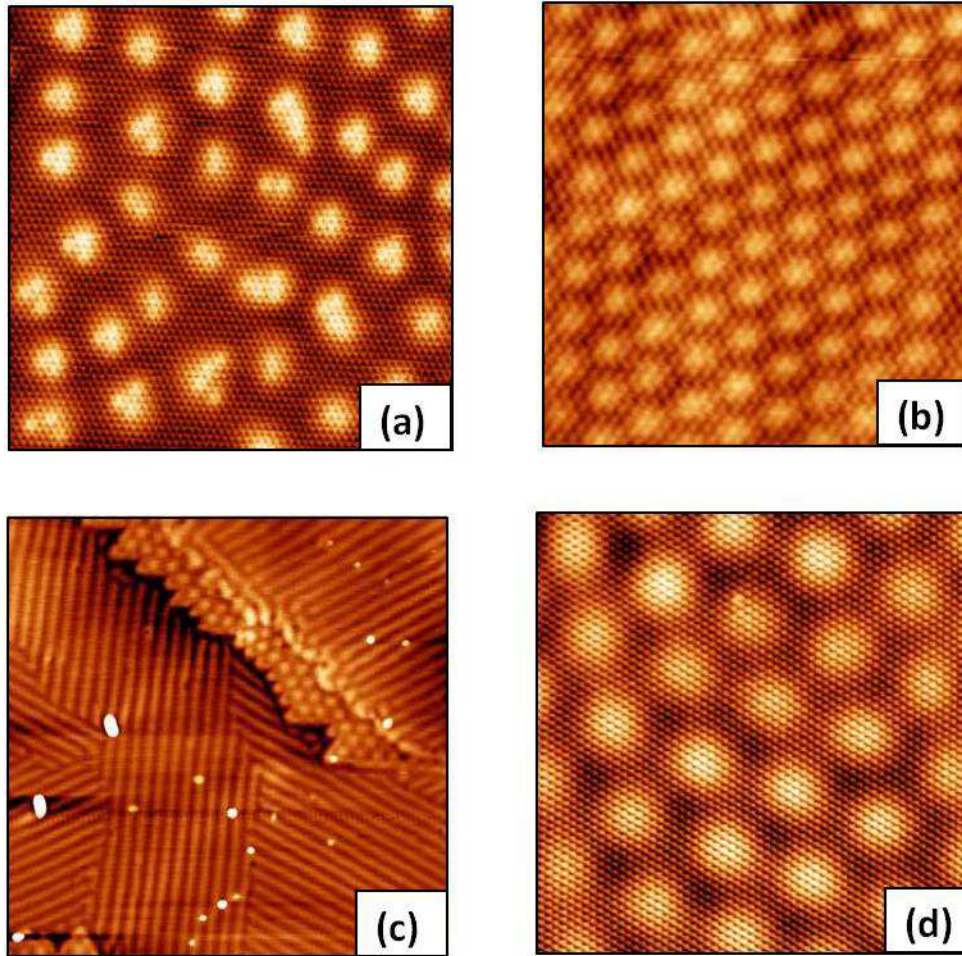


Figure.3.2: STM topographic images of all modes of intercalation. (a) shows diluted phase (DP) ($12\text{nm}\times 12\text{nm}$, -1.6V) (b) shows film phase (FP) ($7.5\text{nm}\times 7.7\text{nm}$, -0.5V) (c) stripe phase (SP) ($70\text{nm}\times 70\text{nm}$, 1.5V) and (d) half balls phase (HP) ($12\text{nm}\times 12\text{nm}$, -0.73V).

3.3 Characterization of film phase (FP)

After the intercalation of gold, 80% of the sample surface was covered with intercalated gold clusters (DP) and the rest of 20% was with a continuous monolayer of gold (FP) and pristine monolayer. Figure 3.3. shows the topographic STM images of FP. In Figure 3.3.b, only one per two carbon atoms can be observed at low bias voltage whereas, at higher bias voltage (not shown) all six carbon atoms were observed. This is the characteristic of a bilayer graphene [115], hence FP is also called ‘bilayerlike’ region (BLL). The gold monolayer weakens the contrast between A and B sub lattices in graphene explains the ‘bilayerlike’ appearance of this region when biased at low voltages.

Chapter 3. Intercalation of gold on Epitaxial Graphene

However, the BLL or FP region is different from the conventional bilayer graphene as shown in Figure.3.3.c. This image shows a regular pattern of bright structures with a 13×13 -G super cell, equivalent to a 12×12 -Au super cell.

Also smaller dots with an average radius of 1 nm display a $2\sqrt{3} \times 2\sqrt{3}R30$ -Au reconstruction, which refers to a gold-gold distance $d_{\text{Au-Au}} = 2.66 \text{ \AA}$. Thus, FP consists of two types of reconstructions; 13×13 -G reconstruction (3.19 nm) and a $2\sqrt{3} \times 2\sqrt{3}R30$ -Au reconstruction (0.92 nm).

The origin of the 13×13 -G surface reconstruction (big blue diamond in Figure 3.3.c) arise from a Moiré pattern resulting from the superposition of the two planes: one gold monolayer with a gold-gold distance of 2.66 \AA and one graphene monolayer as schematized in Figure 3.3. Though the model (Figure 3.3.d), certainly explains the 13×13 reconstruction in this bilayerlike region, it does not explain the observed $2\sqrt{3} \times 2\sqrt{3}R30$ structure (small blue diamond in Figure 3.3.c). It is assumed that this modulation corresponds to a surface corrugation of the gold layer and an inhomogeneous transfer of charge with the top graphene layer.

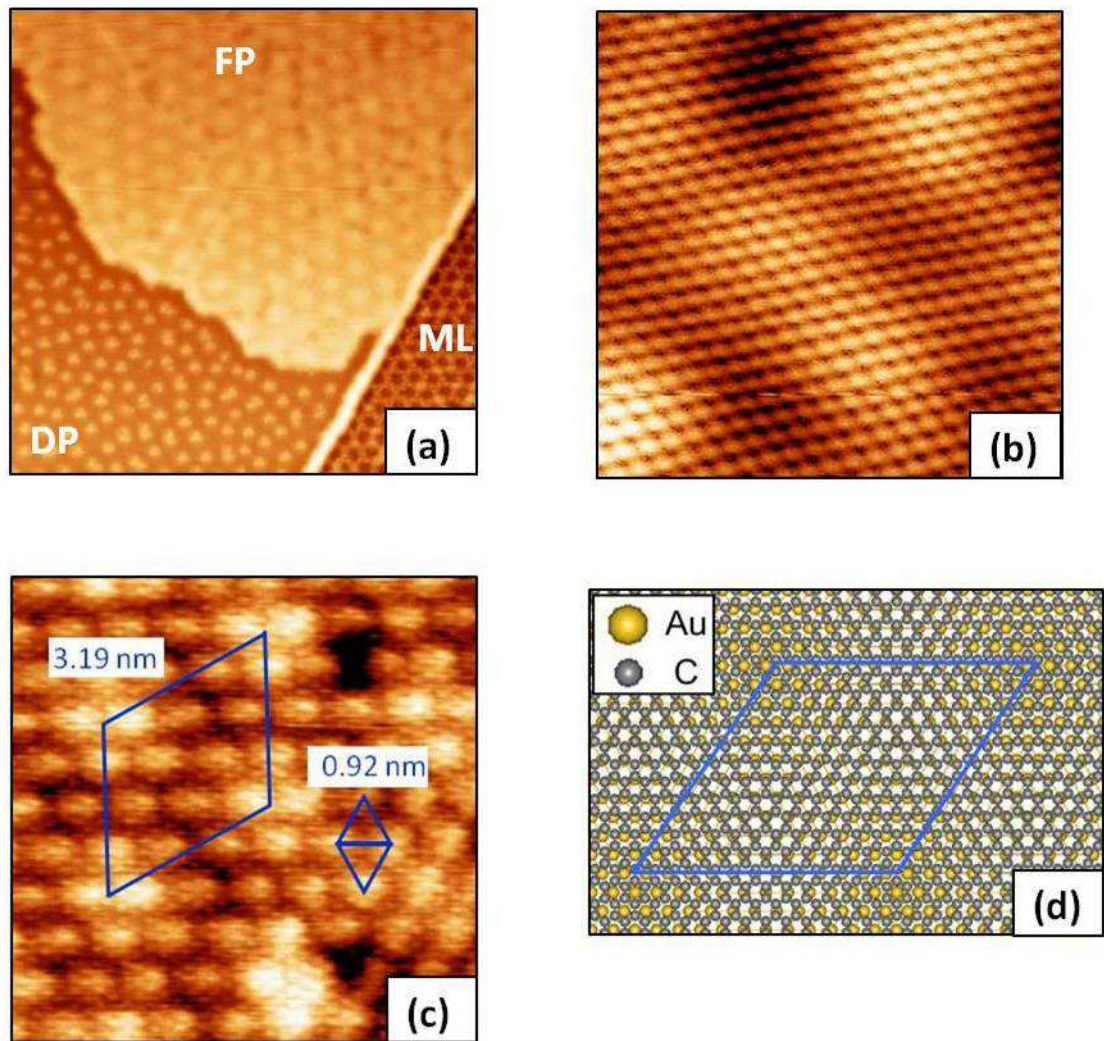


Figure.3.3: STM topographic images of film phase (FP). (a) (45nm×45nm,-1.5V), shows the Film Phase (FP) diluted Phase (DP) and Monolayer Graphene (ML). (b) (5nm×5nm,-5mV) shows the atomic resolution of film phase (FP) reveals only one per two carbon atoms as in the case of bilayer graphene at low bias (-5mV). (c) (8nm×8nm,-0.5V) shows FP at higher bias (-0.5V) display 13x13-G reconstruction (3.19nm) and a $2\sqrt{3}\times 2\sqrt{3}R30$ -Au reconstruction (0.92nm). (d) shows a theoretical model showing the Moire pattern obtained by the superposition of a monolayer of gold and a monolayer of graphene, resulting in a 13x13-G surface modulation as observed in (c) [83].

Chapter 3. Intercalation of gold on Epitaxial Graphene

3.4. Characterization of diluted phase (DP)

Figure 3.4. depicts the STM topographic images of intercalated gold clusters known as diluted phase. The DP consists of an irregular distribution of aggregates of clusters with an average distance of 2.2 ± 0.1 nm.

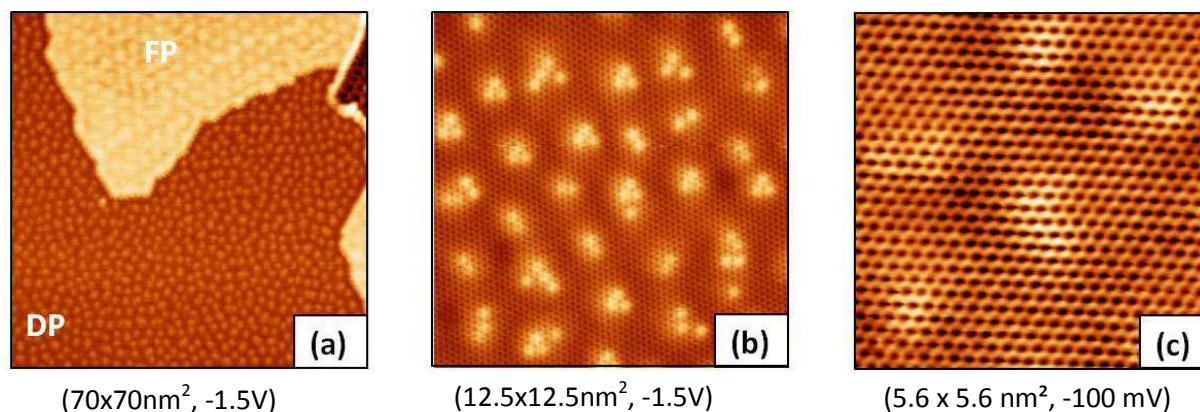


Figure.3.4: STM topographic images of diluted phase. (a) Intercalated clusters or (DP) and film phase (FP). (b) zoom of DP in (a), (c) zoom of DP at low bias (-100mV) reveals the 6 carbon atoms in honeycomb structure of graphene, confirmed gold clusters are intercalated below the ML graphene.

The intercalated gold clusters are evidenced by bright protrusions visible at high bias voltage as shown in Figure 3.4.a and enlarged in 3.4.b. The zoomed image at low bias voltage (-100meV) shows the graphene plane over the bright dots where the six carbon atoms of the honeycomb structure are equally visible (Figure 3.4.c). This confirms that the gold clusters are just under the top graphene monolayer. These clusters are less visible at low bias voltage and the honeycomb structure of graphene dominates the contrast. The measured height difference between pristine ML graphene and the DP is 0.8 ± 0.1 Å. This corresponds to a ML graphene and a bilayer graphene formed on two adjacent steps with the bilayer graphene formed on lower terrace [116]. This signifies that the space between the top ML graphene and the buffer layer does not allow the insertion of 3D gold islands. Therefore, it is reasonable to propose that the Au aggregates consist of small flat clusters or individual atoms. We have attributed these bright dots to aggregates of mostly 3 flat

Chapter 3. Intercalation of gold on Epitaxial Graphene

clusters triangle shaped with 1 or 3 Au atoms. Further details about the number of gold atoms within the clusters and the position of the intercalated gold atoms can be inferred in next section.

3.5. Position and number of intercalated Au atoms

The first interpretation of the features observed by STM and their attribution to flat triangular gold cluster was quite naïve [83] and needed further detailed studies with the help of STM calculated images. Several questions were still under debate. What is the nature of the intercalated gold, flat clusters of individual gold atoms? What is the real location of gold, under the buffer layer or between the graphene top layer and the buffer layer? Do we really have cluster atoms or simply individual atoms? This question is particularly important because beyond this, this demonstrates the possibility to have topological insulator proposed in a theoretical paper [117]. Which corrugation could be expected depending of the position and the number of gold atoms, cluster? To understand in more details about the position and number of Au atoms intercalated on graphene, a comparative study was performed between the experimental STM and the simulated STM images using DFT-LDA calculations.

The simulated STM images using DFT-LDA calculations were performed by our collaborators Tao Jiang and Marie-Laure Bocquet from ENS, Lyon. The calculations were carried out with Vienna Ab initio Simulation Package (VASP). They were also considered the local density approximation (LDA) to describe the exchange and correlation energy. Also utilized screened hybrid functional of Heyd, Scuseria and Ernzerhof (HSE) scheme to quantify the improvement of electronic structure of graphene. In order to get a good understanding to Si-face graphene on SiC interface and its influence to electronic structure of graphene, adopted a large commensurability i.e. 13×13 graphene on $6\sqrt{3} \times 6\sqrt{3}$ substrate (referred as to 6R3), instead of smaller model- the 2×2 graphene on $\sqrt{3} \times \sqrt{3}$ (referred as to R3) SiC substrate preferred by many previous ab initio studies of the same system which give 8% extra strain due to the mismatch of graphene and SiC lattice constants. The SiC substrate is modeled by two SiC bilayers, the top face being Si and the

Chapter 3. Intercalation of gold on Epitaxial Graphene

bottom being C saturated by hydrogen atoms, including 432 atoms. All structures were relaxed until the total forces are smaller than $0.02 \text{ eV}/\text{\AA}$. Another key parameter to compute an accurate band structure is the Brillouin Zone k-sampling in reciprocal space. A set different k-values further from Γ point along the Γ -K direction were taken into account. STM images at constant current were simulated by means of the Tersoff-Hamann theory. In order to correctly reproduce the exponential decay of wavefunctions in the vacuum region; above a given height approximately $2\text{-}3 \text{ \AA}$ from the outmost atoms of the sample, the analytical expression of the wave function for a flat potential in vacuum was considered.

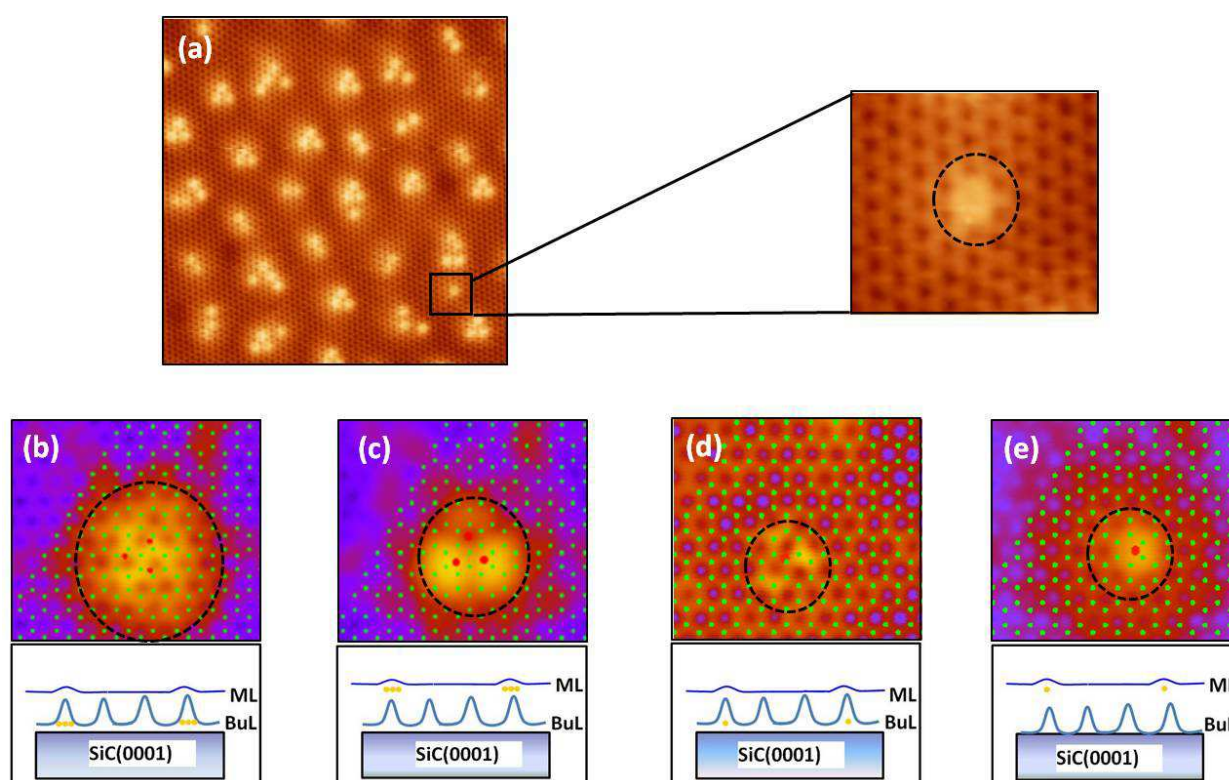


Figure.3.5: Experimental STM image ($12.5 \times 12.5 \text{ nm}^2$, -1.5 V) of gold clusters intercalated on epitaxial graphene in which one isolated cluster is zoomed ($2.7 \times 2.4 \text{ nm}^2$, -1.5 V) and shown in a black circle (a). The simulated STM images of 1 and 3 Au atoms between the ML and BuL and under the BuL and the corresponding schematic diagrams are shown below of the image (b-e). All the simulated STM images were obtained at -1.3 V and 100 nA .

Chapter 3. Intercalation of gold on Epitaxial Graphene

In Figure 3.5.a, we have found and focused on an individual object that constitutes the aggregates. These aggregates are made of one to four of these features. The individual feature shape is a triangle which affects the contrast of about 8 carbon atoms corresponding to a radius of 0.5nm. In b) to e) we compare the calculated images of the resulting feature on top graphene layer for a cluster made of three gold atoms (one) under the buffer b) and d) or between the graphene and the buffer layer c) and e) respectively. Among the all calculated images, the zoomed isolated cluster in the experimental STM image resembles as one Au atom between the graphene monolayer (ML) and buffer layer (BuL) as shown in (3.5.e). Moreover, the affected number of carbon atoms by the intercalated gold in the experimental STM image ≈ 8 , which is same as in the case of one Au atom between the ML and the BuL. The simulated size of 3 Au atoms between the ML and BuL and under the BuL is very large compared to the experimental image. The affected numbers of carbon atoms by 3 Au atoms ML and BuL and under the BuL are 53 and 89 respectively. And for 1Au atom under the BuL, the shape of simulated image is completely different from the experimental isolated cluster image. Hence, from the shape and size and the number of affected carbon atoms, we can reach a conclusion that the intercalated gold cluster is made by one Au atom and the intercalation occurs between the monolayer (ML) and buffer layer (BuL). We noticed that the calculated roughness induced by the intercalated gold atoms was always found much higher than experimentally observed. For example, in the case of one gold atom intercalated between the monolayer graphene ML and BuL, the calculated roughness was found about 1 Å while for the experiment 0.4 ± 0.04 Å was found.

However, the experimental STM image contains mostly aggregates of 1 to 4 clusters, which are separated by 3.3 ± 0.8 Å. This asks the question of the stability of individual gold atoms separated by such a distance. The stability of such aggregates is currently studied by calculation.

Chapter 3. Intercalation of gold on Epitaxial Graphene

3.6 Scanning Tunneling Spectroscopy (STS) measurements on ML, DP and FP

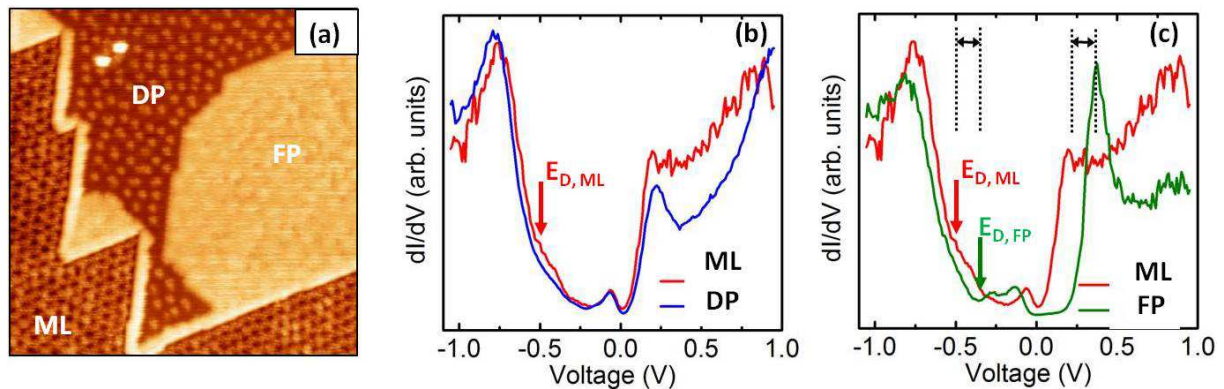


Figure.3.6: (a) STM topographic image of gold intercalated EG ($50 \times 50 \text{ nm}^2$, -1 V) and the corresponding STS measurements on the three region labeled ML (undoped monolayer graphene), DP (diluted phase) (b) and FP (film phase) (c) [83].

In order to see which intercalation mode is able to dope graphene, scanning tunneling spectroscopy measurements were performed and compared with that of pristine graphene. The spectroscopic data of these individual regions were obtained by spatially averaging the curves recorded at several points in the corresponding regions. It was found that there was no difference between the STS data of Monolayer graphene (ML) and diluted phase (DP) as shown in Figure 3.6b. This clearly demonstrated that no doping of graphene on the diluted phase.

The dI/dV curve of FP depicts the (Figure 3.6c) marked shift of the maxima with an increase in the gap around the Fermi level. The position of the Dirac point was shifted by 200 meV towards the Fermi energy indicating a p-type doping effect. This also corresponds to the shift of the large peak at $\approx +450 \text{ meV}$. Two structures appeared with a soft gap around -250 meV . This could possibly be attributed to the super periodicity $2\sqrt{3} \times 2\sqrt{3} R_{30-Au}$. The spectroscopic effect associated with the surface moiré pattern is supportive of the idea that this region consists of an intercalation of gold monolayer with ML. As the n doping of the graphene layer is due to a transfer of electron from the substrate, this result indicates that gold atoms screen this transfer of charge, in other

Chapter 3. Intercalation of gold on Epitaxial Graphene

words modify the work function of the electron in the substrate/G interface. When the intercalation is discontinuous (as in the case of diluted phase) this “screening” is not enough efficient, while in the case of the continuous film the screening is enough efficient to hinder this transfer of charge and a p-type doping is observed. However, further theoretical studies are needed to explain the behavior of the STS curves. A part of these results were published in [83].

To conclude that the p-type doping occurs only for a continuous gold layer but do not happens in the case of diluted phase.

3.7. Free standing nature of intercalated gold clusters

To understand the ‘free standing nature’ of intercalated atoms several methods were employed such as Differential charge density plot, Projected Density of States (PDOS) and X-ray photoelectron spectroscopy (XPS).

3.7.1. Differential charge density

The bonding property of the intercalated clusters with graphene was verified using differential charge density plot. It was observed that there were no significant difference in the charge density of gold and carbon on graphene and buffer layer. The charge redistribution indicates that the bonding between gold and carbon is mainly due to the dipole-dipole interactions, hence, there was no obvious charge depletion or increment in both graphene and buffer layer. Therefore, one can conclude that these gold clusters are freestanding between the graphene ML and the buffer layer.

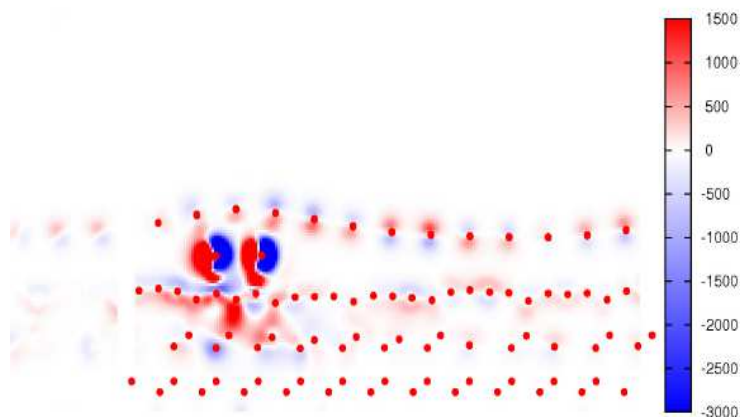


Figure.3.7: Shows differential charge density of graphene with intercalated gold clusters. The red dots are the atoms on top of or close to the section plain and the three red dotted lines from top to bottom are graphene layer, buffer layer and SiC. The intercalated gold atoms (two mixed red and blue dots) are located between the graphene and buffer layer. Red color in color scale indicates accumulation of electrons and blue color indicates depletion of electrons.

3.7.2. Projected Density of States (PDOS)

The free standing nature of gold clusters was further supported by the Projected Density of States (PDOS) obtained from Density Functional Theory-Local density Approximations (DFT-LDA) calculations. Figure 3.8 shows the PDOS of ML and BuL without gold, ML and BuL when 3 gold atoms in between, and ML and BuL when 3 gold atoms below the BuL. When we compare the PDOS of pristine ML graphene with 3 gold atoms below the BuL or between the ML and BuL it was found that the PDOS of graphene ML with intercalated Au atoms lying exactly on the same position of graphene without Au, which indicates that there was no change in the estimation of PDOS with and without Au intercalation. In addition, the same results were obtained with respect to the position of the gold atoms. Hence, in the framework of this theoretical approach the existence of gold atoms does not affect the electronic structure of graphene.

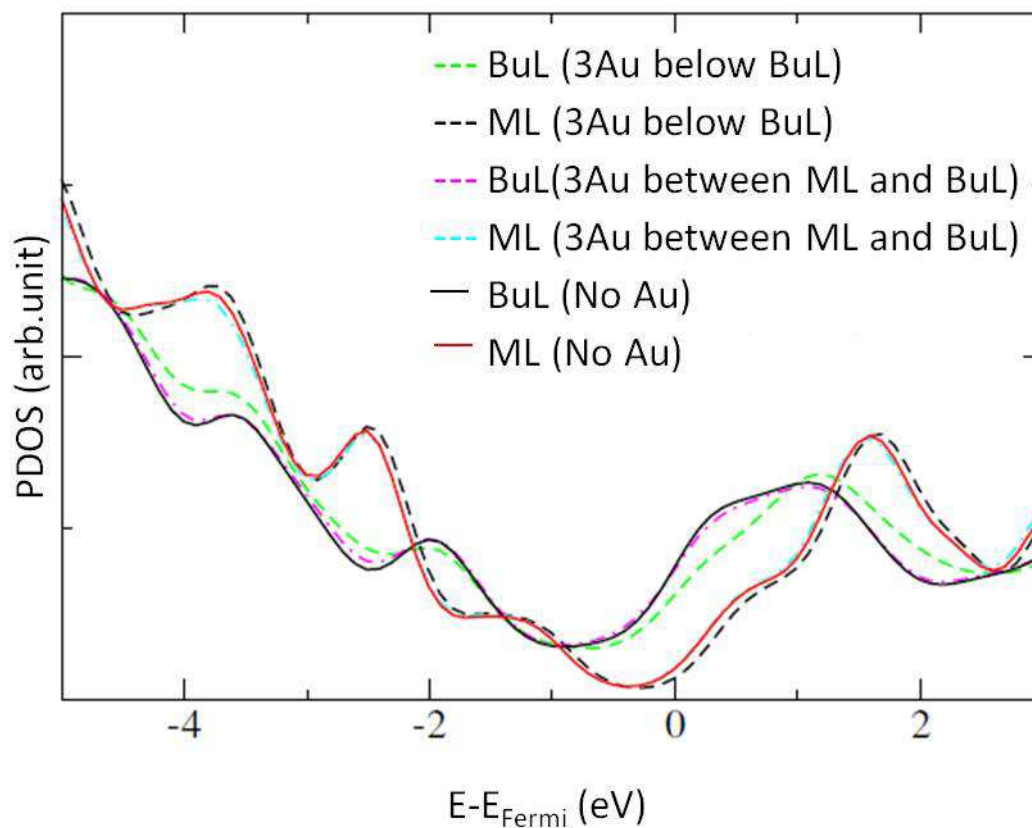


Figure.3.8: Projected density of states (PDOS) of buffer layer (BuL) and monolayer graphene (ML) for graphene with and without gold intercalation. The position of 3 gold atoms (below the BuL or between BuL and ML) are considered.

3.7.3. X-ray photoelectron spectroscopy (XPS)

A detailed analysis of the chemical states of intercalated gold with cluster phase (DP) and large areas of film phase (FP) was determined by X-ray photoelectron spectroscopy (XPS). The principle of this technique can be found in chapter 2.

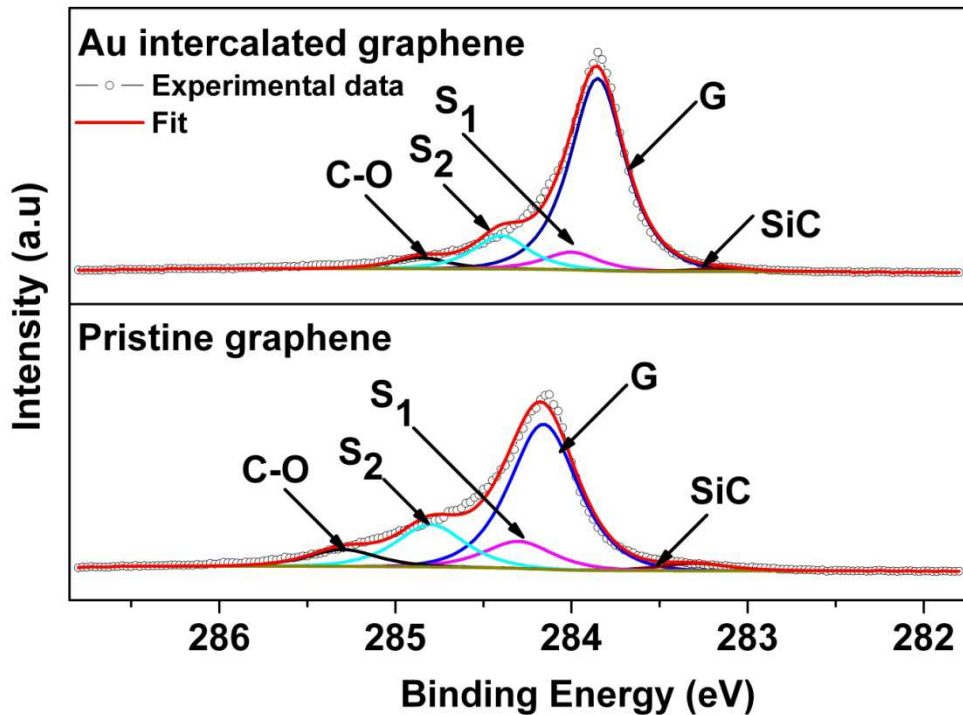


Figure.3.9: C1s spectra of pristine graphene (bottom) and gold intercalated graphene (top) along with their deconvolution into bulk SiC (SiC), graphene (G), buffer layer (S1 and S2) components and carbon-oxygen (C-O) component. The fitting parameters are summarized in the Table 3.1.

Figure 3.9 shows the C1s XPS spectra of pristine graphene (bottom) and gold intercalated graphene (top). The C1s spectrum of the pristine monolayer graphene shows five components, one at 283.3 eV related to SiC bulk component, graphene component at 284.16 eV, buffer layer (BuL) components S1 (284.3 eV) and S2 (284.8 eV) and a component at 285.3 eV is due to the oxygen-carbon groups, since the sample was exposed to air. As illustrated in Figure 3.10, the lower energy component S1 is due to the covalent bonds between the BuL and SiC surface, while S2 is related to the sp^2 bonded carbon atoms within the buffer layer. The two components have an area ratio of S1:S2 slightly below 1:2.

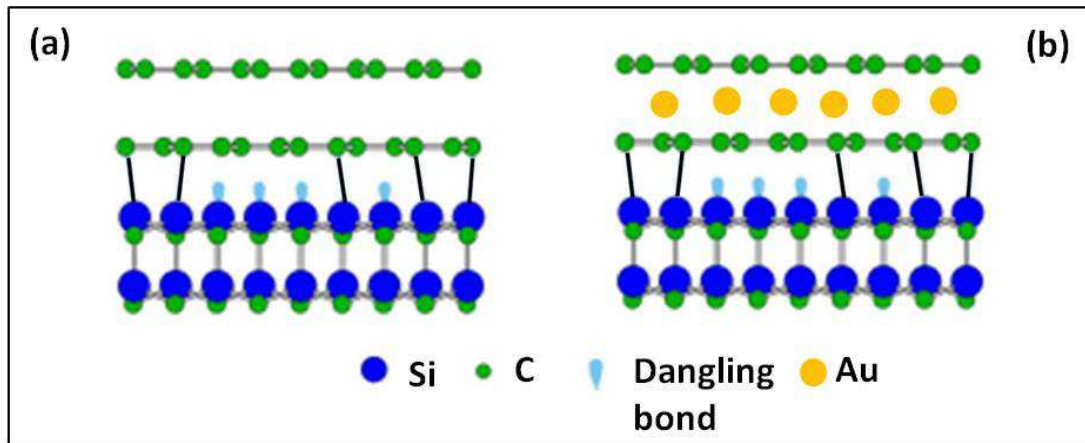


Figure.3.10: Structural model of (a) pristine graphene [118] and (b) gold intercalated graphene.

The interpretation of these components was deduced in accordance with [53, 118]. The origin of the C-O peak at higher binding energy may arise from the oxygen contamination of our sample [119]. The effect of partial oxidation was observed before from ARPES measurements where the Dirac Energy of pristine graphene, $E_D \approx -0.29\text{eV}$ was increased from $E_D \approx -0.45\text{eV}$ obtained from STS measurements, which were performed in-situ.

Figure 3.9 (top) shows the C1s spectrum of graphene with intercalated gold clusters. No additional components are required to fit the spectra when compared to pristine graphene. The intensity of the graphene component is increased by 20%, but the whole shape of the C1s spectra is unchanged and both components S1 and S2 are still present. Supposing that the gold is intercalated under the BuL and leads to decouple the BuL, then we should observe a suppression of both the S1 and S2 components. In the case of hydrogen intercalation, Riedl *et al.* [66] observed the complete absence of buffer layer components (S1 and S2) in their C1s core level spectra and concluded and proved that the buffer layer is turned into a quasi-free-standing graphene monolayer. A similar result was obtained in the case of oxygen intercalation on EG on SiC (0001) [120]. In our study, the buffer layer components are present even after the gold intercalation confirming that the gold atoms do not break the bond between carbon atoms from buffer layer and silicon

Chapter 3. Intercalation of gold on Epitaxial Graphene

atoms from SiC substrate. Thus BuL remains intact. Furthermore, intensity of graphene component is increased after the Au intercalation. This indicates that the ML graphene is decoupled from the SiC substrate. Therefore, these results point out that the Au atoms do not make any chemical bond with carbon atoms (no additional components) and the BuL is preserved (S_1 and S_2 are unchanged). On the basis of this C1s spectra and the fact that the STM images clearly show the graphene layer on top of the intercalated gold, we conclude that gold is intercalated between the BuL and the top graphene layer.

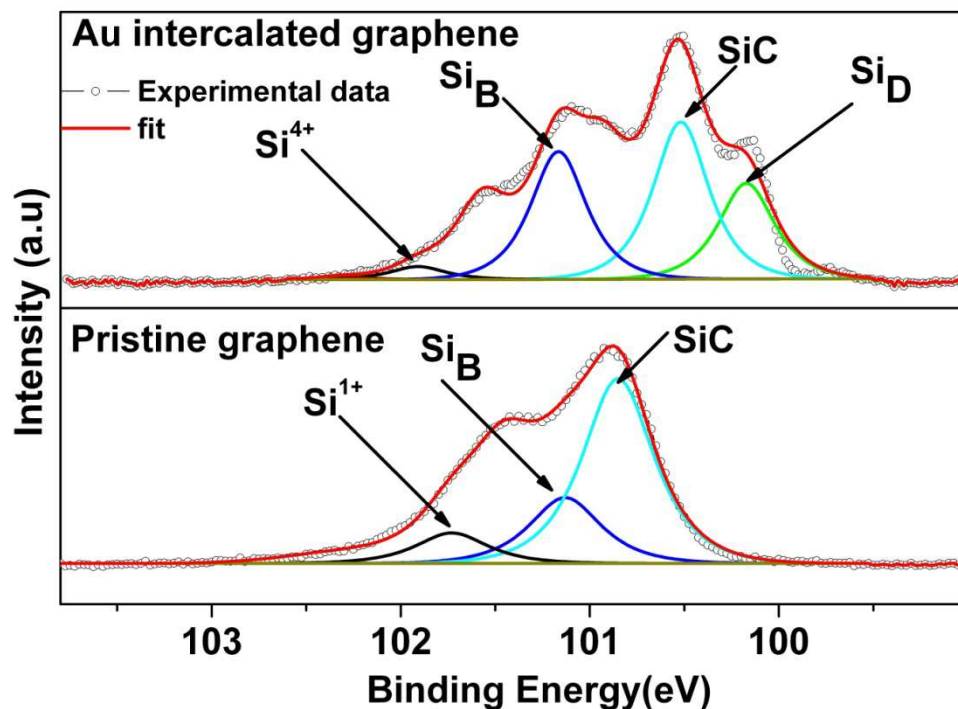


Figure 3.11: Si2p spectra of pristine graphene (bottom) and gold intercalated graphene (top) along with their deconvolution; bulk SiC (Si_C), buffer layer (Si_B), oxide components (Si^{1+} , Si^{4+}) and an additional surface defect component (Si_D) in Au intercalated graphene. For the sake of clarity, only $Si2p_{3/2}$ components are shown. The fitting parameters are summarized in the Table 3.1.

Figure 3.11 shows the Si2p spectra of pristine graphene (bottom) and gold intercalated graphene (top). Due to spin orbit splitting, the pure Si2p peak split into two components, $Si2p_{1/2}$ and $Si2p_{3/2}$ with an energy separation of 0.6eV and the area ratio of 1:2. For clarity, only $Si2p_{3/2}$ components are shown in the Figure 3.11. The Si2p spectrum of pristine graphene consists of three components. The dominated peak at 100.85eV is

Chapter 3. Intercalation of gold on Epitaxial Graphene

attributed to SiC bulk, one at 101.13eV related to BuL component (Si_B) and an oxide component (Si^{1+}) at 101.73eV due to the oxygen contamination of our samples. The BuL component (Si_B) is related to Si atoms from the SiC substrate that bound to the carbon atoms of the buffer layer [53,118]. As they are still in sp^3 -hybridization, only a small chemical shift with respect to the bulk SiC peak can be observed.

The Si2p spectrum of gold intercalated graphene (Figure 3.11 (top)) shows an additional component at lower binding energy from bulk SiC compared to pristine graphene. The peak at lower binding energy could be attributed to Au-Si2p bonds [121-122]. However as shown by Emtsev *et.al.* [53], this component has been observed on pristine graphene (without any deposition) and attributed to surface defects. The origin of this component arises from the Si atoms on the surface of graphene/BuL or incorporated into graphene's lattice as interstitial defects. This peak is absent for high-quality samples with large-scale homogeneity. Park *et.al.* [123] attributed to Si atoms that are trapped in the interface layer during graphitization. As we have seen from C1s spectra that the buffer remains intact and is not decoupled from the substrate, therefore, in our case this lower binding energy component can be directly related to surface defects which may arise during the preparation of graphene samples with gold (during gold deposition and further annealing) that slightly degrade the quality of our samples. Consequently, from Si2p spectrum of gold intercalated graphene, one can conclude that there are no SiC-Au or Si-Au bonds.

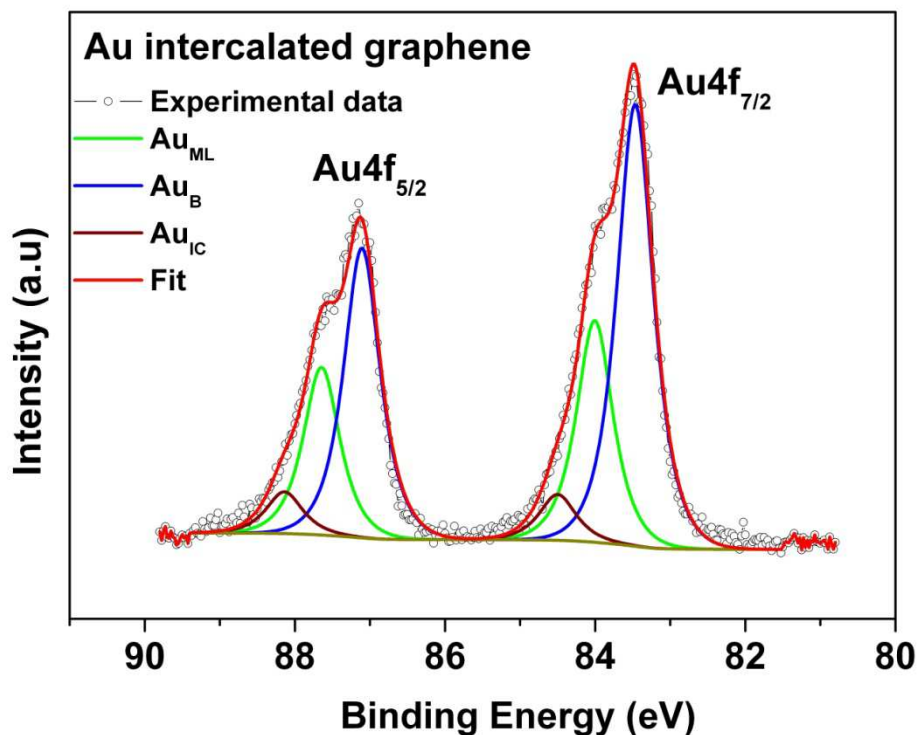


Figure 3.12: Au4f core level spectra of gold intercalated graphene together with their deconvolution into bulk gold (Au_B), monolayer of gold (Au_{ML}) and gold intercalated clusters (Au_{IC}). The fitting parameters are summarized in the Table 3.1.

Further to verify the bonding nature of gold with carbon and silicon atoms, Au4f spectrum of gold intercalated graphene was recorded. Figure 3.12 shows the Au4f spectrum of gold intercalated graphene. Due to spin-orbit splitting, the pure Au4f spectra split into two components, $Au4f_{5/2}$ and $Au4f_{7/2}$ with an energy separation of 3.65eV and area ratio of 3:4. The Au4f spectrum of gold intercalated graphene is decomposed into three components. The dominant peak at lower binding is attributed to the Bulk gold (Au_B). The other two peaks at 84eV and 84.5eV are assigned to gold monolayer (Au_{ML}) and small clusters (Au_{IC}) or individual atoms respectively. The Bulk gold (Au_B) component originates from the 3D-islands of gold on the sample surface which were observed in the STM images even after several cycles of annealing. The assignment of other two peaks is related to a shift towards higher binding side with decreasing the size of gold clusters [124-126]. Kitsudo *et.al.* studied the so called “final state effect”, the effect of a positive charge left on a small metal particle immediately after photoemission from gold nano particles grown on oxides and HOPG supports. It is observed that binding energy shift changes dramatically at a critical number of

Chapter 3. Intercalation of gold on Epitaxial Graphene

atoms per particle (n_A) value ~ 70 atoms, where the metal to non-metal transition takes place. In the non-metal region, E_B shift increases steeply almost exponentially with decreasing n_A , gradually decreases with increasing n_A in the metallic region (Figure 3.13). They observed Au4f spectra for (0.05, 0.2, 0.6 ML) are decomposed into two components with higher and lower E_B shift. They proved that the higher E_B component is attributed to small clusters and lower E_B component is attributed to large clusters [124].

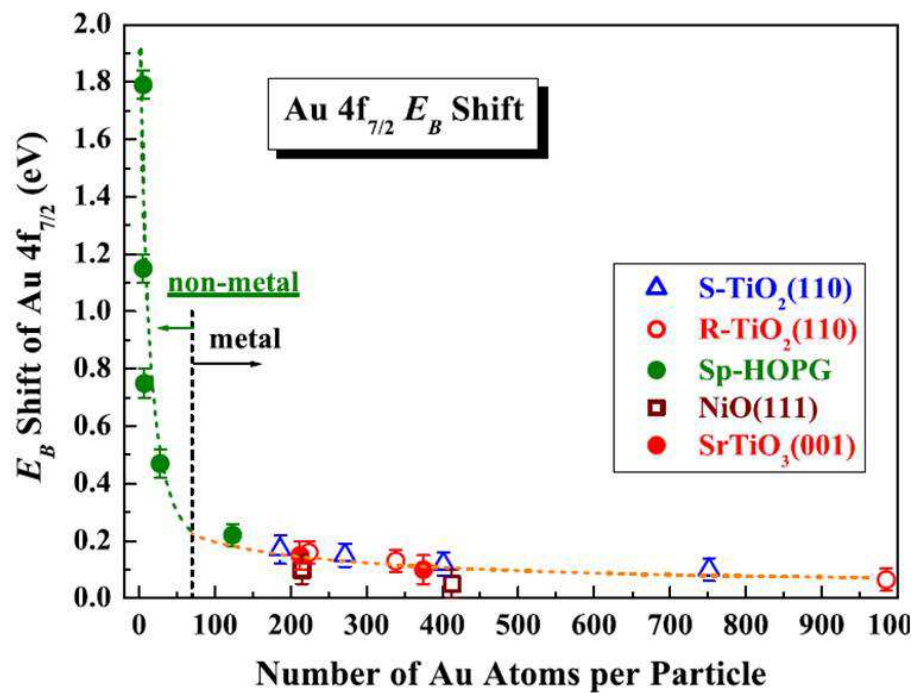


Figure.3.13: Binding energy shift of Au 4f_{7/2} for R-and S-TiO₂(110),SrTiO₃(001), NiO(111) and Sp-HOPG supports as a function of number of Au atoms per particle. Dotted line indicates a critical number (70) of Au atoms per particle for metal-non-metal transition. Adapted from Kitsudo *et al.* [124].

Boyen *et.al.* also shown that Au4f shift towards high binding energy side by decreasing the size of gold clusters [125]. The reduce size of gold cluster until the ultimate limit of individual atoms in the case of the diluted phase will then lead to an increase of the binding energy of the Au4f line. This is in accordance with our results, however a shift of 1eV is observed in our case while up to 1.6 eV would be expected in the case of individual atoms. How the gold

Chapter 3. Intercalation of gold on Epitaxial Graphene

atoms, even separated by 5 Å could still interact, what kind of relaxation effect would happen in the photoemission process for intercalated gold (charging effect,...) these are open questions.

To conclude, the “free standing” nature intercalated gold clusters was revealed by XPS. The C1s XPS spectra of pristine graphene and gold intercalated were accurately fitted with the same number of components, the intact nature of BuL component pointed out that Au atoms do not make any bond with carbon from BuL or from graphene. Further analysis of Au4f core level spectra, also reveals an absence of Au-C bonds which are expected at 1.5eV towards higher binding energy with respect to Bulk Au binding energy position [127]. Moreover, the Si2p and Au4f core level spectra of gold intercalated graphene ensure the absence of Au-Si bonds. However the reason why and how the intercalation of gold leads to increase the SiD component is still an open question. This is probably due to the intercalation process and this component could be associated to the formation of rims during intercalation process.

Chapter 3. Intercalation of gold on Epitaxial Graphene

Pristine graphene					
Core level	Component s	E_B (eV)	FWHM	Peak area (%)	Assignment
C1s	SiC	283.3	0.457	3.1	SiC bulk
	G	284.16	0.457	60.75	Graphene
	S1	284.3	0.457	11.33	Sp ³ bonded C
	S2	284.8	0.457	17.72	Sp ² bonded C
	C-O	285.3	0.457	7.1	O- contamination
Si2p _{3/2}	SiC	100.85	0.442	45.4	SiC bulk
	Si _B	101.13	0.442	16.19	Si bonded to buffer layer
	Si ¹⁺	101.72	0.442	3.5	Oxide peak
Gold intercalated graphene					
C1s	SiC	283.14	0.368	1.35	SiC bulk
	G	283.85	0.368	74.56	Graphene
	S1	284	0.368	6.84	Sp ³ bonded C
	S2	284.4	0.368	12.93	Sp ² bonded C
	C-O	284.86	0.368	4.32	O- contamination
Si2p _{3/2}	Si _D	99.48	0.510	15.28	Surface defects
	SiC	100	0.510	24.93	SiC bulk
	Si _B	100.95	0.510	20.38	Si bonded to buffer layer
	Si ⁴⁺	102.05	0.510	2.06	Oxide peak
Au4f _{7/2}	Au _B	83.47	0.570	36.55	Au bulk
	Au _{ML}	84.01	0.570	18.34	Au ML or Au clusters (big)
	Au _{IC}	84.5	0.570	3.8	Au clusters (small)

Table.3.1. The fitting parameters for the C1s, Si2p_{3/2} and Au4f_{7/2} of the pristine graphene and gold intercalated graphene. All spectra were taken at photon energy of 350eV. E_B is the binding energy referenced to the Fermi level. Curve fitting were carried out using casa XPS software, fitted with standard Voigt function including a Shirley background.

Chapter 3. Intercalation of gold on Epitaxial Graphene

3.8. Standing wave patterns on diluted phase (DP)

One of the first goals of my work was to explore the band structure of graphene particularly around the Van Hove singularities. A modification of the band structure around M points was first suggested by the observation of standing waves pattern on the graphene layer in the presence of intercalated dispersed gold atoms. For these reasons and in order to compare directly these measurements with ARPES measurements in this thesis I will recall here FT-STs experiments and its interpretations [128].

The diluted phase (DP) for positive bias voltage at +0.8, +0.9 and +1.0V are shown in Figure 3.14. Here the empty states are probed, from the topographic images (3.14.a-c) the intercalated gold clusters can be seen as large protrusions and from the corresponding dI/dV maps (d to f) marked features attributed to standing wave patterns can be observed. These standing wave patterns were only observed in the presence of the intercalated gold clusters. It seems that the aggregates create an excess of electrons and appear as dark regions for the empty states energies in the dI/dV maps (d to f). The size of the dark region was reduced with an increase in bias energy and finally a complete strong and contrasted standing-wave pattern was observed in (f). Figures (g) and (h) shows the zoomed topographic image and dI/dV map reveal that the standing waves manifest as bright protrusions with lattice vectors which correspond to a $p(2 \times 2)$ in conjunction with stripe line with the same periodicity (in the same directions as the unit cell vectors as schematized in (i)).

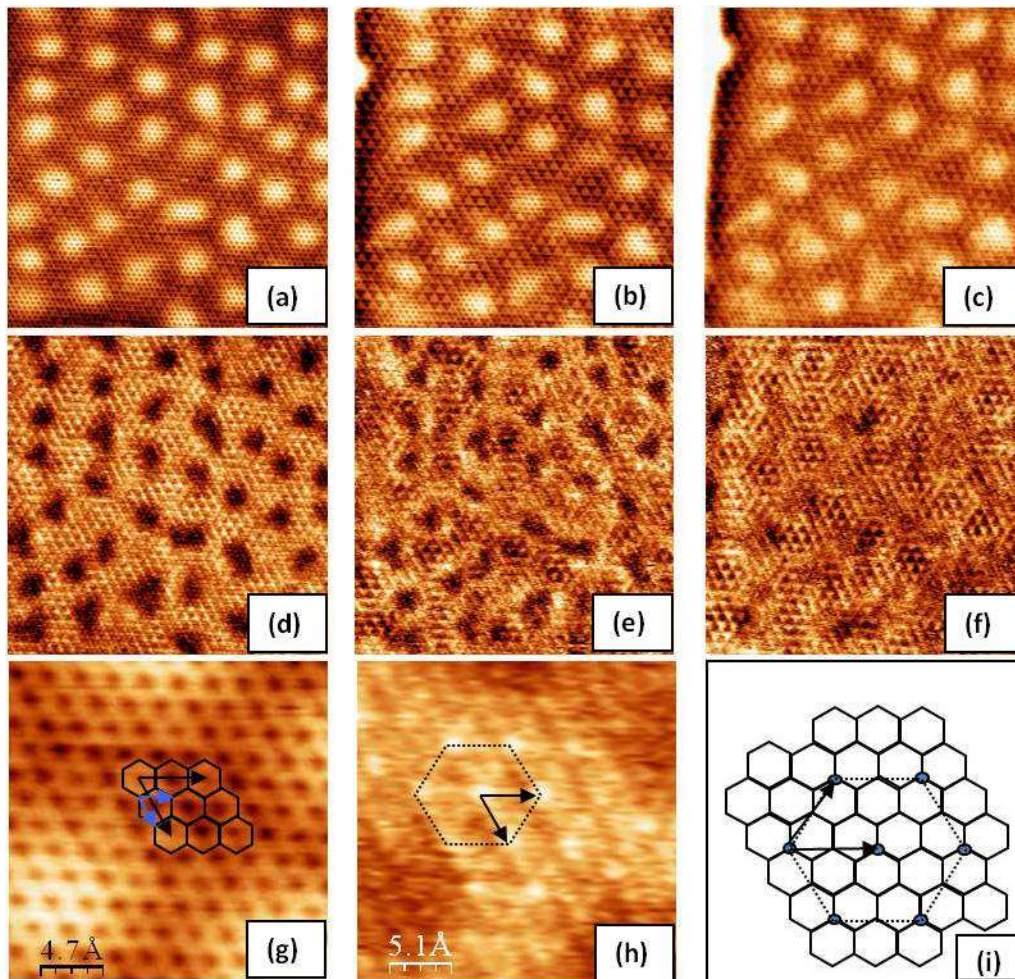


Figure.3.14: STM topographic (a-c) and dI/dV maps (d-f) of DP for bias voltage from +0.8 to +1V (empty states) which develops a standing wave pattern. (a, d) ($14 \times 14 \text{ nm}^2$) and (b,c,e,f,) ($12.5 \times 12.5 \text{ nm}^2$). (g) and (h) ($2.5 \times 3.2 \text{ nm}^2$) shows a zoomed area of a region of resonators which shows that standing waves manifest as bright protrusions with a p(2×2) reconstruction, as schematized in (i). Images are taken at +0.8V, 1nA for topographic (g) and dI/dV map (h) [128].

Sprunger *et al.* was first to show that, the FT of standing-wave patterns obtained at the Fermi level, gives a direct representation of the Fermi surface [129]. It provides a direct representation of wavelengths of standing waves in the local density of states and also details of the possible scattering process. In this elastic process, wave functions are perturbed (stationary perturbation of Hamiltonian) which results to mix all unperturbed Eigenstates. The Fourier transform image represents how many time a scattering event corresponding to a diffusion vector with a given module and direction is observed.

Chapter 3. Intercalation of gold on Epitaxial Graphene

It has been demonstrated that the power spectrum of the 2D FT-STS is in a first approximation the Joint Density of states (JDOS) at a given energy which can be formally calculated by the 2D self-correlation function of the CEC [130]. Since the pioneer results of Sprunger, this approach has been used not only for the Fermi surface at the Fermi level, but also, using dI/dV map images for the determination of the Fermi surface at different energies. JDOS has been successfully used on superconductors [131] allowing the evidence of Bogoliubov-de Gennes pairs in the opening of superconducting gap. Simon *et al.* [132] demonstrated that not only the position of the features in the FT-STS but also their shape is able to provide valuable information of the Fermi surface at different energies allowing a complete determination of the energy dispersion of a 2D semimetal by the interpretation of the features shapes and their modifications with energy. In the same time these experiments demonstrated that the Fermi liquid approximation can be valid not only at the Fermi level but at different energy and the band structures are robust enough in the scattering process (Eigen states nature are preserved). Few years later, on EG this approach was used to measure the group velocity of the QP's [133] and to provide a direct evidence of the chiral property of electrons in ML graphene [134] or the virtual hopping process between two successive plane in few layer graphene in the scattering process around point defects [135].

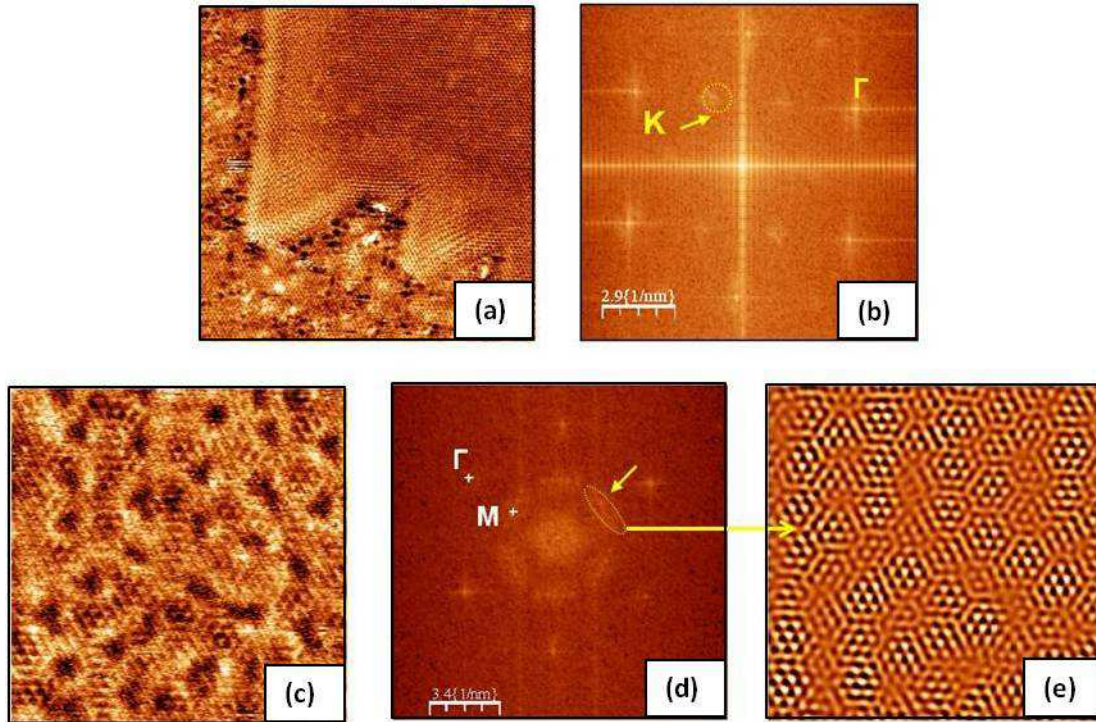


Figure.3.15: (a) shows the dI/dV map of DP (b) shows the 2D Fourier Transform (power spectrum) of dI/dV map of DP(a) at -0.7V ($19 \times 19 \text{nm}^2$). (c) shows the dI/dV map at +0.9V ($13 \times 13 \text{nm}^2$) and (d) shows the corresponding 2D Fourier Transform (power spectrum) of (c). (e) shows the FFT filtering of the dI/dV image taking only the elliptical feature around M-point has indicated on FT-STIS image at +0.9V (d). This gives a filtered dI/dV image where the observed network of resonators is strongly enhanced [128].

With this approach we will interpret the evolution of the FT of dI/dV images as a function of bias voltage. Figure 3.15.a depicts dI/dV map of DP at -0.7V where faint features around the K-points appear at its 2D FT as shown in Figure 3.15.b. These features are due to defect which creates standing waves and correspond to the well known $\sqrt{3} \times \sqrt{3}$ reconstruction and usually observed on graphite surface around point defects. Consequently, On the other hand, for the energy of +0.9V, the standing-wave pattern was observed as shown in Figure 3.15.c. The corresponding stronger feature appears around M point in the 2D FT image as indicated in Figure 3.15.d (shown with yellow color ellipse). Figure 3.15.d. illustrates the FFT filtering of the elliptical feature around the M-points (indicated by the yellow arrow on (c) at +0.9V. Figure 3.15.e gives a filtered dI/dV image

Chapter 3. Intercalation of gold on Epitaxial Graphene

where the observed network of resonators is strongly enhanced. Therefore, the observed features around the M points are strongly related to the standing wave patterns.

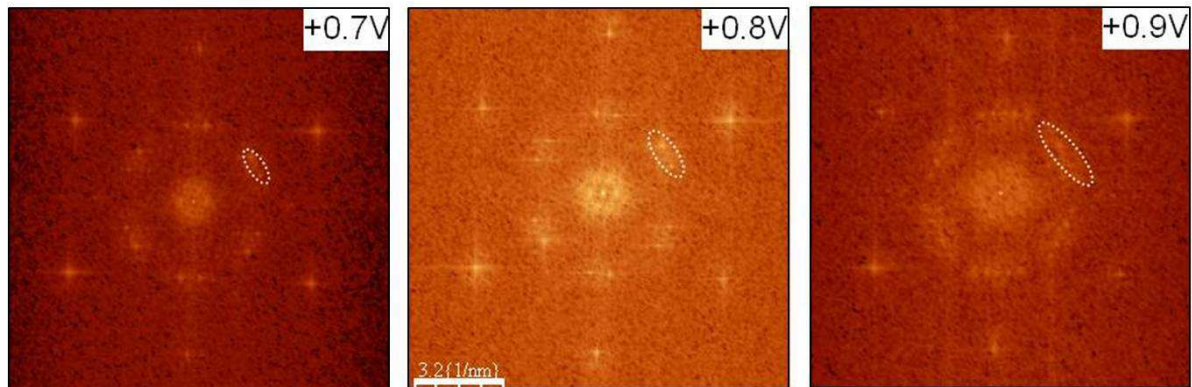


Figure.3.16: 2D Fourier Transform (power spectrum) of the dI/dV map image at the energy indicated on the figures. The dotted ellipses are represented by the strong features around M-points.

The size of the ellipse increases with the bias voltage as shown in Figure 3.16. The features around the M points in FT-STs become more and more contrasted and elliptical with the long axis of the ellipse along the direction M-K- Γ and further develop into distinct bright spots with increasing number (two at +0.7, +0.8V and four at +0.9V). The origin of these features has been associated with the idea of localization of the density of states around M points due to band crossover between two consecutive K and K' contours. This has been further verified by Joint Density of States (JDOS).

3.8.1. Joint Density of States (JDOS)

The gold clusters acting as defects that perturb the graphene quasiparticles. The constant energy contours have been calculated using the band structure resulting from a tight-binding model in which only the first nearest neighbor (1st order NN TB) hopping has been considered.

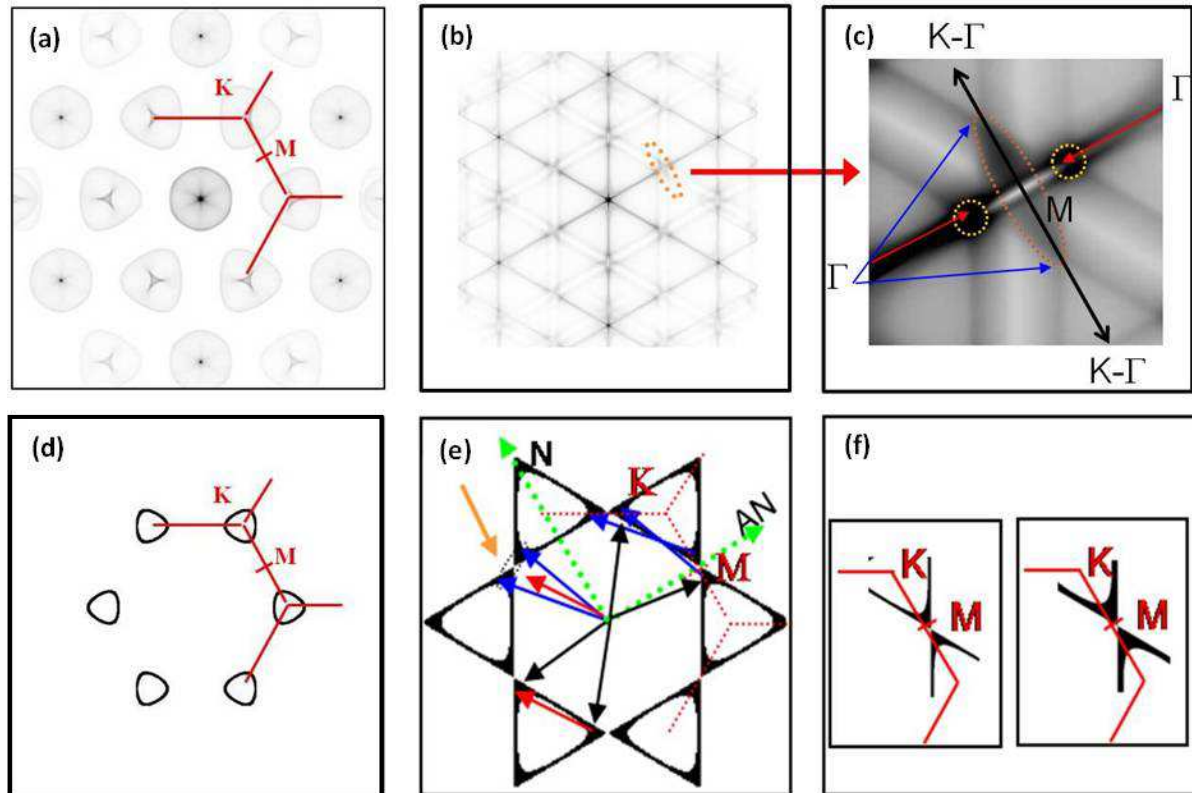


Figure.3.17: (a) and (b) show theoretical FT of the local density of states (dI/dV map) at energies for which the constant energy contours (CECs) are shown in (d) and (e) respectively. A zoom of the calculated features around M-point is given in (c). The blue and red arrows correspond to the momentum vectors associated to the black vectors in (e). In (c), these vectors are shown in the zoomed features around M-points: the elliptical feature by blue arrows and the two structures in perpendicular direction by red arrows around M point in the calculated JDOS. Blue arrows describe the ellipse correspond to intervalley scattering between two first nearest neighbor contours. Red arrows correspond to the intravalley scattering process shown in (e). (f) gives the proposed CEC evolution with increasing energy in the vicinity of the Van Hove singularity explaining the increase of the elliptic size found around M in (b) and (c). The size of the ellipse increases with the area of the density of states in the vertex of the triangle-shaped CEC contours [128].

The calculated JDOS image, which corresponds to the constant energy contour (CEC) given in 3.17.d below the crossover energy are given in Figure 3.17.a. At these energies the contours are localized around the K-points. JDOS shows the features around the K-points as identical to the one observed in Figure 3.15.a at -0.7V. Figure 3.17.b shows the calculated JDOS image which corresponds to the CEC of a graphene monolayer

Chapter 3. Intercalation of gold on Epitaxial Graphene

represented in (e) at the energy which corresponds to the band crossover, when K contours touch each other as schematized in f. This energy corresponds to the so-called Van Hove singularities (VHs). In (c) a zoom of the calculated JDOS around M-points displays two features. An elliptically shaped broad feature with long axis along M-K- Γ direction and two contrasted points in the perpendicular direction i.e. along the Γ -M- Γ direction (red arrows). As shown by the blue arrows the elliptical feature can be associated with the momentum which joins two equivalent points of two consecutive CECs around the K-points (called intervalley scattering). The feature along the Γ -M- Γ direction (red arrows) can be associated with the momentum which joins two corners of the same triangle-shaped K contour (called intravalley scattering) as shown in (e). However, the experimental FT-STs only shows the elliptical feature observed around M points due to the intervalley scattering, the features due to intravalley scattering predicted by the theory were absent.

In the JDOS approach, the elliptical features at the M-points appear in the spectra only if the CECs touch each other [136]. For normally dispersing graphene, when the energy is decreased below the Van Hove energy, the neighboring triangular CECs centered at the K-points no longer intersect, and the ellipses at the M-points are not observed as soon as we decrease the energy below the Van Hove energy. In the second scenario, the Van Hove singularity is extended to flat band, for which the momentum nesting at the Van Hove energy. In this situation, an increase in energy yields an increasing of the area of the flat band in the vertex of the triangular CECs contributing to the DOS. It can be clearly seen that the size of the elliptical feature in the JDOS depends on the size of the black area in the vertex of the triangular CEC [89]. This implies that the elliptical feature can be a finger print of the extension of the Van Hove singularity. In the work of Rotenberg [89], where the link between doped graphene and superconductivity was strongly supported, the ARPES measurements show that as soon as the vicinity of the Van Hove singularity is reached, the vertices of two consecutive triangular CEC contours begin to touch, and the density of states in the vertices was being filled by the doping. The

Chapter 3. Intercalation of gold on Epitaxial Graphene

situation appears quite similar to the one depicted in 3.17.f, which corresponds to a non-conventional dispersion. However, here the situation is for a non-highly-doped graphene.

Therefore, to conclude, we have seen that the intercalated clusters create strong standing wave patterns on monolayer graphene for bias voltage corresponding to the unoccupied states ranging from +0.7 to +1eV. These structures are attributed to the screening effect. The gold clusters screen the transfer of charge from SiC (0001) substrate to epitaxial monolayer graphene. This creates a charge inhomogeneity on graphene plane and scatters the quasiparticles of monolayer graphene thus creating a standing wave patterns. The 2D-FT of the dI/dV map images with standing wave patterns showed elliptical features around the M which have been attributed to the finger print of large extension of VFs. As these results were obtained on empty states, supposing that the symmetry of the band structure of graphene is preserved, we have explored the filled states with Angle-resolved photoemission spectroscopy (ARPES) measurements.

3.9. ARPES measurements on Pristine and Gold intercalated graphene

Angle-resolved photoemission spectroscopy (ARPES) measurements on pristine graphene and gold intercalated graphene (DP) were carried out at the CASSIOPEE beamline at the SOLEIL synchrotron radiation source using a Scienta R4000 electron spectrometer. The spectra were recorded at photon energy of 60eV with overall energy resolution of around 30meV at 10K. All the samples were prepared in a separated UHV system and then characterized by STM. They were then transported in air prior to UHV system of synchrotron radiation source. A soft degassing process at 500K for several minutes was performed before measurements.

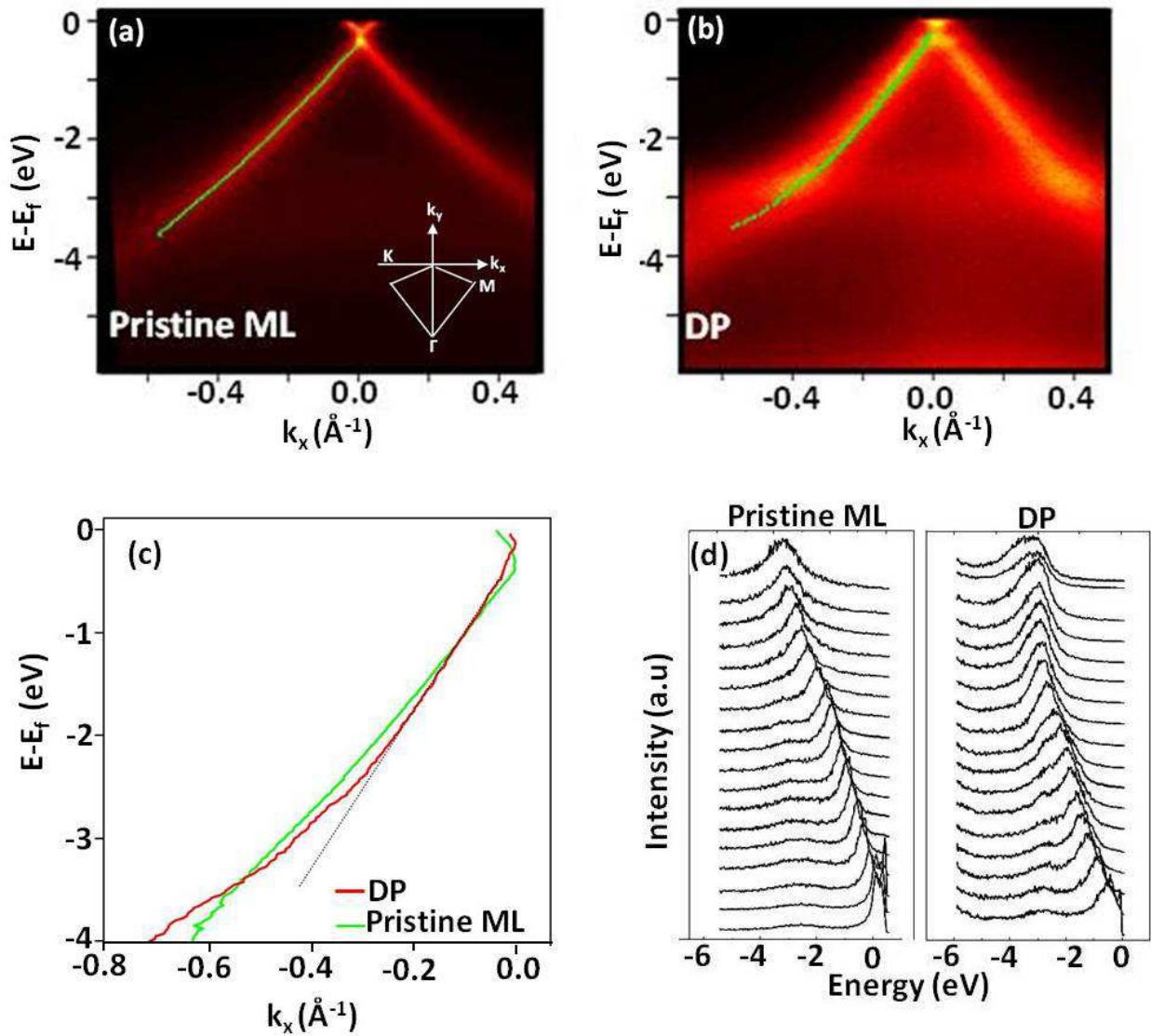


Figure.3.18: ARPES intensity of graphene π band around K points (a) pristine graphene (b) for diluted phase (DP), along the direction schematized in the inset of (a), with superimposed MDC peak positions shown by green lines. (c) Compares the MDC lines of pristine and Diluted phase (d) shows EDC stacks in both cases (K_x values range from 0 to -0.6\AA^{-1} from bottom to top).

Angle resolved photoemission spectra of pristine graphene and graphene monolayer with gold clusters (DP) are shown respectively in Figure 3.18.a and 3.18.b. These dispersions have been measured around the K point (where π and π^* bands touch each other) of Brillouin zone as schematized in the inset of Figure 3.18.a. Momentum Distribution Curve (MDC-intensity cut at constant energy) peak positions are

Chapter 3. Intercalation of gold on Epitaxial Graphene

superimposed on the corresponding experimental dispersions shown by green lines. The respective stacked Energy Distribution Curves (EDC-intensity cut at constant momentum) are also shown in Figure 3.18.d. Characteristic linear dispersions around the K point are observed in both samples. Pristine monolayer (ML) exhibits a sharp dispersion characterized by thin bands and linear until -3eV while DP showed a broader line width compared to the pristine graphene and linear until -2eV and after an abrupt deviation from the linearity when approaching the van Hove singularities (VHs) below -2eV . The abrupt deviation associated to a high increase in the ARPES intensity as well as a large broadening of the dispersion band in the EDC (see figure 3.18(b and d)). This is the characteristic of a strong renormalization of the band structure usually observed in highly doped graphene. Fermi velocity (V_F) of quasiparticles are deduced from the slope of both dispersions and we observed a 20% increase in DP compared to pristine ML. For the pristine graphene, $V_F = 0.99 \pm 0.08 \cdot 10^6 \text{ m.s}^{-1}$ and for DP, $V_F = 1.24 \pm 0.2 \cdot 10^6 \text{ m.s}^{-1}$.

Furthermore, the ARPES measurements near the Dirac point were performed for pristine graphene and gold intercalated graphene (DP) as shown in Figure 3.19. The position of the Dirac point was obtained from the point at which two slopes on dispersion touch each other. In pristine graphene, the Dirac Energy (E_D) $\approx -288\text{meV}$ and for gold intercalated graphene (DP), $E_D \approx -232\text{meV}$. This indicates that there is a weak p-type doping of 56meV induced by the gold clusters. However, such doping was slightly different from the previous Scanning Tunneling Spectroscopy (STS) measurements where no doping was observed. This may be due to the partial oxidation of the graphene sample as ARPES measurements were performed ex-situ while STS measurements were performed in-situ. Although no gap was observed in both cases, dispersion near the Dirac point was strongly modified in DP. A strong mass renormalization around -0.33eV was observed, which promotes a kink of unclear origin. Similarly, a subtle kink was also observed in quasifree-standing graphene on Ni (111) substrate with a continuous intercalated Au layer [48]. This kink was attributed to a residual interaction with gold monolayer due to a mixing with surface Shockley states. A similar kink was observed in

Chapter 3. Intercalation of gold on Epitaxial Graphene

pattern-hydrogenated graphene [137]. However no reason was given for such an appearance.

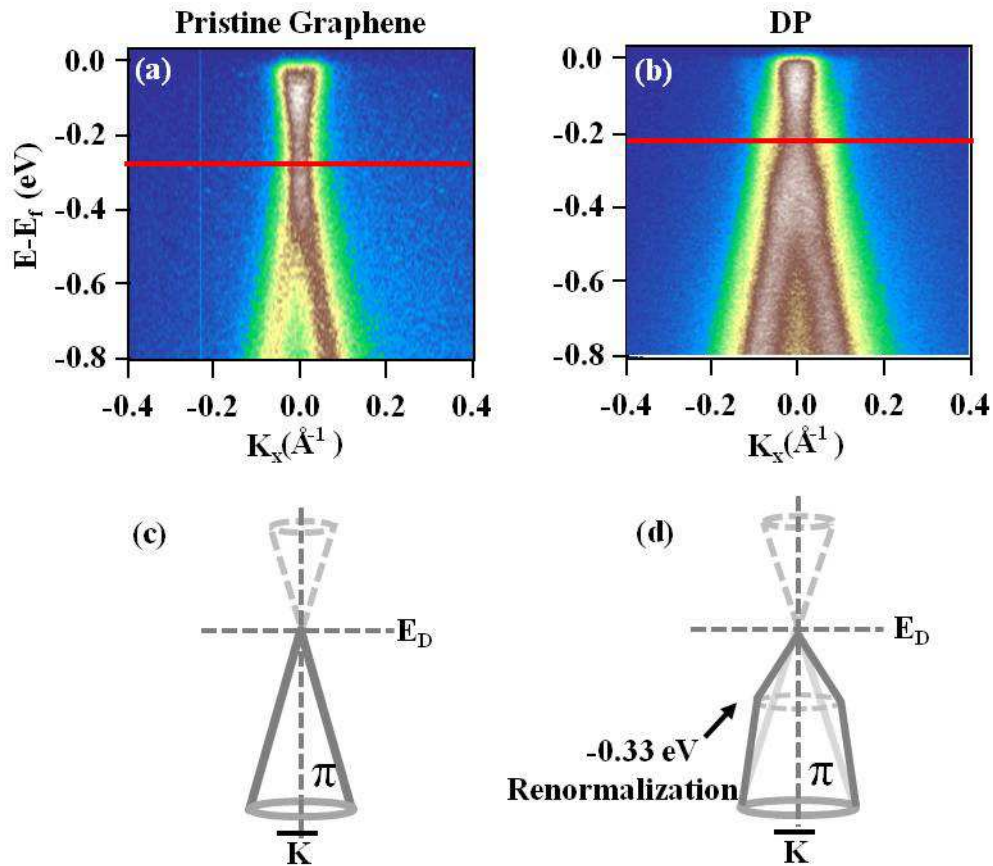


Figure.3.19: (a) and (b) are the ARPES measurements around the Dirac point of pristine graphene and for diluted phase (DP), respectively. (c) and (d) are the schematic diagram of band dispersion around the Dirac point of pristine graphene and DP, respectively. A renormalization is observed around -0.33eV for DP as shown in (d).

Analysis of constant energy surfaces around the M point (is a saddle point where the density of states has singularity referred to as Van Hove singularity.) also showed some interesting results. Figure 3.20(a) shows the three dimensional (3D) representation of the band structure of graphene and the calculated Constant Energy Contours (CEC) shown below, with the topological points of graphene where the dispersion around two adjacent K points meet giving rise to a saddle point and a Van Hove singularity. These VHs were modified by intercalated clusters as shown in the band structure near the M point (Figures 3.18(b) and (c)) as well as an increase of intensity of spectral function. From Figure 3.20(b –d), the dispersion modification in cuts of electronic structure around the M

Chapter 3. Intercalation of gold on Epitaxial Graphene

point at different binding energies was confirmed. In the case of pristine graphene (Figure 3.20.c), the contours meet at -2.8eV and at -2.3eV for intercalated graphene (Figure 3.20.d).

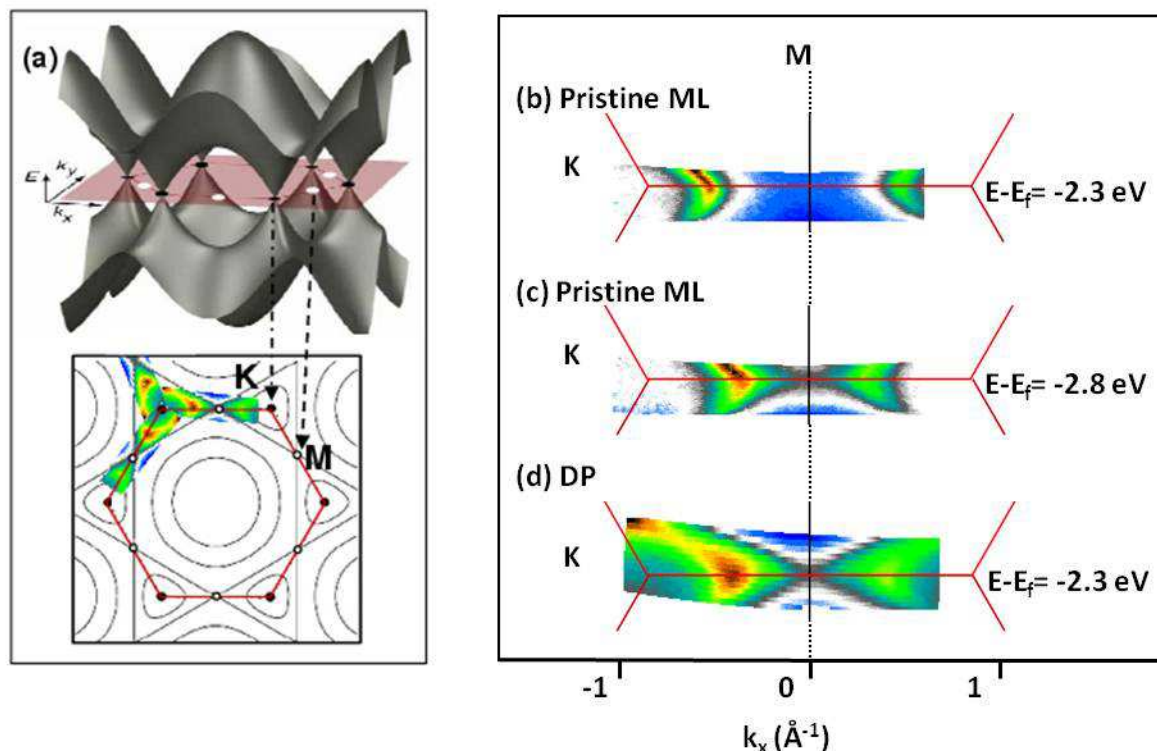


Figure.3.20: 3D representation of band structure of graphene and 2D constant energy contours maps (CECs). The CECs are calculated using first-nearest-neighbor TB approximation. Figure (b) and (c) show Fermi surface around M points for pristine graphene at -2.3eV and -2.8eV respectively and (d) for DP at -2.3eV . The large extension of VHs observed in graphene ML with intercalated gold clusters (DP) at -2.3eV while at the same energy VHs is not reached for pristine graphene. The Fermi surface shown in (d) is indicated in (a).

The Constant Energy Contours (CEC) for intercalated graphene (DP) was strongly warped; the apex of triangular shaped contour was filled when approaching the VHs showing a large increase of the density of states showed in Figure 3.20.d. In conclusion, the modification of the band structure of graphene was observed due to an extension of Van Hove singularity. These results were published in [138].

Chapter 3. Intercalation of gold on Epitaxial Graphene

“These results confirm the interpretation of standing wave patterns and features observed in FT-STs attributed to a large VHS extension supposing that the empty states and filled states symmetry of the graphene band structure is preserved”.

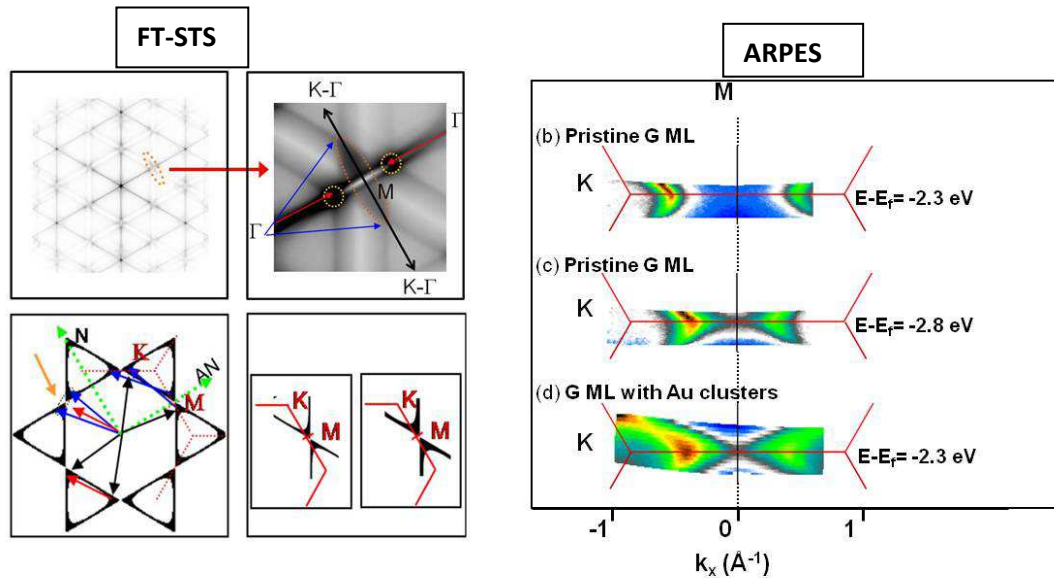


Figure.3.21: Link between FT-STs and ARPES. Extension of VHS expected with FT-STs confirmed by ARPES.

3.9.1. VHS extension, effective mass enhancement and superconductivity

Inspired by the Graphite intercalation compounds (GICs) community and the discovery of superconductivity at relatively high critical temperature, 11.5K for the intercalated alkali metal CaC_6 [139], and up to 30K for the alkali metal and earth metal doped polyaromatic molecules [140], our observations can be revisited in the framework of the superconductivity properties. The mechanism of superconductivity of GICs is still under debate and the origin of this property is still unclear. Graphene becomes to be a play ground for this research field where all theory on the superconductivity are revisited. The classical BCS theory which involves electron-phonon coupling [141] and all exotic phases expected in the vicinity of the van Hove singularity, [142-145].

The ARPES measurements on DP shows that the intercalated gold clusters increases the Fermi velocity of quasiparticles while maintaining its dispersion linear but also strongly modifies the band structure of graphene around the Dirac point as well near

Chapter 3. Intercalation of gold on Epitaxial Graphene

the VHS. Thus the elliptical features observed in FT-STS related to the extension of Van Hove singularity is again confirmed by ARPES. A similar strong Van Hove singularity extension was observed in the case of potassium and calcium intercalated epitaxial graphene, where graphene was strongly 'n' doped by the donor atoms as a consequence the Fermi level was placed at the VHS of π^* states of graphene[89]. They found that the band structure is strongly renormalized by the resulting density of states (DOS) such that VHS has an extended, not point like character as shown below.



Figure.3.22: shows the experimental Fermi surfaces of the samples with various doping leads to extended VHS where the triangular electron pockets at K and K' have merged leading to a flat band. Adapted from McChesney *et al.* [89].

Such a strong extension of Van Hove can increase the critical temperature for superconductivity. The effect of foreign atom states and the rigidity of band structure of graphene are questionable for larger doping in superconducting GIC CaC_6 [146]. In both cases, Fermi velocities of quasiparticles were lower than its pristine form (0.5 to $0.7 \times 10^6 \text{m/s}$) and the intercalant was homogeneously distributed between the graphene planes. However, in our case, the intercalant was inhomogeneous and nearly no doping compared to pristine graphene, Fermi velocity was increased by the intercalated clusters. Also this Fermi velocity of graphene with intercalated clusters was higher than those for epitaxial graphene on SiC for C terminated face [57]. This strongly suggests that the clusters decouple the graphene monolayer from the substrate, which we will discuss later.

Chapter 3. Intercalation of gold on Epitaxial Graphene

In another theoretical study [147], VFs were modified by applying a slight potential oscillation and or corrugation on the graphene layer accompanied by a decrease of the Fermi velocity. They showed that a periodic potential applied by patterned modifications or contacts on graphene's surface leads to anisotropic behaviours such as Fermi velocity renormalization around the Dirac point, gap opening and also the density and type of carrier in a graphene superlattice are extremely sensitive to the applied potential and may further be tuned the Fermi level. Therefore, VFs were affected immediately, either through the modification of hopping potential (theoretically) [148] or by the modification of the rotation angle between two graphene layers (experimentally) [149]. Li *et al.* reported that a rotation between stacked graphene layers can generate VFs, which can be brought close to Fermi energy by varying the angle of rotation [149]. So that the pseudoperiodic potential created by the clusters was the most probable hypothesis for VFs extension. Nevertheless, the reason behind the modification of band structure by these clusters is still a challenging question. That to say, our system offers a platform to study the role of the VFs in superconductivity (VFs extension scenario) in the case GICs.

Recently, by using angle resolved photoemission spectroscopy study on graphite intercalation compounds, CaC₆, Valla *et al.* showed that electron-phonon coupling on graphene-derived Fermi surface to graphene phonons is strong enough to explain an increase in critical temperature T_c , which implies that superconductivity originates in graphene sheets whereas intercalants provide the charge for filling of the graphene π states [70, 150]. However, in this system, no extension of VFs was observed. The electron-phonon coupling changes the dispersion and lifetime of electronic states in the vicinity of the Fermi level, which increases the effective mass of electrons at the Fermi level and density of states is increased [151]. This mass enhancement is evaluated by a parameter λ defined by $m^* = m_0(1 + \lambda)$ where m^* and m_0 are the effective masses with and without electron-phonon coupling respectively. The strength of electron-phonon coupling can be characterized by Eliashberg function $\alpha^2F(\omega; \epsilon, \mathbf{K})$ [152]. Eliashberg function can be defined as the total transition probability of a quasiparticle from/to the state (ϵ, \mathbf{K}) by

Chapter 3. Intercalation of gold on Epitaxial Graphene

coupling to the phonon modes with frequency ω . Therefore, electron-phonon coupling constant is given by

$$\lambda = 2 \int_0^{\infty} \frac{d\omega}{\omega} \alpha^2 F(\omega; \epsilon, \mathbf{K}) \quad (\text{Eq.3.1})$$

Hence, λ can be extracted directly from the real part of spectral function, such that $\lambda = -[\partial(\text{Re}\Sigma)/\partial\omega]_0$ i. e. the slope of $\text{Re}\Sigma$ near 0 eV (Fermi level). The real part ($\text{Re}\Sigma(\epsilon, \mathbf{K}) = \epsilon(K) - \epsilon_0(K)$), gives shift in energy while imaginary part gives life time broadening quasiparticle. The real and imaginary part can be simple extracted from the peak positions k_m and widths Δk of the Lorentzian fitted momentum distribution curves (MDC is an intensity cut at constant energy) at each ω using the expressions

$$\text{Re}\Sigma(\omega) = (k_m - k_0)v_0(\omega), \text{Im}\Sigma(\omega) = \frac{\Delta k}{2} v_0(\omega) \quad (\text{Eq.3.2})$$

where v_0 represents the bare band velocity at ω where there is no many body effects. The choice of bare dispersion plays a significant role in determining the exact shape and magnitude of self energy. Within a narrow energy scale, it is sufficient to approximate the bare dispersion by $\epsilon_0(\mathbf{K}) \approx -\hbar V_F(k - k_F) + \beta(k - k_F)^2$. Thus the bare band dispersion can be extracted in different ways. One way is to extrapolate $\epsilon(\mathbf{K})$ from states at higher binding energy where the renormalization is negligible. Another one is to take $\epsilon(\mathbf{K})$ from calculation of band structure which does not incorporate many body effects. Finally, $\epsilon(\mathbf{K})$ and the self energy can be determined by a self-consistent fitting procedure [153]. Then, from the modified strong-coupled theory of superconductivity [154,155], it is possible to get the expression for superconducting transition temperature which related to the electron-phonon and coulomb coupling constants, is given by

$$T_C = \omega_{log} \exp \left\{ -\frac{1.04(1+\lambda)}{\lambda - \mu^*(1+0.62\lambda)} \right\} \quad (\text{Eq.3.3})$$

Where ω_{log} is logarithmic average phonon frequency and μ^* is the screened coulomb pseudopotential.

$$\omega_{log} = \exp \left\{ \frac{2}{\lambda} \int_0^{\infty} \frac{d\omega}{\omega} \alpha^2 F(\omega) \ln \omega \right\} \quad (\text{Eq. 3.4})$$

Chapter 3. Intercalation of gold on Epitaxial Graphene

In order to start the discussion, we recall the spectral function from chapter2, Eq.2.31.

$$A(\mathbf{k}, E) = \frac{1}{\pi} \frac{Im\{\Sigma(\mathbf{k}, E)\}}{[E - E_k^0 - Re\{\Sigma(\mathbf{k}, E)\}]^2 + [Im\{\Sigma(\mathbf{k}, E)\}]^2}$$

The gold intercalation modifies the band structure, it changes the real part which can be evaluated by the deviation of the band dispersion from the bare band dispersion (band without modification) and the imaginary which gives the FWHM in the MDC. The latter gives the life time broadening of the quasiparticles. We have observed a strong Van Hove extension without doping. Here we would like to evaluate the expected coupling effect at the origin of this deviation in the framework of the GICS and superconductivity property. If we compare directly the bare dispersion with intercalated gold graphene, the estimation of the real part is unsound. Indeed the Fermi velocity is renormalized in the case of intercalated gold, and we need to compare this dispersion with the expected bare dispersion considering that both Fermi velocities are the same. For that we consider the measured bare dispersion (pristine graphene) and consider its polynomial fit to get the whole dispersion. Then the linear value obtained in the fit of the gold intercalated graphene was applied to the polynomial fit of pristine graphene (called as equivalent pristine graphene). By doing that both dispersion are now identical in the linear part and differ only when approaching the VHs. The Figure 3.23. a) shows the spectral intensity of gold intercalated graphene with two superimposed curves of MDC dispersion of gold intercalated graphene and equivalent pristine graphene. The Real part given by (Eq.3.2) where v_0 is expressed in eV.Å. is given in c. Following Valla *et al.* [150], the coupling constant will be estimated from the slope of the real part approaching the VHS, but in our case around -4eV. *We recall here that we do not have overdoped the graphene and this exercise is done to evaluate the coupling if the doping had been done.*

Chapter 3. Intercalation of gold on Epitaxial Graphene

The value is found to be $\lambda=1.5$ which is much more higher than the value found in the case of K intercalated graphite which gives the higher critical superconductive temperature [150]. We cannot directly calculate *what would be* the theoretical critical temperature for several reasons. Firstly, we should have to extract the average phonon frequency with the self-consistency method using the Eliashberg function (Eq. 3. 4). This is not possible as the deviation we are dealing with is not in the vicinity of the Fermi level. Secondly we do not know the value of the reduced coulomb potential expected in our case. However the electron phonon coupling let us expect a critical temperature above 60K in the framework of the McMillan theory using the parameter (phonon frequency and reduced coulomb potential) used for intercalated graphite. The value found for various cuprate semiconductors are $\lambda =2.5$ for LaSrCuO with calculated $T_c = 41K$ and experimental value is 36-40K. And in the case of YBaCuO, λ is 3 with calculated $T_c = 77K$ and for experimental is 85-92K [156]. This gives us a rough estimation of T_c . We would like also to notice that the maximum value of λ is found in the direction of the highest trigonal warping i. e. when the band dispersion is measured along Γ -K-M direction. In our case this value is estimated as the dispersion was measured along M-K-K (green line in Figure 3.23.b)). This means that a much higher λ coupling is expected in our case. The imaginary part of the spectral line is also shown in Figure 3.23 (d). It increases until the VHS, but shows a maximum around -2.2eV. This probably comes from the deviation from linearity which corresponds to the beginning of the trigonal warping which is enhanced in the Γ -K-M. This approach is also not fully rigorous, because we don't know how robust will be the band dispersion for doping and which kind of other renormalization we can expect with strong doping. But previous experiment showed that a much higher VHS extension is expected for strongly doped graphene layer [see for ref.89].

Chapter 3. Intercalation of gold on Epitaxial Graphene

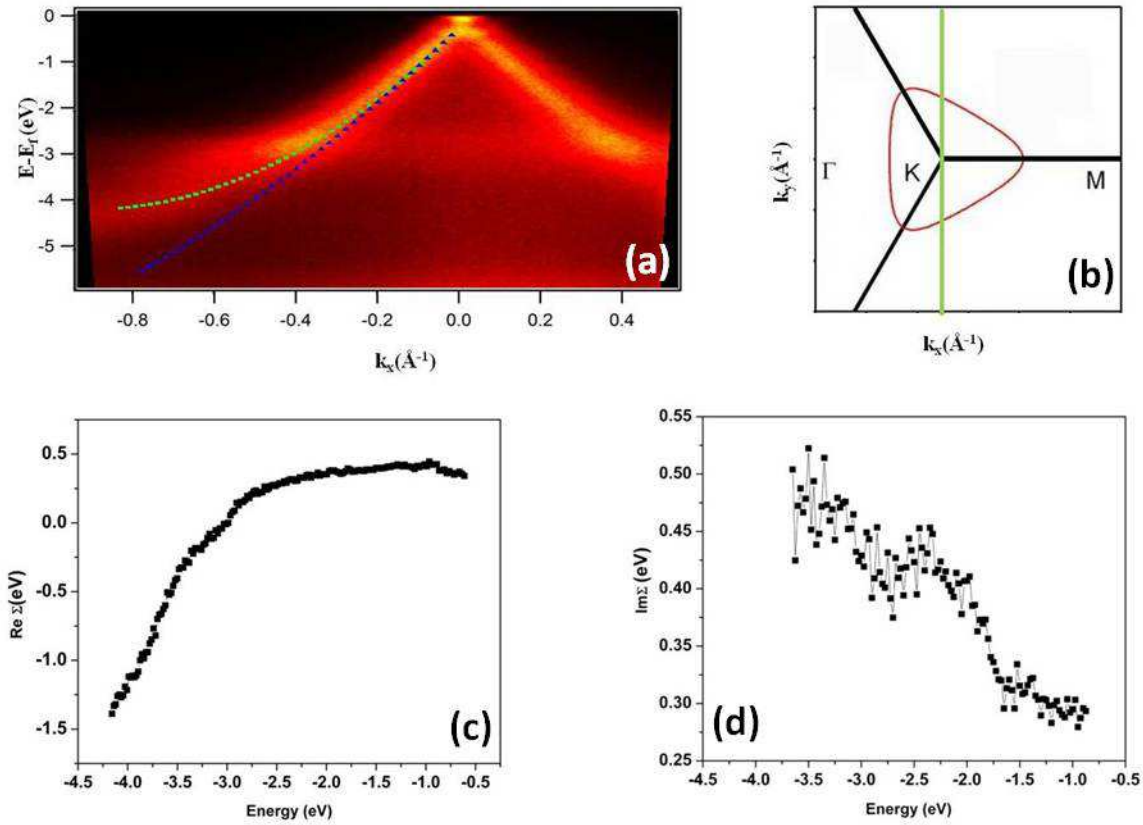


Figure.3.23: (a) Spectral intensity of gold intercalated graphene. Green dotted line represents MDC derived dispersion of gold intercalated graphene and blue dotted line represents equivalent pristine graphene (refer the text above for detail).(b) measured dispersion along the direction of M-K-K is represented by the solid green line. (c) Real part and (d) Imaginary part of self energy.

We would like to come back to an important modification of the band structure which is an increase of Fermi velocity. As given by the equation 3.5, the Fermi velocity is in first approximation proportional to the nearest neighbor hopping energy t and the lattice parameter ($a_G = 2.46 \text{ \AA}$). Our first assumption for the augmentation of Fermi velocity in DP was the release of compressive strain of graphene by the cluster induced decoupling. This leads to an increase of lattice parameter and consequently an increase of Fermi velocity compared to pristine graphene. Therefore, we have carefully verified this assumption by taking Fourier Transform (FT) measurements on the STM topographic images of pristine graphene and DP at different bias. The average lattice parameter taken over several images on the pristine graphene is found ($2.3 \pm 0.07 \text{ \AA}$) while on DP ($2.3 \pm 0.04 \text{ \AA}$)

Chapter 3. Intercalation of gold on Epitaxial Graphene

which are equal in the limit of the uncertainty. These measurements lead to a conclusion that there is no change in the lattice parameter (a_G) of graphene even after the gold intercalation

$$V_F = \frac{\sqrt{3}}{2\hbar} t a_G \quad (\text{Eq. 3.5})$$

If the increase of Fermi velocity (V_F) is not due to an increase of the lattice parameter (a_G) of graphene, the increase in (V_F) may be attributed to an increase of the nearest-neighbor hopping energy t . In the case of bilayer graphene the quasiparticle dispersion is governed by the hopping in one plane while the increase of the effective mass which gives the parabolic dispersion is due to the coupling between the two layers. The highest coupling is found for the Bernal stacking. All sources of decoupling, i.e. the rotation between two planes, which modify the stacking, and the decoupling by increasing the inter-plane distance is susceptible to modify the distribution of the hopping potential values. Here, the second layer is the buffer layer graphene. One aspect of the coupling is the influence of the corrugation induced by the buffer layer. As shown by Lauffer *et al.* [116] the corrugation decreases with the increase of the number of graphene layers in few graphene layers.

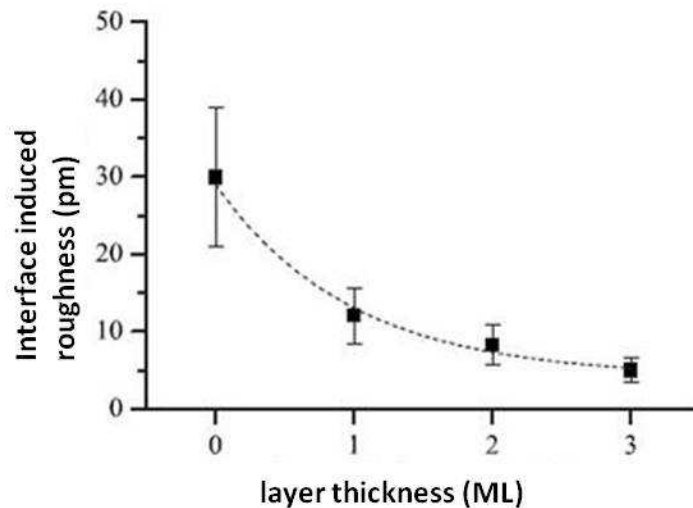


Figure.3.24: Interface induced roughness as a function of layer thickness in monolayer (ML). Figure adapted from Lauffer *et al.* [116].

Chapter 3. Intercalation of gold on Epitaxial Graphene

3.10. Decoupling of monolayer graphene by intercalated gold clusters

To understand decoupling of graphene ML, roughness analysis of graphene between the clusters were investigated. In addition, the transfer of charge from substrate to graphene ML was calculated and the following sections discuss them in details.

3.10.1. Roughness analysis

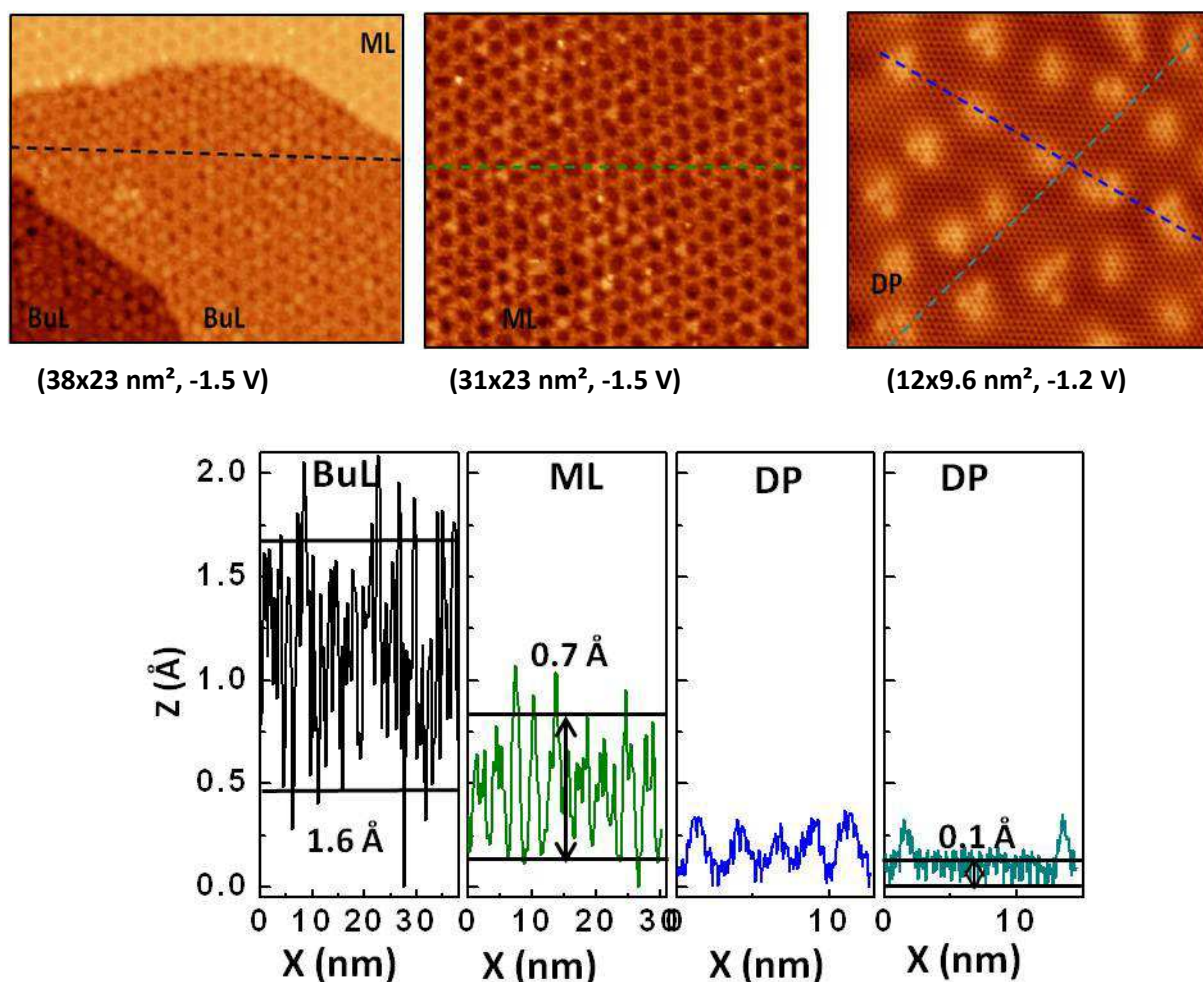


Figure.3.25: The roughness of Buffer layer (BuL, black dash lines), monolayer graphene (ML, green dash lines) and graphene over the gold clusters (blue dash lines) and graphene in between the clusters (cyan dash lines). The corresponding line profiles are shown below.

In order to evaluate the roughness release induced by the clusters, we have measured the roughness between the clusters and compared to the one of the Buffer layer

Chapter 3. Intercalation of gold on Epitaxial Graphene

(BuL) which is approximately 1.6 Å and for monolayer graphene (ML) is 0.7Å. The roughness of graphene between the clusters is 0.1Å. From these measurements, one can conclude that the corrugation associated to the BuL is strongly reduced an order of magnitude in the case of Au intercalated graphene. The graphene layer between the clusters seems to be flat and it is evident that the graphene ML is decoupled from the BuL.

3.10.2. Calculation of charge transfer

Decoupling of monolayer graphene from the substrate is also verified by calculating the transfer of charge from the substrate. The charge transfer is calculated for both pristine and gold intercalated graphene. The number of electrons, at Fermi energy, E_F for $T=0K$ is basically given by dividing the volume of a K-space primitive cell (V_K) by the K-space volume per allowed wave-vector (Ω_K) [157]. So the density of electrons per unit volume V , (n_e) is given by:

$$n_e = d \frac{1}{V} \frac{V_K}{\Omega_K} \quad (\text{Eq.3.6})$$

where d is the degeneracy. Therefore, in graphene, the electron system is two dimensional. The volume Ω_K per allowed wave vector is $\frac{(2\pi)^2}{V}$. The volume V_K of a K-space primitive cell at E_F is one of the Fermi surface, which is πK_F^2 . The degeneracy d is 4 (2×2 for valley and spin degeneracy).

Therefore

$$n_e = 4 \frac{1}{V} \frac{V}{(2\pi)^2} \pi K_F^2 = \frac{K_F^2}{\pi} \quad (\text{Eq.3.7})$$

The dispersion is linear with

$$E(K) = E_D + \hbar V_F K = \hbar V_F (K - K_F) \quad (\text{Eq.3.8})$$

$$E_D = -\sqrt{\pi n_e} \hbar V_F \quad (\text{Eq.3.9})$$

From (Eq.3.9), the density of electrons, n_e for pristine graphene is $6.221 \cdot 10^{12} \text{ cm}^{-2}$ where $E_D = -0.288 \text{ eV}$ and $V_F = 0.99 \pm 0.08 \cdot 10^6 \text{ m.s}^{-1}$ (obtained from ARPES). For intercalated

Chapter 3. Intercalation of gold on Epitaxial Graphene

graphene, $n_e = 2.572 \cdot 10^{12} \text{ cm}^{-2}$ where, $E_D = -0.232 \text{ eV}$ and $V_F = 1.24 \pm 0.2 \cdot 10^6 \text{ m.s}^{-1}$ (obtained from ARPES). Hence, the transferred charges (electron from BuL to Au) are $3.648 \cdot 10^{12} \text{ cm}^{-2}$. With the same transfer of charge from buffer layer, an increase of Fermi velocity V_F , would imply an increase of n-type doping as shown in Figure 3.26.

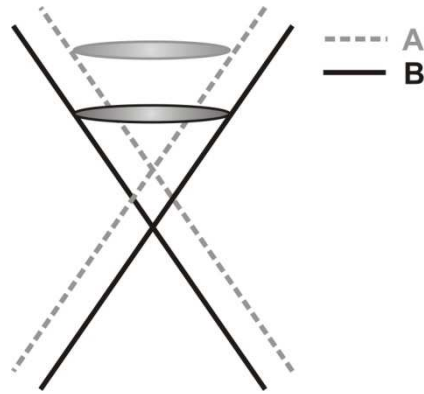


Figure.3.26: Schematic diagram of dispersion near the K point with constant Fermi surface. The dashed gray lines A represents higher slope with larger Fermi velocity V_F , and the solid black lines B represents lower slope with lower Fermi velocity V_F . By keeping the same Fermi area, an increase of Fermi velocity V_F , indicates n-type doping shown by upward movement of Fermi surface (shown in gray circles).

However, here in this case, E_D is almost constant, which means that $V_F \sqrt{n_e}$ is constant also ($E_D \propto V_F \sqrt{n_e}$ from Eq.3.9). This means that decoupling (increase of V_F) goes with decrease on n_e (p-type doping).

3.10.2.1. Charge transfer from Fermi surface measurements

If we assume that the Fermi surface is circular with radius K_F , then the density of electrons (n_e) can be deduced from the Fermi surface using Eq.3.7.

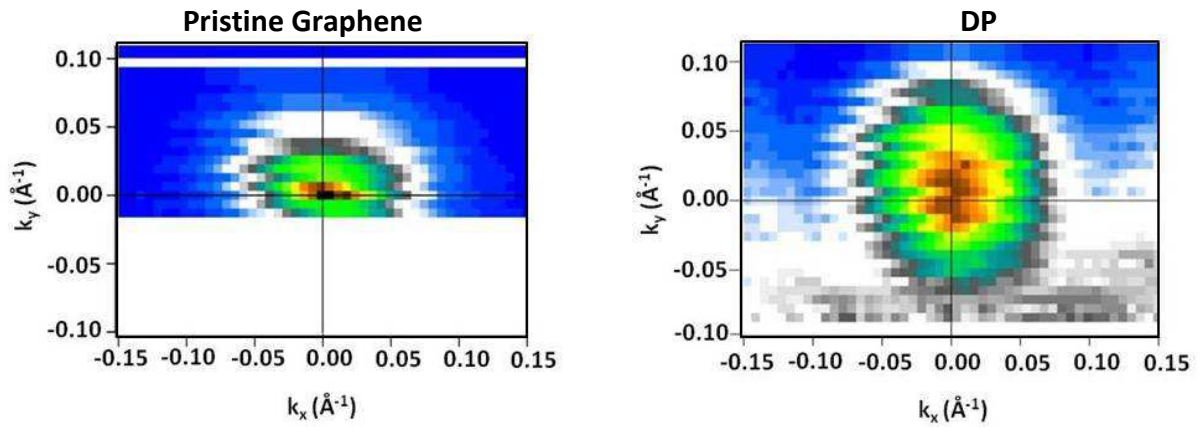


Figure.3.27: Fermi surface measurements of pristine graphene and gold intercalated graphene (DP).

For pristine graphene, $K_F = 0.047 \text{ \AA}^{-1}$ and then $n_e = 7.03 \cdot 10^{12} \text{ cm}^{-2}$ and for gold intercalated graphene, $K_F = 0.055 \text{ \AA}^{-1}$ and then $n_e = 9.63 \cdot 10^{12} \text{ cm}^{-2}$. It was found that the measured value of density of electrons n_e is quite different from the calculated ones. From the calculated n_e , for gold intercalated graphene, $K_F = 0.0284 \text{ \AA}^{-1}$, this was much smaller than the measured value. In fact, such a higher value of measured $K_F = 0.055 \text{ \AA}^{-1}$, refers to the graphene layer on top of the Au atoms are more like n-type doped with $E_D = -0.449 \text{ eV}$ by using $V_F = 1.24 \pm 0.2 \cdot 10^6 \text{ m.s}^{-1}$. This discrepancy is due to the fact that the slope of the dispersion is not equal above or below the Dirac point E_D due to the strong renormalization around the Dirac points (see Figure.3.19 (b) or (d)). If we calculate the Fermi velocity V_F from the measured Fermi surface, using (Eq.3.9), $V_F = 0.93 \cdot 10^6 \text{ m.s}^{-1}$ for pristine graphene and $V_F = 0.63 \cdot 10^6 \text{ m.s}^{-1}$ for gold intercalated graphene. The decrease of V_F in gold intercalated graphene can be explained using the following equation

$$E_D \propto V_F \sqrt{n_e} \quad (\text{Eq.3.10})$$

The slope of dispersion above the Dirac point is smaller than the slope below the Dirac point, thus have large value of K_F , thereby large n_e . By keeping constant E_D with large n_e , the V_F is decreases (Figure 3.28).

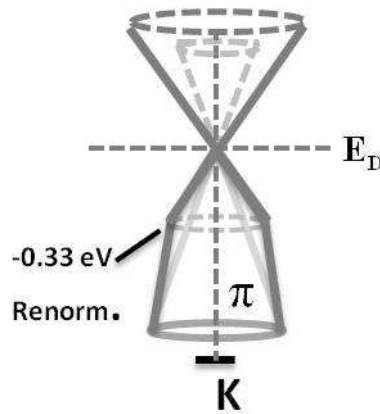


Figure.3.28: Schematic illustrates the dispersion near the K point with two different slopes above and below the Dirac point. The solid line shows the lower slope with large Fermi surface and thus has higher Fermi velocity V_F .

Thus because of the renormalization of the band structure around the Dirac point, the calculated transfer of charge is more precise, which is $6.221 \cdot 10^{12} \text{ cm}^{-2}$ for pristine graphene and $n_e = 2.572 \cdot 10^{12} \text{ cm}^{-2}$ for gold intercalated graphene. There is a difference of charge transfer in both cases, but in the case of intercalated gold the charge transfer is masked by the renormalization around the Dirac point leading to conclude for both pristine and intercalated gold the Fermi level is at the same position even if the charge transfer is different.

3.11. Conclusion

Gold intercalation on EG reveals mainly two types of surfaces with distinctive topography. First one is termed as diluted phase (DP) and the latter is film phase (FP). The DP consists of intercalated gold clusters with an average mean distance of 2.2nm, having no interaction with graphene. The FP arising from the intercalation of 1ML of gold between a MG and the underlying SiC substrate gives a 13×13 -G reconstruction and a $2\sqrt{3} \times 2\sqrt{3} R30$ reconstruction. From scanning tunneling spectroscopy (STS) measurements no doping was found on diluted phase while a p-type doping observed on FP. The bonding property of these gold clusters was examined using differential charge density plot and PDOS calculations. These calculations revealed that the gold clusters are free standing, this was further evidenced by XPS. The position and number of Au atoms were

Chapter 3. Intercalation of gold on Epitaxial Graphene

verified by making a comparison between the experimental STM image and simulated STM images with different positions (under the BuL or between the ML and BuL) and 1 or 3 Au atoms. From the similarity of shape and size in experimental STM image of isolated cluster with simulated STM images, we conclude that gold clusters are composed of one gold atom and that is intercalated between the ML and BuL.

The intercalated gold clusters generate a strong standing wave pattern on monolayer graphene for bias voltage corresponding to unoccupied states from +0.7 to +1eV. These structures are attributed to a screening effect. The gold clusters screen the charge transfer from the substrate to monolayer graphene that creates a charge inhomogeneity on the graphene plane and scatter the quasiparticles. A detailed analysis of the standing wave pattern using FT-STS revealed elliptical features around M points, which have been attributed to large extension of Van Hove Singularities. This has been further confirmed by ARPES measurements.

ARPES characterization of diluted phase demonstrates that the intercalated Au clusters keep the linear dispersion of quasi particles of graphene and increase their Fermi velocity. A strong mass renormalization was observed near the Dirac point, which promotes a subtle kink of unclear origin. Interestingly, no doping was found on DP compared to pristine graphene from the detailed ARPES measurements. Large extension of VHs was observed from the Fermi surface around M points confirmed the link between ARPES and FT-STS. The increase of Fermi velocity has finally been attributed to a modification of the hopping potential due to the decoupling from the BuL which has been proved by roughness analysis of graphene between the clusters and charge transfer calculations.

Abstract: Chapter 4. Molecules on Epitaxial graphene

Abstract: Chapter 4. Molecules on Epitaxial graphene

Dans ce chapitre nous abordons le problème du dopage par l'interaction avec des molécules donneuses d'électrons afin d'amener le niveau de Fermi au niveau des singularités de van Hove. Les molécules utilisées ici sont des Tetrathiafulvalene derivatives (TTFm). Jusqu'à présent une seule étude de photoémission a reporté un dopage de type n pas le dépôt de ce type de molécules. Aucune étude n'a permis de connaître précisément la conformation des molécules sur le substrat de graphène et les conditions de transfert de charge. Dans notre cas, les chimistes ont ajouté des chaînes alkyles aux molécules afin d'accroître l'interaction molécule/graphène. L'étude STM montre que les molécules adoptent une conformation de type « edge-on », perpendiculaire au substrat, elles forment ainsi des lignes parfaitement ordonnées avec un assemblage supramoléculaire de type empilement π - π . Les chaînes alkyles sont en interdigitation fortes et c'est cette interdigitation qui est à l'origine de cette conformation pour laquelle le transfert de charge n'est peu ou pas possible avec le substrat. Dans certaines régions une conformation « à plat » est observé est l'interdigitation des chaînes latérales modifiées. Des mesures STM en milieu liquide montrent un ordre différent avec toutes les molécules « à plat » sur la surface en interaction π - π avec le substrat de graphène. Dans ce cas le rôle du solvant dans le processus d'auto-assemblage est mis en évidence. Nous montrons donc ici l'implication entre la conformation et la fonctionnalisation du graphène, ici le dopage de type n. Dans une seconde partie de ce chapitre nous présentons les résultats obtenus sur le dépôt de molécules photochromes à base de diarylethene connectées à des molécules conjuguées.

Chapter 4. Molecules on Epitaxial graphene

4. Molecules on Epitaxial Graphene (EG)

This chapter is devoted to the study of deposition of different molecules on epitaxial graphene (EG) to understand the reactivity of graphene with molecules and to functionalize graphene on both sides. Due to the inertness of graphene surface, graphene promotes the molecule-molecule interaction in the self-assembling process, this chapter highlight the interplay between the conformation of the molecules and the expected properties such as a transfer of charge with the graphene layer for the application of molecular electronics.

The first part discusses the deposition of Tetrathiafulvalene derivatives (TTFm) on pristine graphene and gold intercalated graphene. In the following of the previous chapter the aim is to strongly n-dope the gold intercalated graphene and to put the Fermi level at the VHS by depositing electron donor molecules. The graphene layer is modified on both sides, one side with gold- the band structure is modified and on the other side the position of the Fermi level is adjusted, leading to the realization of Graphene Based Hybrid structures (GBHs).

The second part deal with study of photochromic diarylethene and conjugated molecules on graphene. Diarylethene is a molecule, which has two conformations open/close by light switching, and the goal was to connect these with conjugated molecules. The conjugated molecules were studied by STM in the framework of the thesis of R. Shokri in collaboration with the University of Freiburg. Here the self-organization process of diarylethene connected with long conjugated molecules was studied.

4.1. TTFm molecules on Epitaxial graphene

Tetrathiafulvalene (TTF) and its derivatives exhibit strong electron-donor abilities and have been successfully used as building blocks to form charge transfer salts and organic conductors because of their rich electron nature due to the core sulphur atoms [158]. TTF is an important constituent in supramolecular chemistry, crystal engineering, molecular conductors and superconductors [159-161]. TTF display efficient nonlinear

Chapter 4. Molecules on Epitaxial graphene

optical responses (NLO) in the second and third harmonic generation which provide a promising strategy for the molecular engineering of switchable NLO materials [162]. The majority of TTF's applications are determined by the donor abilities of this molecule, which are the result of the high-lying HOMO [163]. Recently, the charge-transfer doping in few-layer graphene covered with TTF molecules has been evidenced by X-ray photo electron spectroscopy (XPS) [164]. Voggu *et al.* [165] has shown the effect of charge transfer interaction of graphene with electron donor (TTF) and acceptor molecules using Raman spectroscopy, UV-Visible absorption spectroscopy and electrical resistivity measurements. In their study, Raman G-band softens progressively with increasing concentration of TTF, the occurrence of charge transfer band at 500-800nm region in the electronic absorption spectra and the increase of electrical resistance with increasing concentration of TTF strongly reveals the charge transfer of TTF molecules to graphene. Recently, in a theoretical paper, Sun *et al.* [166] has shown that upon adsorption of TTF molecules on graphene, with molecules laying flat on the surface, charge is transferred from the π orbital-dominated HOMO of TTF to the π orbitals of graphene. The most important feature is that upon adsorption of TTF on graphene there is a screening layer at the interface, which prevents further charge transfer from TTF to graphene. It has been shown theoretically that, charge transfer from TTF to graphene creates a positive dipole pointing toward TTF molecule and the work function of TTF- adsorbed graphene will decrease due to this positive dipole. This obeys the commonly accepted rule that "electronegative adsorbates increase the work function of the surface, and electropositive adsorbates decrease the work function of the surface" [167]. It is not necessary to deposit several layer of molecules and that all is fully governed by the conformation of the first molecular layer and its ability to transfer the charge into the graphene layer. This transfer occurs only if TTF is flat on the surface i.e. by aligning π orbital of TTF with π orbital of graphene.

In all these works, it was not reported the detailed studies of the conformation of the molecules. Therefore, the aim of this study was to investigate the effect of charge-

Chapter 4. Molecules on Epitaxial graphene

transfer doping of epitaxial graphene on SiC(0001) doped with TTF molecules. Consequently to tune the Fermi level in the vicinity of VFs as in the case of Ca and K doped graphene [89] and thus to investigate the effects of functionalization on both sides of epitaxial graphene by depositing these molecules on top of gold intercalated graphene using ARPES. Unfortunately, we could not achieve this goal due to the relocation of our lab. So some of the preliminary obtained results are discussed, particularly dealing with the self-organization process and conformation at the graphene surface.

The molecules used in this study was derivative of TTF with four dodecylthio side chains TTF(SC₁₂)₄ or so called TTFm synthesized by C. Mattioli from CEMES, Toulouse in the frame work of the CHIMIGRAPHN ANR. The full name of the molecule is 1,3-Dithiole,2-[4,5-bis(dodecylthio)-1,3-dithiol-2-ylidene]-4-5-bis(dodecylthio) tetrathiafulvelene, C₅₄H₁₀₀S₈. The scheme of the TTFm molecule is shown in Figure 4.1

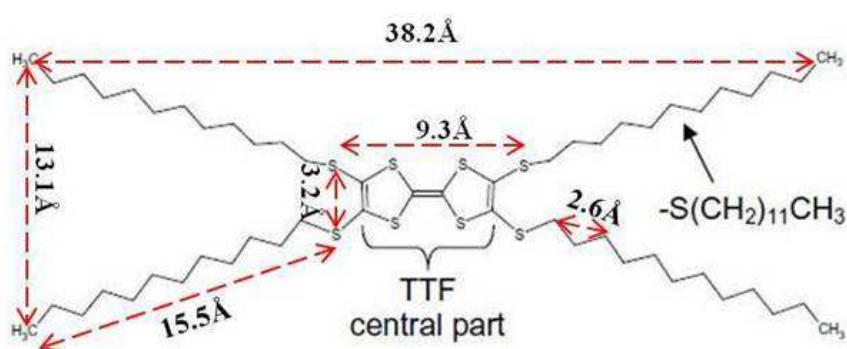


Figure.4.1: The scheme of TTFm molecule, where the TTF core with four dodecylthio side chains.

The TTFm molecules were deposited on pristine epitaxial graphene and gold intercalated epitaxial graphene grown on SiC(0001). The results obtained on both of these samples are discussed below.

Chapter 4. Molecules on Epitaxial graphene

4.1.1. TTFm molecules on pristine epitaxial graphene on SiC(0001)

The preparation of epitaxial graphene sample was already discussed in chapter 1. The TTFm molecules (orange colour powder) were deposited on graphene by evaporation from 420K to 490K, while the sample held at room temperature. The molecules in the glass test tube underwent a phase transition from solid phase to liquid phase during the heating and the measured melting temperature of these molecules was around 340K at a pressure in the 10^{-7} mbar range. After the molecule deposition, the characterization of the samples was performed with the LT-STM from Omicron at 77K at a base pressure in the 10^{-11} mbar range.

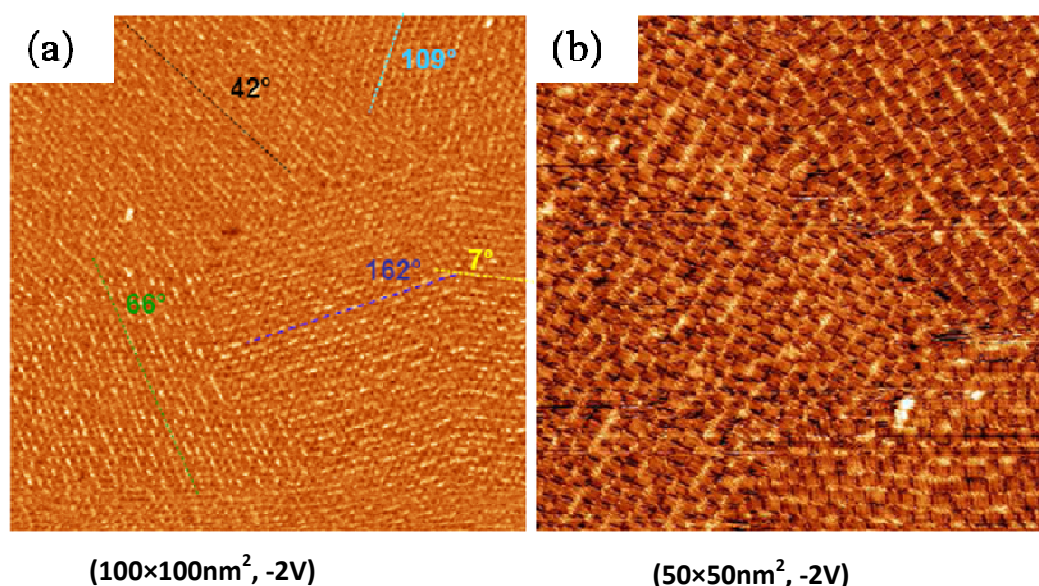


Figure.4.2: STM topographic images of TTFm molecules on pristine epitaxial graphene. a) and b) show self-assembled molecules on graphene forming domains of parallel rows with different orientations. The orientations of rows in the image a) are given with respect to the horizontal. b) shows the zoom of a), where the molecules are tightly packed manner.

After the deposition of TTFm molecules, the surface was completely covered with layer of molecules. Figure 4.2 shows the STM topographic images of TTFm molecules on pristine epitaxial graphene. From the Figure, it is clear that the graphene sample surface is completely covered with self organized TTFm molecules. The TTFm molecules formed domains of parallel rows with different orientations as shown in Figure 4.2 a. Figure b)

Chapter 4. Molecules on Epitaxial graphene

shows the zoom of a) which do not match with the hexagonal symmetry of graphene. This indicates a weak molecule-substrate interaction. The three dimensional growth of molecules were not observed on the surface. The molecules were arranged in a closely packed manner (Figure 4.2.b).

Despite the tip was stable enough to image the self organized molecules, in some areas such as borders of the terrace or borders of domains with different orientations, the tip was unstable. This illustrates the high mobility of molecules on graphene even at 77K. Molecules are stabilized only in the formation of the supramolecular layer, near defect or step edges where the layer is not stable enough.

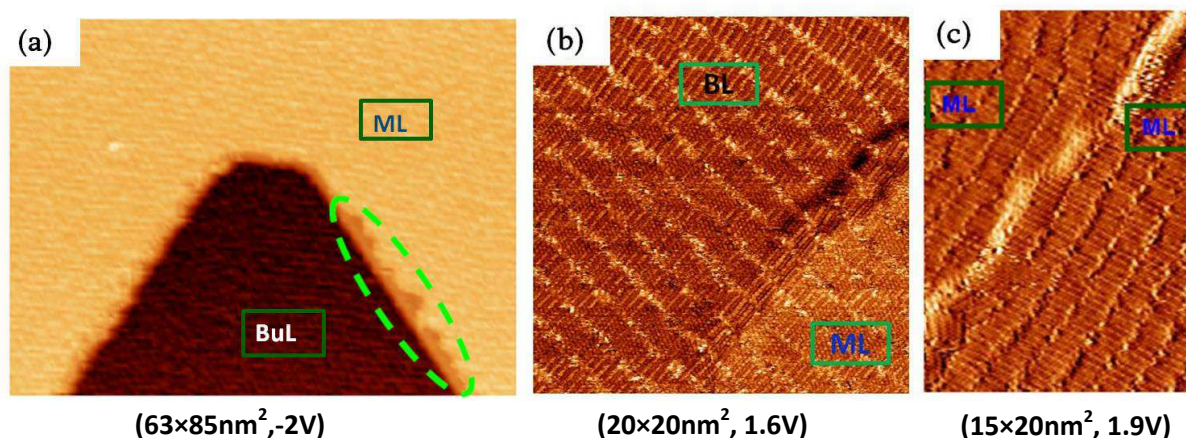


Figure.4.3: STM topographic images of TTFm molecules on pristine epitaxial graphene. The green ellipse in (a) highlights the discontinuity of molecular layer at the border of a terrace. Whereas in (b) (the step height is 3.35\AA which corresponds to the space between two graphene layers) and in (c) (the step height is 2.54\AA which corresponds to 1 SiC bilayer spacing) the molecules form a continuous layer.

Figure 4.3 shows the STM images of self assembled layer of TTFm molecules on pristine graphene organized in different areas of the surface. Figure 4.3. a) shows the organization of the molecules at the border of the terrace, where the molecules are discontinued shown by a green ellipse, while in b) and c) the molecules form a continuous layer. This is possible because a graphene sheet covers the whole surface and is continuous even over the step edges. Where we observe a monolayer graphene (ML), this graphene sheet is on top of the buffer layer (BuL), when we have bilayer graphene, the top

Chapter 4. Molecules on Epitaxial graphene

graphene sheet is on top of a monolayer graphene. However, a few areas of the buffer layer are still visible on the surface (Figure 4.3 a). In this case, the graphene layer is disrupted at the edge of the BuL/ML step edges, and we observe that the molecular carpet is interrupted as shown Figure 4.3 a). In b) and c) the molecules are continuous at the border and cross the step edge without defect.

The measured thickness of the molecular layer is $\sim 1.7 \pm 0.02 \text{ \AA}$. This confirms that the sample surface is covered with only one monolayer of molecules and their long molecular axis is parallel to the surface as the length of the molecule is 3.8nm. The TTFm molecules can be laid planar or tilted on the surface. The distance between the molecular wires and the distance between the molecules within the wires are measured as shown in Figure 4.4. The mean distance between the wires is $1.62 \pm 0.05 \text{ nm}$ (Figure 4.4 c) which is approximately the length of only one dodecylthio side chain. This means that the dodecylthio side chains are fully interdigitated. The distance between the TTF core (brightest structure) within the molecular wire is $0.40 \pm 0.03 \text{ nm}$ (Figure 4.4 d). We have also measured the periodic feature inside the dodecylthio side chains which is $0.25 \pm 0.03 \text{ nm}$, and this distance corresponds to the distance between two second nearest-neighbour carbon atoms within the dodecylthio side chains (Figure 4.4 e). This indicates that only half of the carbon atoms of the side chains are imaged by STM. This could be an interference process with arm chair plane in the direction of the zig-zag but could also be attributed to an edge on conformation of the molecules. As the TTF molecular rows are not always oriented in the same direction with respect to the graphene, we think that this indicates an edge-on conformation. The edge-on conformation of molecules are supported by the molecular modelling shown Figure 4.5 b) where the distance between TTF core is less than 0.5nm when they are off plane geometry is nearly same as the distance obtained from STM. Obviously the bright spots attributed to the high density of states provided by TTF cores.

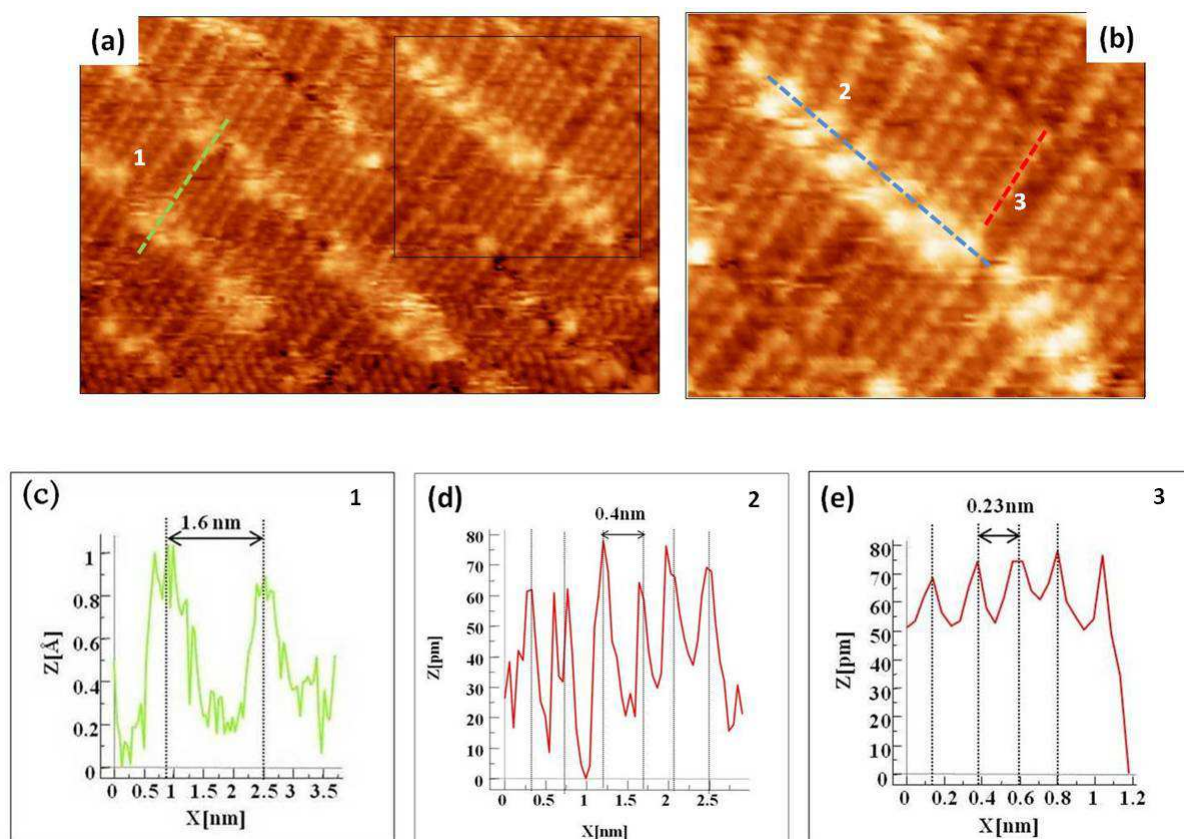


Figure.4.4: (a) STM topographic image of TTFm molecules (11nm× 5nm, 1.6V) (b) the zoom of molecular line in (a) (5nm×4 nm, 1.6V). Line profile for (c) distance between the molecular wires (d) distance between the TTFm bright core (e) distance between the second nearest C atoms within the side chain.

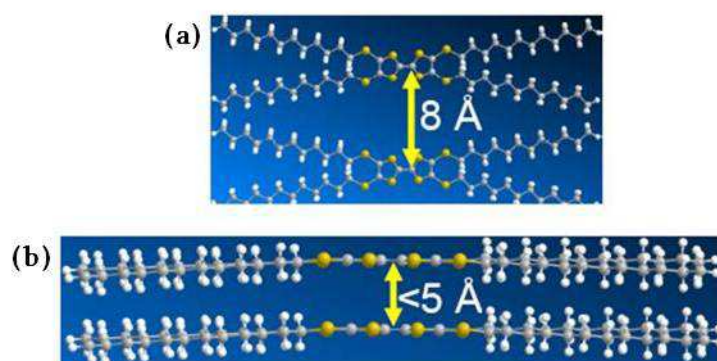


Figure.4.5:(a) Molecular modelling two free TTFm molecules give a distance of 8Å between them when these two molecules are laying flat next to each other. (b) Shows a distance smaller than 0.5nm if molecules are on edge-on conformation.

Chapter 4. Molecules on Epitaxial graphene

From the Figure 4.6.a, we can clearly see that the bright lines (TTF core) are not continuous and we observed some black areas in between. The black areas are also associated to the contrast modifications in the alkyl chain. The origin of these black regions is not yet clear. We think that it could be attributed to a modification of the TTFm conformation. Indeed, the lateral alkyl chains are still observed with no obvious missing rows. This tends to think that the molecules are laying flat or the angle between molecules and the substrate is changed.

In Figure 4.6 a) and b) both alkyl chains and TTF core are clearly visible. This means that TTF core is not missing. Figure 4.6 a) shows bright lines with disruption along the TTF core as indicated by the red arrows. When a bright spot is missing or black, the alkyl chains around are perturbed but not missing. As shown in b) around bright spots the alkyl chains seems to be in edge-on conformation, one per two carbon atoms is visible while for alkyl chains connected to the black (less contrast) spots, they appear to be flat (all carbon atoms are visible) which creates a large space with neighbouring alkyl chains. The alignment of alkyl chain is perturbed each time when the central bright line is disrupted. A counter argument would be to say that TTF is missing as they are not obvious. In figure c) the TTF core are intense and alkyl chains are also visible but not well resolved. The black region as seen in a) for example as indicated by a separate box in b) which is zoomed in d). We can clearly say that TTF are not missing in the less contrasted region. Then our conclusion is that TTF is more flat on the surface. Also we observe the length of interdigitated side chains is slightly different around the dark and bright features. Between two bright lines, the length of interdigitated side chain ($1.62 \pm 0.05 \text{ nm}$) is longer compared to the length of side chains between the dark and bright structure ($1.55 \pm 0.05 \text{ nm}$). This indicates that the bright feature corresponds to the TTF core sulphur atoms, when they are in edge on conformation; there is probably no charge transfer to the substrate. Therefore, we can expect columbic repulsions which will increase the distance. On the other hand, the dark feature corresponds to the molecules, when they are laying flat on the surface and a charge transfer to the substrate is expected. Therefore we can expect a columbic attraction which will reduce the length of interdigitation. Therefore

the interdigitated side chains play a significant role to determine the conformation of molecules.

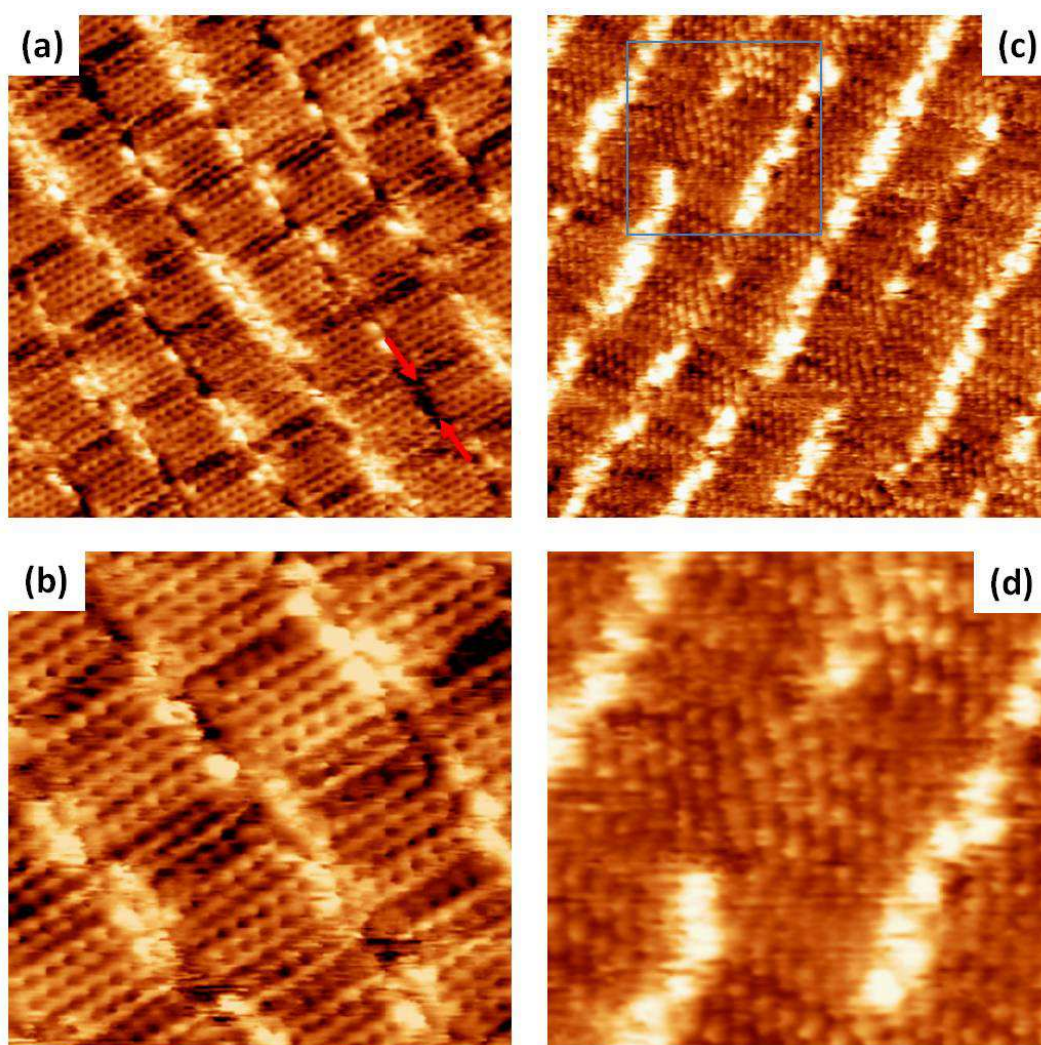


Figure.4.6: STM topographic image of TTFm molecules. a) shows bright lines with disruption along the TTF core as indicated by the red arrows ($10 \times 10 \text{nm}^2, -2\text{V}$) b) shows the zoom of (a) where around bright spots the alkyl chains seem to be in edge on conformation ($5 \times 5 \text{nm}^2, -2\text{V}$). In c) the TTF core are intense and alkyl chains are also visible but not well resolved ($10 \times 10 \text{nm}^2, 1.4\text{V}$) (d) shows the zoom of (c) where no missing of TTF core ($5 \times 5 \text{nm}^2, 1.4\text{V}$).

The performance of TTF devices strongly depend on the packing structures of TTF molecules between electrodes. Therefore, many efforts have been contributed to disclose the factors that regulate the packing behaviours of TTFs on surfaces. In particular, the solvent effect is found to significantly affect the intermolecular interactions. The use of

Chapter 4. Molecules on Epitaxial graphene

specific solvents can control the pattern of TTF [168]. Abdel-Mottaleb *et al.* [169] have shown by STM that bear TTF, TTF with one, two, or four alkyl chains of different lengths and different functional groups at a liquid/graphite interphase- that all of them have the TTF core essentially coplanar with the surface. However, it has been shown that the presence of hydrogen bonds in amide groups enhance the π - π stacking of molecules thus TTF core is tilted perpendicular to the HOPG surface [170]. Moreover, TTF molecules with long alkyl chains assemble into one-dimensional stacks in which long alkyl chains promote intermolecular π - π overlapping acting as so-called molecular fasteners. Molecular fasteners are such that the central skeleton has been fastened with long alkyl chains. This was interpreted as an effect of the van der Waals interactions between the alkyl chains which fastens the TTF cores of neighbouring molecules tightly along the stacks. This observation was obtained on the TTF crystal [171]. With the aim to promote the molecule-substrate interaction, thus to enhance the transfer of charge from molecules to substrate we have introduced long alkyl side chains with TTF core. Despite that, the alkyl side chains promote the intermolecular π - π overlapping consequently fully interdigitated which leads to an edge on conformation of the TTF core, consequently hinders the charge transfer. Our assumption was that a different organization could be obtained in UHV. To our knowledge, without adding specific bonds (amide groups) this is the first example where an edge-on with π - π stacking is observed. The distance between the closer S-S sulphur is below 4Å. This is also the first time that both conformations can be observed in the same supramolecular layer. This asks the question how could we modify this conformation with external stimuli.

4.1.2. TTFm molecules on gold intercalated epitaxial graphene on SiC (0001)

The same preparation method was employed to deposit TTFm molecules on gold intercalated graphene. Prior to molecule deposition, gold intercalation was carried out on the pristine epitaxial graphene. The method of gold intercalation on epitaxial graphene is explained in chapter 3. After several cycles of annealing, gold 3D islands were still present on the sample surface. The deposition of TTFm molecules was done at 150°C for 5 minutes

Chapter 4. Molecules on Epitaxial graphene

with a pressure ranging from 8.10^{-7} mbar to $1.4.10^{-6}$ mbar. The same characterization method was employed here.

The STM images of physisorbed layers of molecules exhibit equally spaced continuous lines of high tunnelling current, indicate the formation of supramolecular wires of the surface.

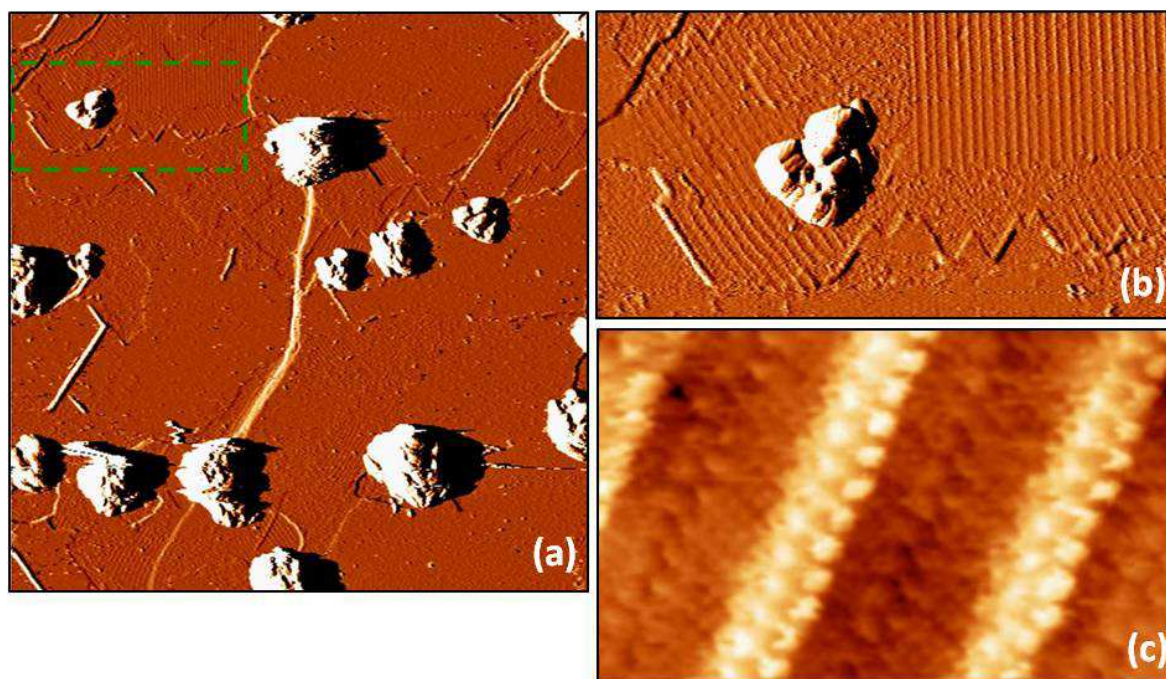


Figure.4.6: STM topographic images of TTFm molecules on gold intercalated epitaxial graphene. a) ($400\times 400\text{nm}^2$, -1.8V) and b) ($150\times 79\text{nm}^2$, -1.8V) show the big gold islands and molecular domains of parallel rows with different orientations c) ($8.6\times 5.2\text{nm}^2$, -2V) is the zoom of b) shows the bright molecular line.

As in the case of pristine epitaxial graphene, the TTFm molecules were self assembled on the surface and formed domains of parallel rows with different orientations as seen in Figure 4.6(a-b). However it was not clear that the molecules were adsorbed on gold intercalated region or on undoped epitaxial graphene layer. The distance between the molecular wires is $3.5\pm 0.1\text{nm}$ and between the TTF core within the molecular wire is $0.48\pm 0.05\text{nm}$. Here the distance between the molecular wires is two times (!) larger than the distance in the case of pristine sample. We can assume that the molecules are following the edge-on conformation on the intercalated gold sample as in the case of

Chapter 4. Molecules on Epitaxial graphene

pristine graphene. The increased distance between the molecular wire leads us to the conclusion that the side chains are not fully interdigitated unlike in the case of pristine graphene. This may be due to the difference in corrugosity of graphene layer or work function induced by intercalated gold leading probably to a slight modification of the van der Waals interaction. It is difficult to go deeper in the discussion and interpretation of this self-organized process. But small modifications of the graphene layer, as observed by gold intercalation, are able to strongly modify the self-organization. An edge-on conformation is preserved but the interdigitation is strongly modified and the distance between the molecular wires is multiplied by two.

However, in both cases, for pristine graphene and gold intercalated graphene in UHV, the molecules follow edge on conformation and thus promoting intermolecular interactions. This may be due to the interdigitation or van der Waals interaction between the side chains which enhance the intermolecular π - π overlapping of neighbouring TTF core as observed in a crystal, there in a 3D growth [171]. One more time, this demonstrates that graphene is an ideal substrate to follow the self-organization of supramolecules and promote the molecule-molecule interaction instead of molecule-substrate interaction.

In conclusion the weak molecule-graphene interaction, as well as the interplay between the alkyl chain conformation, their propensity to interdigitate and their interaction with the substrate which tends to lay them flat on the surface in a arm-chair conformation finally leads to edge-on conformation of the sulphured core. The expected charge transfer is probably not done. However this study shows that this conformation could be tune by the interplay of the alkyl-alkyl interaction, their interdigitation length and the molecule-substrate interaction.

4.1.3. TTFm molecules on graphite

The TTFm molecules follow edge on conformation on epitaxial graphene in UHV so there is no charge transfer to the substrate. Therefore, to understand the conformation of molecules in solution, we have deposited the solution of TTFm molecules in phenyl

Chapter 4. Molecules on Epitaxial graphene

octane solvent on HOPG in ambient conditions. Figure 4.7(a) shows the STM topographic image of TTFm molecule in phenyl octane solvent on graphite. Contrarily to the observed self-organization process in UHV on graphene we do not observe molecular line but a hexagonal structure. The conformation of the molecules is totally different but in accordance with all previous studies [169]. Fig. 4.7 (b) shows the line profile of TTF core and the average distance between the TTF cores is found to be 2.2 ± 0.14 nm. This distance is in accordance (even if we have a drift in the image) with the distance between the TTF core when they are laying flat as illustrated by the model obtained from chemsketch in figure (c). This signifies that the molecules are laying flat. The interaction with the graphite surface and the alkyl chains is much more higher than for the graphene surface. The difference in molecular structure could be also due to effect of solvent or the imaging conditions or simply to the higher molecule-substrate interaction in the case of graphite surfaces. We project to study the deposition of the TTFm molecule on graphite surface but under UHV condition in order to solve this question.

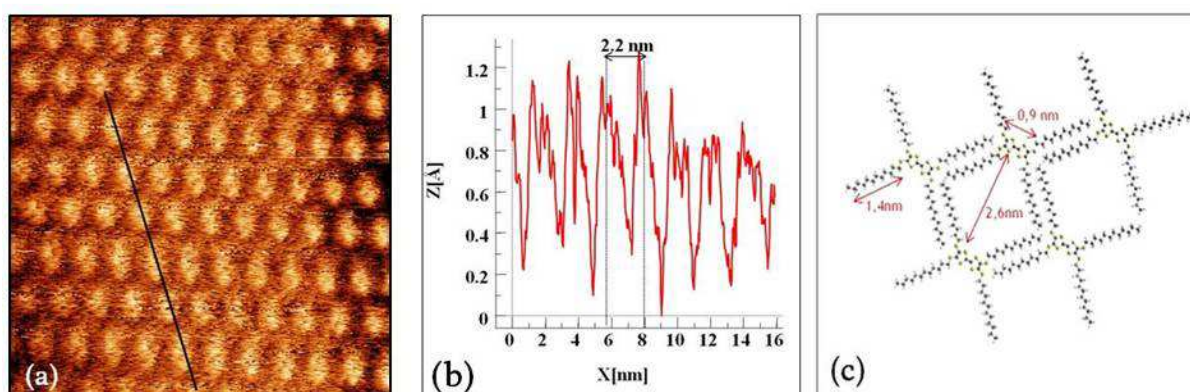


Figure.4.7: (a) STM topographic image of TTFm molecule in phenyl octane solvent on graphite ($16.6\text{nm} \times 16.6\text{nm}$, -1V) (b) line profile of distance between TTF bright core (c) Scheme of TTFm molecules when they are laying flat.

4.2. Photochromic molecules on graphene.

Graphene is an ideal substrate for molecule deposition because of its chemically inert nature. Due to this property, it is able to minimize the interactions between the substrate and molecules and increase the molecule-molecule interaction thus promoting the self assembly of molecules. Graphene can also preserve the photochromic property of

Chapter 4. Molecules on Epitaxial graphene

the molecules. Therefore, by taking the advantage of this property, we have deposited photochromic molecules on epitaxial graphene.

4.2.1. Diarylethene molecules

Diarylethene is a photochromic molecule, i.e. a compound that undergoes a reversible photo transformation between two stable states with markedly different optical and electronic properties and different geometries. When irradiated by light (at specific wavelengths), the molecule undergoes a ring-closure/ring-opening reaction with a whole delocalization/separation of the π -electrons inside the molecule.

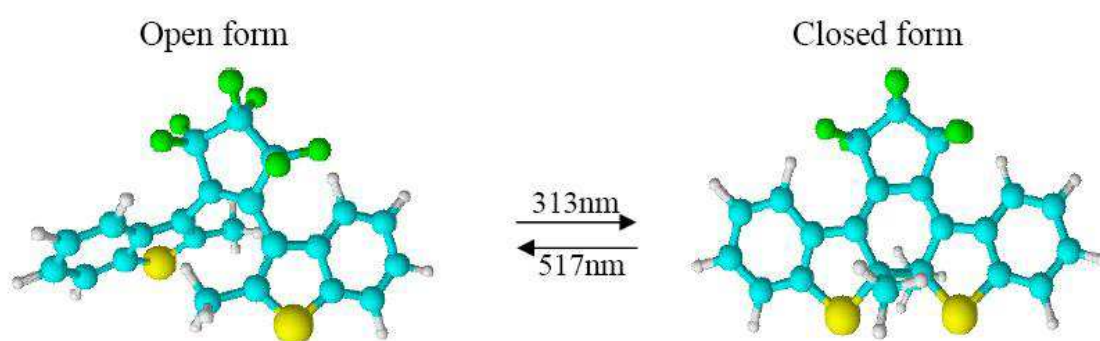


Figure.4.8: Diarylethene molecules in its open and closed conformation.

Diarylethene molecules are very promising photochromic candidates because of their thermal stability, high fatigue resistance (i.e. occurrence of side-reactions is very rare), high addressability (because wavelengths for inducing cyclization and decyclization reactions are well separated), fast response time and high cyclization and cycloreversion quantum yields (both are quite dependent on the functional side groups R) [172].

Figure 4.9 shows that photocyclization reaction is only possible when the distance between the two reactive carbons (shown by red arrows) is smaller than 0.42 nm [173]. Diarylethene molecules with only open anti-parallel conformation can take part in a photocyclization reaction while open parallel form is photochemically inactive, as photoisomerization is fulfilled by Woodward-Hoffmann rule [174].

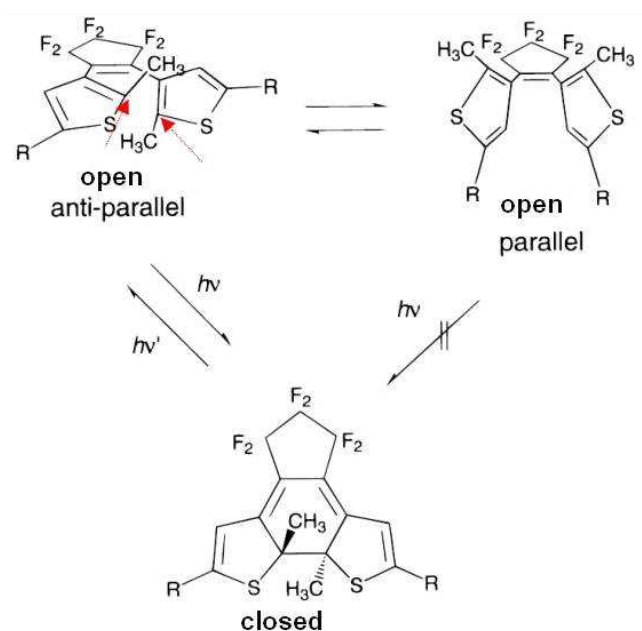


Figure.4.9: Photocyclization reaction of diarylethene molecules.

According to Woodward-Hoffmann rule, for a system containing $(4n + 2)$ pi electrons (6 pi electrons in diaryl), the symmetry-allowed ground state rotation is disrotatory; such rotation bring methyl groups close to closing ring. This steric hindrance will block the ground state reaction. In the excited state, the symmetry allowed rotation is conrotatory. Such conrotatory motion moves away the two methyl groups from closing the ring and do not disturb the reaction.

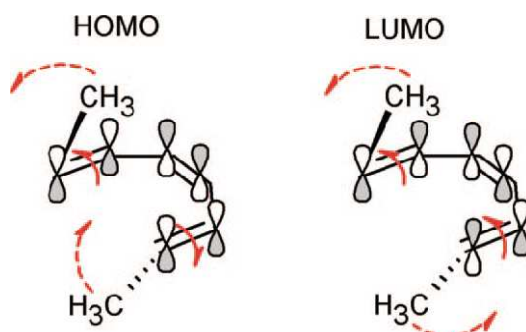


Figure.4.10: Antiparallel open form: HOMO-no bond formation, LUMO-bond formation

Chapter 4. Molecules on Epitaxial graphene

In parallel open form, disrotatory rotation in the ground state does not lead to steric hindrance however in the excited state conrotatory rotation brings one of the methyl groups close to closing the ring which blocks the cyclization reaction.

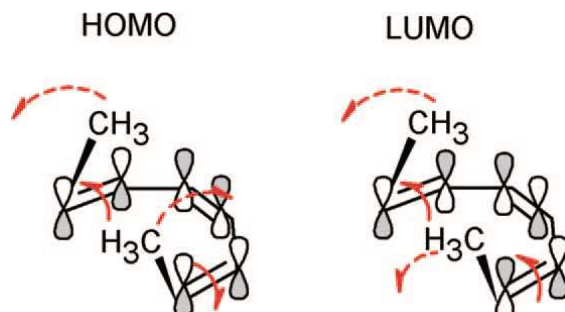


Figure.4.11: parallel open form: HOMO- bond formation, LUMO- no bond formation .

The first deposition was carried out with a commercially available diarylethene (TCI Europe, 1,2-bis(2-methylbenzothiophene-3-yl)-3,3,4,4,5,5-hexafluoro-1-cyclopentene) on pristine graphene. The molecules were evaporated at 125°C ($I_c = 9\text{ A}$, with I_c is the current for heating the crucible,) during 3 min ($P_{\text{sas}} = 7.7 \cdot 10^{-6}\text{ mb}$) with the sample at room temperature. But we could not observe anything on the surface as the STM images were blurred and unstable.

Therefore, we have deposited TBT-diarylethene-TBT with ethylhexyloxy side chains (Figure.4.12 and 4.13) synthesized by F. Calard from the Group of Montpellier on pristine graphene.

4.2.2. TBT-diarylethene-TBT (FC62) molecules

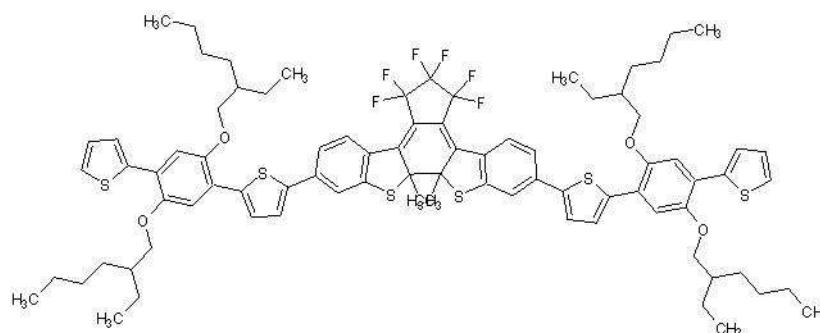


Figure.4.12: Scheme of the TBT-diarylethene-TBT with ethylhexyloxy side chains.

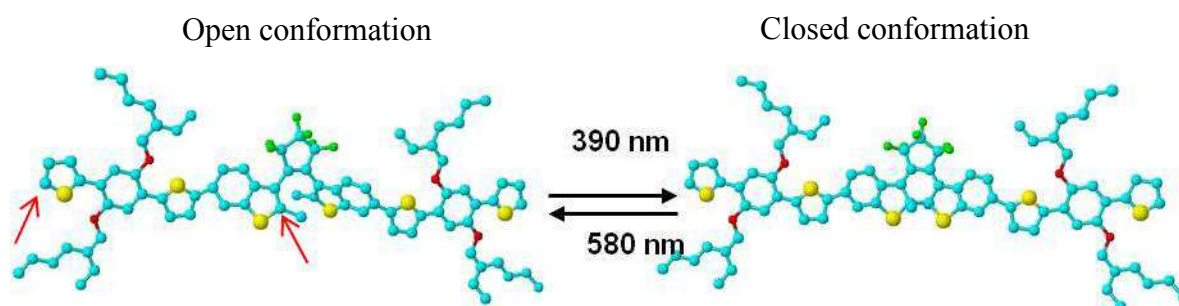


Figure.4.13: Scheme of the TBT-diaryl-TBT with ethylhexyloxy side chains. The F atoms are displayed in green, the O atoms in red, the S atoms in yellow and the C atoms in blue.

The physical parameters of the molecules in its open and closed conformations are summarized in the Table 4.1

Parameters	Open conformation	Closed conformation
Width	16Å	16Å
Length	36Å	36Å
Thickness	4Å	4Å
C-C distance from a TBT to one side of diaryl shown by red arrows	17Å	17Å

Table 4.1: The physical parameters of molecules in open and closed conformations

Chapter 4. Molecules on Epitaxial graphene

The “thickness” of the molecule is the distance between the two CH₃ groups of the diarylethene core. In both conformations, where all thiophene and benzene rings of the TBT units are on the same plane due to the intramolecular interactions between S and O atoms [175].

The FC62 molecules were deposited by evaporation at 215°C on two graphene samples during 3 minutes where the samples held at room temperature. In one sample, FC62 molecules form small islands that are mobile under the STM tip. It was not possible to get stable STM images. But the other sample we were able to get a few images. The FC62 molecules (green colour powder) synthesized from Montpellier composed of open (47% in anti-parallel; 23% in parallel) and closed (30%) conformations. This is revealed from their absorption, fluorescence and NMR characterizations, all made in solutions (either n-hexane, CHCl₃ or CDCl₃). However, during evaporation and deposition on the surface, the molecules can change its conformation.

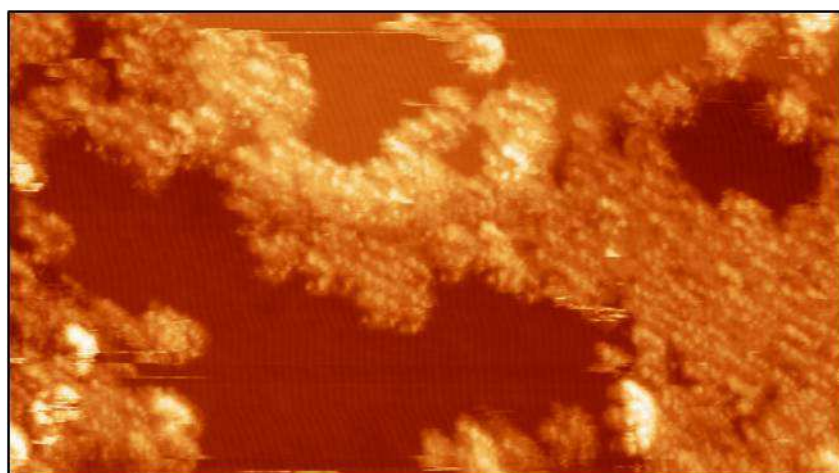


Figure. 4.14: STM topographic image of FC62 molecules on epitaxial graphene (100×56nm², 2.7V).

From Figure.4.14, it is clear that the molecules self-assemble on the surface, forming a 3D island of molecules that is spread over two different terraces of the substrate. The height difference between the two terraces is 2.55 Å (see the corresponding height profile, Figure 4.5 c) which corresponds to the SiC bilayer spacing. Then the molecular

Chapter 4. Molecules on Epitaxial graphene

layer continuously adsorbs on the same graphene sheet over the SiC step edges. The molecules adsorb preferentially at the edges of the terrace, as they are fully decorated by the molecules. Also we observe that the density of molecules is higher on the lower terrace of the substrate than on the upper terrace. This is due to a molecular diffusion from the center of the terrace towards the step edges, thus elongating the molecular island towards the center of the terrace.

The height profile measurements were performed to obtain information on the adsorption behavior of the molecules on the surface. From these height profile measurements, it can be seen that the molecules are forming 3D islands, with a minimum height of $1.85 \pm 0.2 \text{ \AA}$. This distance is much smaller than the width of a molecule and quite near from the “thickness” of the molecule. So the molecules cannot adsorb perpendicularly or tilted on the surface. They are laying flat on the surface.

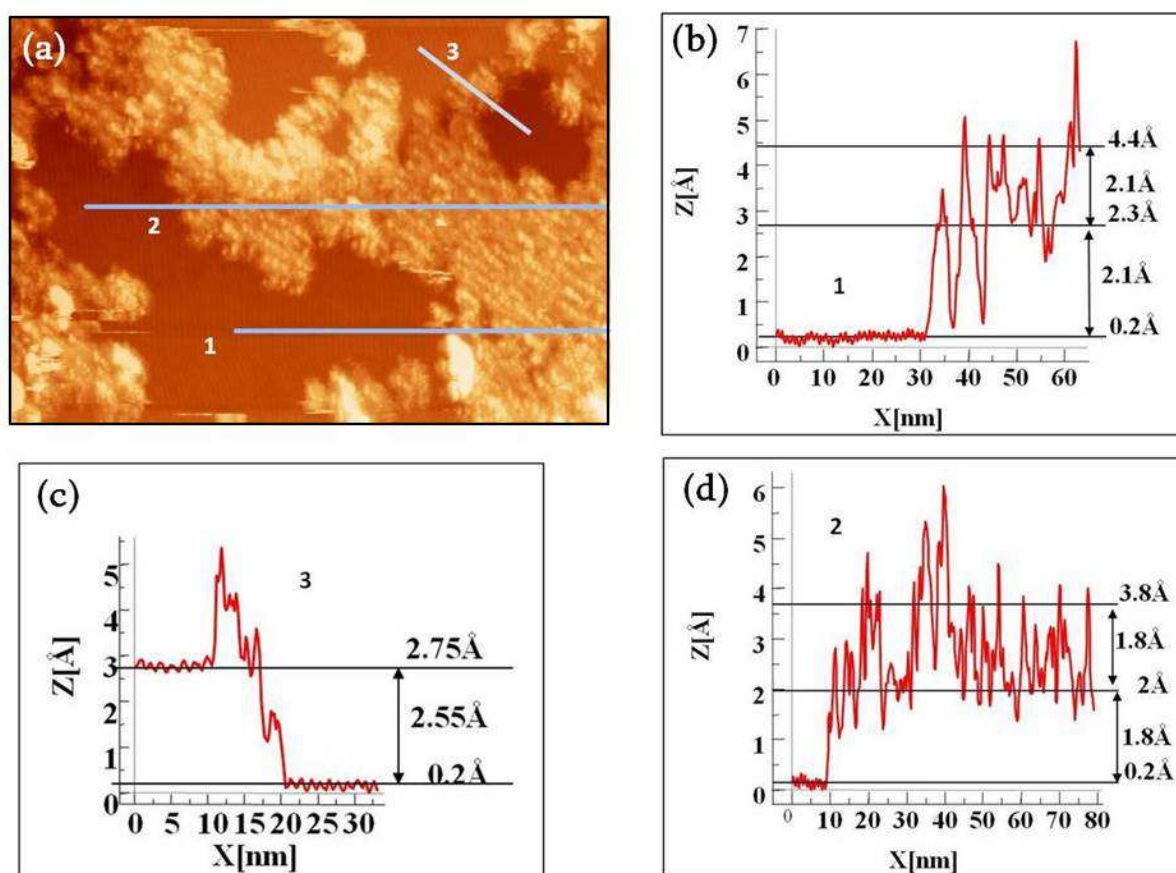


Figure.4.15: a) STM topographic image of FC62 on pristine graphene ($100 \times 61 \text{ nm}^2$, 2.7V) (b-d) corresponding height profile measurements.

Chapter 4. Molecules on Epitaxial graphene

The islands are 3D as there is a second partial layer on top of this first layer with again a minimum height of $1.84 \pm 0.2 \text{ \AA}$ (and even a third with only few isolated molecules, the brighter ones on the STM images). It seems that the island starts to grow vertically before covering the whole surface of graphene. This leads us to assume that the intermolecular interactions are stronger than the interactions between the molecules and the graphene substrate.

By using a self-correlation filter on different STM images, the average distance between the molecular lines is $\sim 2.3 \pm 0.5 \text{ nm}$, which is quite near to the width of a molecule. By checking carefully inside the molecular lines, we can see that the molecules are usually discontinuous. It is possible to recognize on different areas and on different images, the two different features on the surfaces that are probably related to the different conformations of the molecules (Figure.4.16).

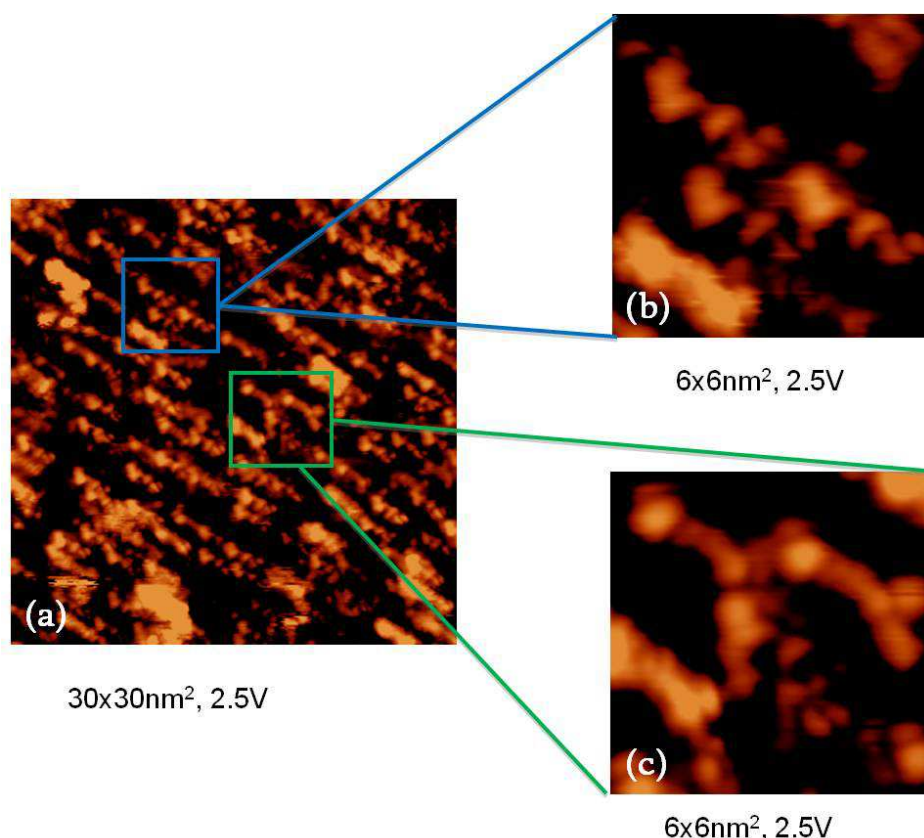


Figure.4.16: (a) STM topographic image of FC62 molecules (b) and (c) show the zoom of (a) where two different features are observed.

Chapter 4. Molecules on Epitaxial graphene

Figure 4.17 shows the zoom of two different features which are observed within the molecular islands. One consists of a bright dot, a comma-shaped dot and two small dots. The other feature has a Y shape made of two small dots with a bright dot at one end. The measured size of this repeated unit is $\approx 1.85 \pm 0.1$ nm. These features correspond to the different conformations of molecules.

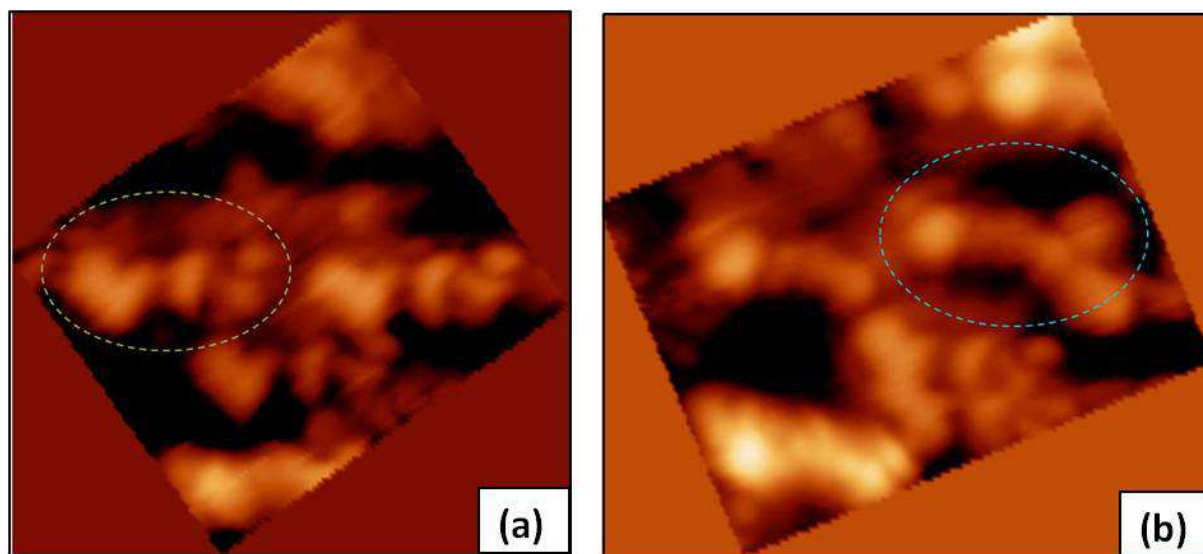


Figure.4.17: STM topographic image of FC62 molecules (a) ($5.5 \times 5 \text{ nm}^2$, 2.5V) and (b) ($7 \times 5.3 \text{ nm}^2$, 2.5V) show the zoom of observed two different features within the molecular islands.

Figure 4.18 shows the average distance between the two bright dots and between the two small dots. It is clear that these distances are same and this distance corresponds to the length of a molecule. Therefore it is difficult to place the molecule on the exact position in the STM image. It is also not possible to identify which conformation we are dealing with and interpret these features.

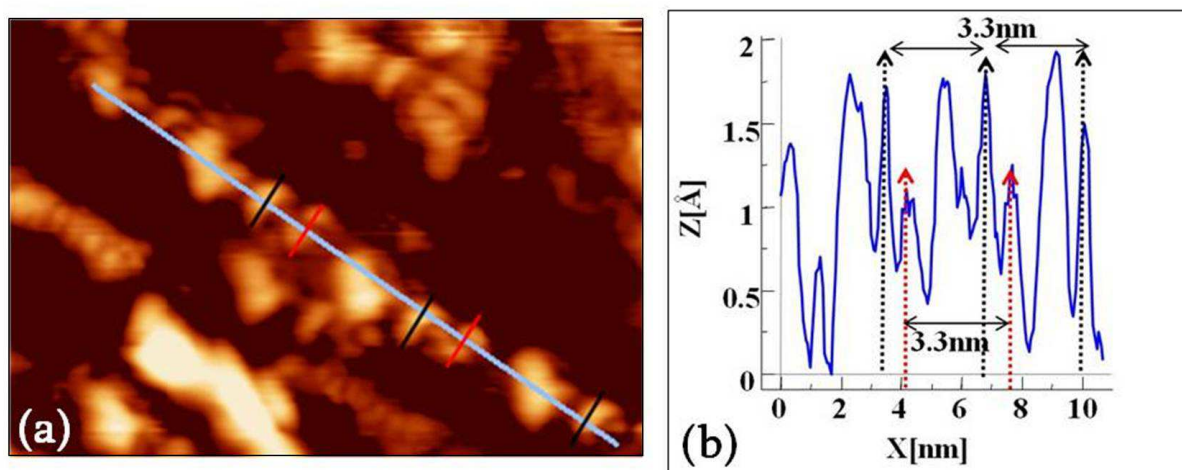


Figure.4.18: (a) STM topographic image of FC62 molecules ($10 \times 7 \text{ nm}^2$, 2.3V) (b) corresponding line profile showing distance between two bright dots and two small dots are same.

To conclude, TBT-Diaryl-TBT with ethylhexyloxy side chains (FC62) seem to self-assemble on epitaxial graphene on SiC(0001) in the form of 3D islands. The imaged island continuously extends over the SiC step edges and its growth has started from the step edges towards the centre of the terrace. From the height profile measurements of this island, it is clear that the molecules lay flat on the surface. The molecular island is composed of one complete molecular layer, a second partial layer and some isolated molecules on top of it. This tends to assume that the intermolecular interactions are stronger than the interactions between the molecules and the graphene substrate.

The molecules are quite well ordered in the center of the island compared to those at the borders. They are forming quite discontinuous molecular lines, oriented along one preferential direction. The average distance between the molecular lines is 2.3 ± 0.5 nm, which corresponds to the width of a molecule.

It was possible to distinguish two periodic features inside the molecular lines. Most of them consist of a bright dot, a comma-shaped dot and two small dots. The distance between two bright dots is 3.3 ± 0.1 nm which corresponds to the length of the molecule.

Chapter 4. Molecules on Epitaxial graphene

The other feature has a Y shape made of small dots with a bright dot at one end and the distance between two bright dots is 3.0 ± 0.1 nm.

4.3. Conclusion

This chapter mainly deals with the deposition of two types of molecules; TTFm and FC62 (TBT-diaryl-TBT with ethylhexyloxy side chains). In the first part of this chapter, the depositions of TTFm molecules on pristine graphene and gold intercalated graphene in UHV, and in phenyl octane solvent on graphite at ambient conditions, were discussed. On pristine graphene and gold intercalated graphene in UHV, TTFm molecules follow edge-on conformation while on liquid/graphite interface the molecules are laying flat on the surface and follow the hexagonal structure of graphite. The difference in conformation of molecules can be attributed to the solvent effect or strong molecule- substrate interaction as in the case of graphite or may be due to the imaging conditions. It will be interesting to study the deposition of TTFm molecules on graphite in UHV to make a comparison and to solve this problem.

In the second part, we discussed the deposition of FC62 molecules on epitaxial graphene in UHV. The molecules formed as 3D islands thus to enhance the molecule-molecule interaction than the molecule-substrate interaction. However the observed two periodic features correspond to two different conformations of molecules within the molecular islands, cannot interpret successfully. Also it was difficult to obtain a complete self assembled layer of molecules on epitaxial graphene in UHV. Therefore, it will be interesting to try on other substrates such as on HOPG [176,177] or on Au (111) [178, 179], or in liquid STM experiments. The presence of two different conformations can be the reason for the disorder in self-assembly. Hence it will be thought-provoking to try a deposition using liquid injection valve then after irradiate the solution (for example using a Na lamp (589 nm)) in order to get almost only one conformation of the molecule on the substrate.

Abstract: Chapter 5. Photophysical properties of molecules

Abstract: Chapter 5. Photophysical properties of molecules

Dans ce chapitre nous présentons une étude photophysique relative à différents chromophores utilisés dans le cadre de la thèse. La première étude aborde les propriétés électroniques d'une série d'oligophénylèneéthiénylène de longueurs croissantes (une à quatre unités moléculaires). A partir de calculs théoriques (DFT et TDDFT) couplés à une large gamme de techniques spectroscopiques (absorption et fluorescence stationnaire ; fluorescence résolue en temps, effets de température, anisotropie d'émission, fluorescence induite à deux photons), des relations structures/propriétés électroniques ont été établies. Le bathochromisme associé à l'augmentation de la longueur de conjugaison a été rationalisé par le modèle classique de la particule dans une boîte 1D. D'autre part, il a été montré, pour ces dérivés, que la configuration électronique quinoïdale domine l'état excité émissif conduisant à une planarisation photoinduite des oligomères. Ces chromophores pouvant jouer le rôle de relais 'électroniques' présentent également des sections efficaces d'absorption à deux photons très intéressantes avec une valeur maximale de 750 GM pour le plus grand oligomère. La seconde étude concerne les propriétés photochromiques d'un dérivé éthiénylperfluorocyclopentène intégrant des oligothiophènes en périphérie de structure. La commutation photoinduite entre formes ouvertes et fermées a été évaluée en solution conduisant respectivement à des rendements quantiques de 0.11 et 0.04 en milieu apolaire. De plus, cette photochromie est très dépendante de la polarité du milieu et diminue considérablement en milieu polaire. Ces photoreactions sont beaucoup moins efficaces que celles observées pour le photochrome modèle dû à un abaissement de l'énergie de l'état singulet. Enfin, il a été montré que la forme ouverte était fluorescente ($\Phi_f = 0.28$) ceci en cohérence avec la faible efficacité à la fermeture du photochrome. Cette étude photophysique met l'accent sur les compromis à trouver entre efficacité de réactions photochromiques et longueurs de conjugaison des fragments moléculaires d'oligothiophènes.

Chapter 5. Photophysical properties of molecules

5. Photophysical properties of molecules

This chapter deals with the study of photophysical properties of different molecules. In the previous chapter, we have seen the self organization process of photochromic molecules with conjugated (FC62) on epitaxial graphene. As the FC62 molecules consists of a diarylethene molecule connected to two oligothiophene, we first start with the photophysical study of oligothiophene molecules and these measurements will be compared to FC62. Oligothiophene (TBT) molecules were synthesized by the team of Prof. F. Serein-Spirau, Montpellier in the framework of ANR Transfilsen.

5.1. Photophysical properties of an oligothiophene series

This part is devoted to the study of the structure/properties relationship of a linear oligo(phenylenethienylene) series whose length is gradually increased from 1 to 4 repeating units. These organic-based- π -conjugated molecules are of considerable current interest because of their semi-conducting and light emitting properties. Oligothiophenes can be used as a versatile molecular platforms [180], or building block motifs [181] to enhance the degree of electronic delocalization within a molecular architecture which allows the rationalization of optoelectronic properties. Moreover, this molecular engineering strategy is totally equivalent to that developed to create new organic chromophores with large two-photon absorption (2PA) cross sections [182]. 2PA materials are of great importance for a wide range of new emerging technologies including optical limiting [183-184], 3D-optical storage memory [185-186], photodynamic therapy [187] and stereolithography [188-192]. It has been demonstrated that a series of macrocyclic thiophene n -mers integrating more than twelve thienylene patterns which exhibit giant 2PA cross sections (δ) up to 11×10^5 G (1 GM = 10^{50} cm⁴ s photon⁻¹) [193]. A similar building method has been applied to insert several thiophene rings into hexaphyrin and octaphyrin derivatives which induced a very impressive

Chapter 5. Photophysical properties of molecules

increase of two photon absorption cross section δ [194]. Therefore it is clear that by increasing the length of conjugated chains could result in a strong enhancement of δ .

The optoelectronic properties of the conjugated oligomers vary significantly with HOMO-LUMO gap. This gap depends on the degree of extended conjugation which, in turn, should depend on the level of planarity of the molecules. Indeed a more planar system leads to a better π - π orbital overlap which promotes the lowering of the HOMO level and therefore the decrease of HOMO-LUMO gap. Therefore, the structural or geometrical properties of the conjugated molecules in their ground state and excited states are important to understand to address such fundamental issues.

This section is organized in the following way: The first part discusses the ground state properties of oligo(phenylenethienylene)s series using UV-Visible absorption spectroscopy, free electron model and Time Dependent-Density Functional Theory (TD-DFT). The second part deals with the excited states properties using low temperature absorption and fluorescence spectra. Then the third part concerns the two photon absorption (2PA) properties of these π -conjugated molecules.

5.1.1 Ground state properties of an Oligo (phenylenethienylene) s series

The ground state properties of oligo (phenylenethienylene)s series were investigated by employing UV-Visible absorption spectroscopy, free electron model and Time dependent-Density Functional Theory (TD-DFT). The scheme of oligo (phenylenethienylene)s series or generally called oligothiophenes (TBT) are shown in Figure 5.1. The repeating unit consists of a regioregular alternated sequence of 2, 2'-bis-thiophene and 2, 5-dialkoxybenzene moieties. These molecules are conjugated molecules where π -electrons are delocalized along the chain. The oligomers exhibit very good solubility in common organic solvents due to the

Chapter 5. Photophysical properties of molecules

alkoxy side chains. They display a planar geometry due to non-covalent intramolecular sulphur-oxygen interactions.

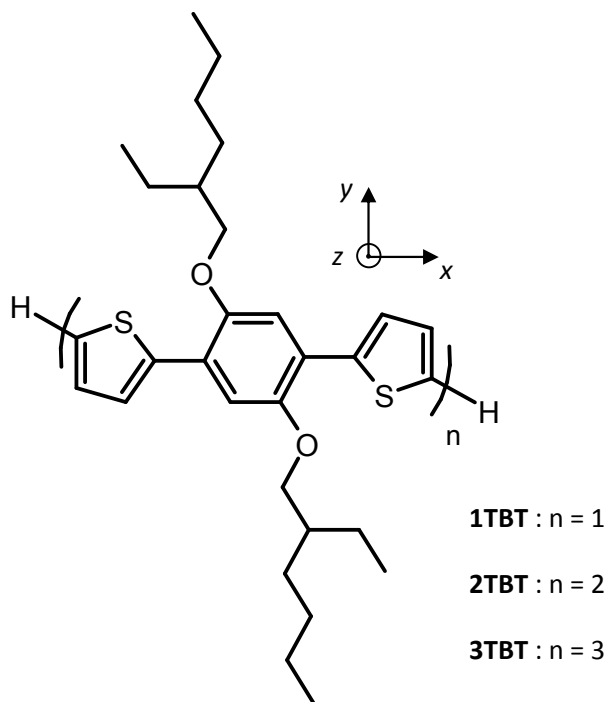


Figure.5.1: The scheme of molecular structure of oligothiophenes (nTBT) where the index “n” stands for number of TBTs.

5.1.1.1. UV-Visible absorption spectroscopy

The UV-Visible absorption spectroscopy measurements were carried out with a Perkin Elmer Lambda 2 spectrometer. The brief of this technique is explained in chapter 2. Figure below shows the absorption spectra of oligomers in n-butylacetate (BUA) solvent and the inset shows the plot of the maximum absorption wave number versus $1/n$ for nTBT in BUA. Table 1 gathers the corresponding spectroscopic data.

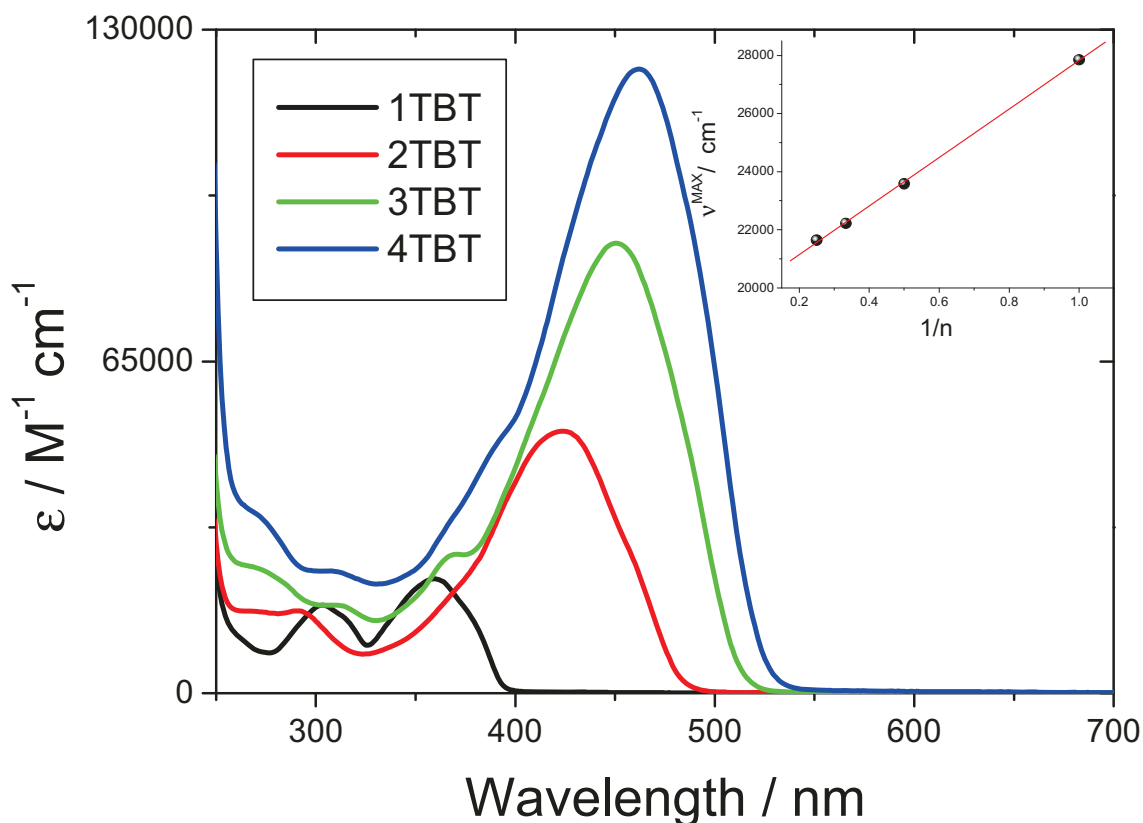


Figure.5.2: The UV-Visible absorption spectra of the oligomers in n-butylacetate (BUA).

	λ_{abs} / nm	ϵ^{MAX} / $\text{M}^{-1} \text{cm}^{-1}$	FWHM / cm^{-1}	M_{ge} / D
1TBT	359	22400	4060	5.5
2TBT	424	51300	4520	9.5
3TBT	450	88200	4555	12.9
4TBT	462	122300	4595	15.4

Table 1: Summary of optical data and calculated parameters for nTBT in BUA

From the Figure 5.2. it is clear that, for each TBT, the low energy side of the spectrum is dominated by an unstructured band which clearly shifts to the red region and increases in intensity by increasing the length of the molecular structure. The absorption band shifts by about 6210cm^{-1} and undergoes a 5.5-fold enhancement in intensity when going from 1TBT to

Chapter 5. Photophysical properties of molecules

4TBT. The mainly dominated absorption band is due to a single electronic transition (i.e. from S_0 to S_1). The broad nature (large Full width half maximum, FWHM) of the absorption band is due to the large population of rotational isomers in its ground state. The large increase of molar absorption coefficients (ϵ) with increasing number of TBTs confirm the nature of strongly allowed conjugated core π - π^* transition (see Table 1). The inset in Figure 5.2 shows a plot of the energies relative to the first absorption maxima versus reciprocal of the number of repeating units (n). The position of maximum absorption (λ_{max}) indicates HOMO-LUMO energy gap. As the conjugation increases (by increasing number of TBTs), HOMO-LUMO gap decreases, consequently an increase of red shift (lower energy). This plot is well in connection with particle in box model [195-197].

5.1.1.2. Particle in a box model

For conjugated molecules it is well known that the singlet energy gap scales inversely with the number of repeat units, which is reproduced very elegantly by Kuhn's simple one electron model [195]. In this model, the π -electrons are considered as one-dimensional free-electron gas which extends itself along the length of the chain. In normal state, the more stable energy states of the electron gas contain two electrons in accordance with Pauli's exclusion principle. If N is the number of π -electrons in the conjugated chain, then for the ground state, each of $N/2$ levels contains two electrons and the remaining levels are empty. The first absorption band is a consequence of the jump of π -electron from highest energy level occupied in the normal state to the lowest empty level.

For the wavelength of the maximum of the first absorption band, the relationship obtains that

$$\lambda_1 = \left(\frac{8mc}{h}\right) \left(\frac{L^2}{[N+1]}\right) \quad (\text{Eq.5.1})$$

Chapter 5. Photophysical properties of molecules

where L is the length of the conjugated chain, N is the number of π -electrons, c , the velocity of light and h is the plank's universal constant. Therefore, the well correlated straight line of absorption maximum (inset of Figure.5.2) confirms that excited state corresponding to the lowest energy band is characterized by an extensive π -conjugation throughout the entire oligomer.

5.1.1.3. Excitation Anisotropy spectra

The occurrence of electronic transitions (S_0 - S_1 or S_0 - S_n) can be further verified by excitation anisotropy spectra. The experimental technique is explained elsewhere [105].

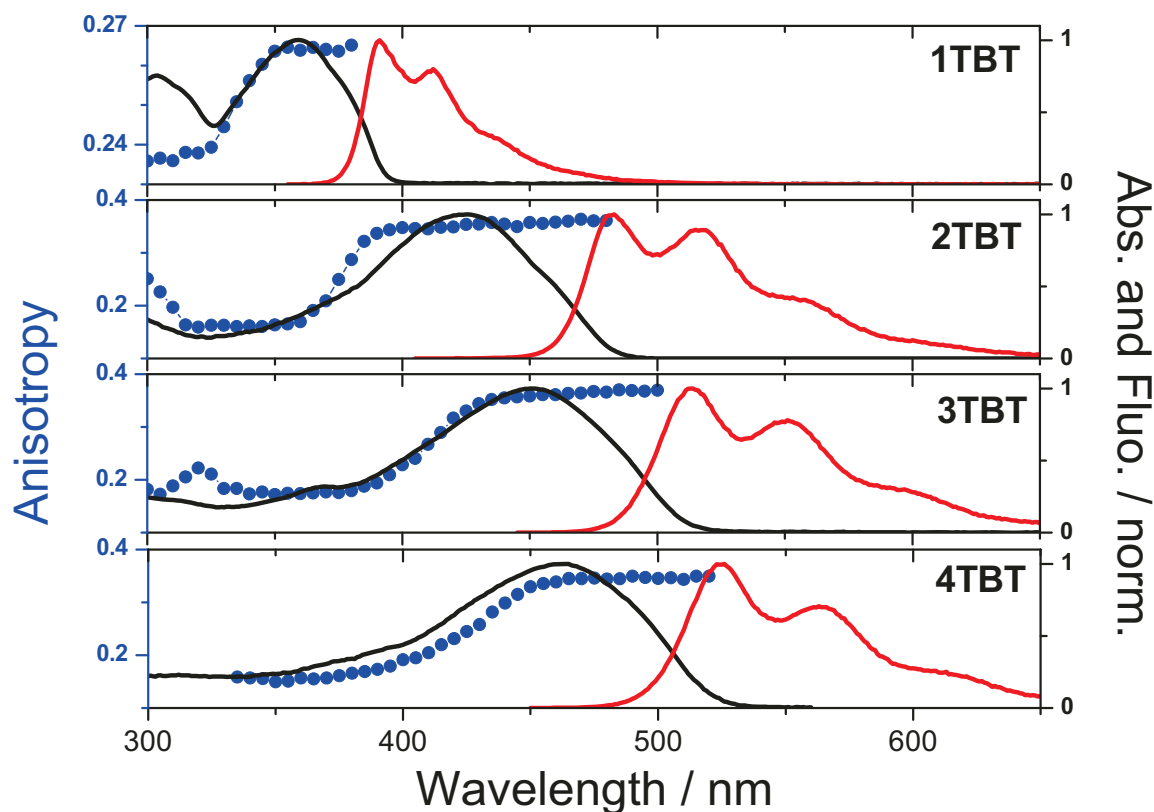


Figure.5.3: Normalized absorption and fluorescence spectra of nTBT in triacetin and Excitation anisotropy spectra (blue circles) of nTBT in triacetin are also shown.

Chapter 5. Photophysical properties of molecules

From the anisotropy spectra (blue circles in Figure.5.3), the anisotropy of all oligomers remains constant in the spectral region of longest wavelength absorption band. The average anisotropy values recorded in this spectral region are close to the theoretical upper limit (i.e. 0.4) which suggests that both absorption and emission transition moments are oriented in the same direction, presumably that of the longest molecular axis (x -axis in Figure 5.1). This is the clear indication of mainly dominated absorption band is due to the single electronic transition S_0-S_1 . Then the anisotropy decreases and reaches another plateau at the blue edge of the absorption band where a slight shoulder located which emphasizes the presence of other S_0-S_n transitions with distinctive electronic symmetries with respect to that of the S_0-S_1 one. For 1TBT, a well separated band is clearly observed at the high energy side of the longest wavelength absorption band.

5.1.1.4. Time dependent-Density Functional Theory (TD-DFT) calculations

All the electronic transitions (S_0-S_1 or S_0-S_n) of the oligomers can be further evidenced using TD-DFT calculations based on the fully optimized geometries obtained at DFT level. In first step, the ground-state geometry of all structures was optimized without any constraint with the PBE0 functional along with the 6-31G(d) basis set. (Note that PBE0 is a good functional for the description of photofunctional molecules [198] and a large system as 4TBT has restricted the choice of an extended basis set). Harmonic vibrational wavenumbers were checked to confirm the convergence to the minimum on the potential energy surface. In second step, the first low-lying excited states were calculated using the vertical TD-DFT calculation with the same basis set. Figure 5.4 shows the fully-optimized geometry of 3TBT along with contours of the frontier orbitals. For all the oligomers, each minimum-energy geometry exhibits a transoid conformation with inter-ring angles ranging from 20° to 23° between dialkoxyphenylene and thiophene groups and from 10° to 12° between two adjacent thiophenes. Extending the π -delocalization by increasing the length of the chromophore does not induce a significant planarization of the structure. In addition, such calculated

Chapter 5. Photophysical properties of molecules

trans-distorted geometries generally deviate from planarity with much larger magnitude as those observed experimentally in solid state. This structural discrepancy should be ascribed to the solid-state packing effects which lead to a substantial reduction of twist angles [199-200].

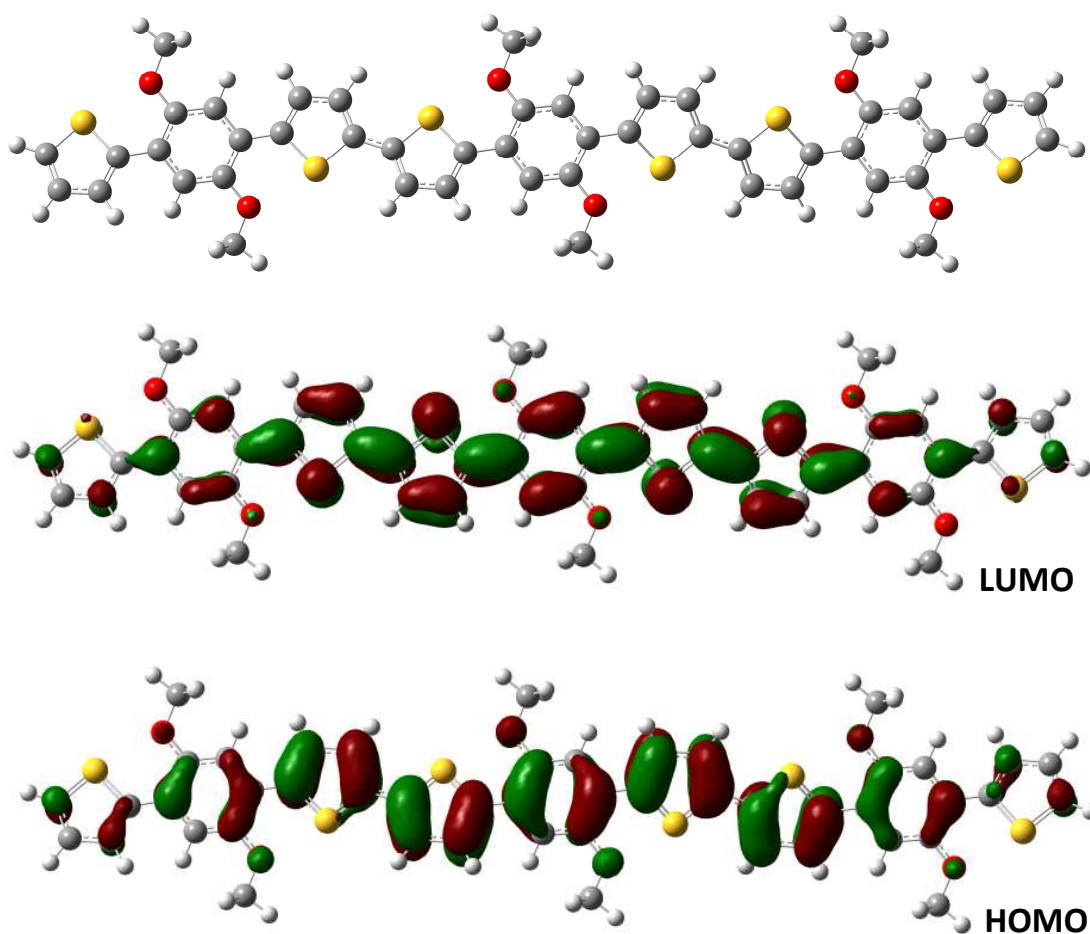


Figure.5.4: Fully optimized geometries of 3TBT obtained at DFT levels and corresponding frontier orbitals optimized at the PBE0/6-31G (d) level [Calculation done by Stephane Aloise, UST, Lille]

Chapter 5. Photophysical properties of molecules

Table 2 are reported the calculated energies of the electronic transitions with their corresponding oscillator strengths and the main orientation. In Figure 5.4 are depicted the electronic contours of the frontier orbitals for 3TBT.

	1TBT				2TBT				3TBT				4TBT			
	Exp.		Theoretical		Exp.		Theoretical		Exp.		Theoretical		Exp.		Theoretical	
	E_{00} /eV	E_{th} /eV	f	Pol. ^a	E_{00} /eV	E_{th} /eV	f	Pol. ^a	E_{00} /eV	E_{th} /eV	f	Pol. ^a	E_{00} /eV	E_{th} /eV	f	Pol. ^a
$S_0 \rightarrow S_1$	3.19	3.43	0.89	\underline{x}, y^b	2.56	2.66	2.11	x	2.39	2.41	3.24	x	2.33	2.31	4.39	x
$S_0 \rightarrow S_2$		4.20	0.23	x, \underline{y}^b		3.28	0.0002	\underline{y}, z^b		2.85	0.0030	z		2.61	0.02	y, \underline{z}^b
$S_0 \rightarrow S_3$		4.58	0	$-^c$		3.42	0.0006	y, \underline{z}^b		2.98	0.0001	z		2.81	0.03	\underline{x}, z^b
$S_0 \rightarrow S_4$		4.78	0	$-^c$		3.74	0.03	\underline{x}, y^b		3.25	0.18	x		2.93	0.62	x
$S_0 \rightarrow S_5$		4.98	0.71	\underline{y}, z		3.94	0.23	x		3.33	0.39	x		3.05	0.04	\underline{x}, y^b

^a see Figure 5.1 for the orientation

Table 2: TD-DFT and experimental electronic transitions of nTBT

For all derivatives, the calculations indicate that the S_0 - S_1 transition is mainly a HOMO-LUMO transition with high oscillator strength and a symmetrical charge delocalization along the x -axis (see Figure 5.1) which corresponds to the phenylene-thienylene segment as shown in Figure 5.4. It should be noted that all TBTs are centrosymmetric molecules which belong to C_{2h} symmetry group. In this case, the calculations indicate that the $S_0 \rightarrow S_1$ transition should be assigned to the $1A_g \rightarrow 1B_u$ transition which implies two electronic states with alternating symmetry with respect to the centre of inversion of the molecule. This transition is one-photon allowed but two-photon forbidden as will be explained using two photon absorption spectroscopy. It is noteworthy that, for 2 to 4 TBT, $S_0 \rightarrow S_1$ transition dipole moment is mainly collinear to the oligomer long axis (x -axis) as previously suggested by the high values of anisotropy. For 1TBT, the length-to-width ratio of the molecule is drastically reduced as compared to the other oligomers. As a consequence, the polarization of the $S_0 \rightarrow S_1$ transition includes a significant component in the y -direction due to a much extended charge delocalization along the 2,5 dialkoxyphenylene moiety. The lower anisotropy recorded for 1TBT (i.e. 0.26 ± 0.1) should therefore denote a slight change in the orientation of the electronic polarization between absorption and

Chapter 5. Photophysical properties of molecules

emission assuming that the transition dipole at emission maintains its orientation parallel to the x -axis (see Figure 5.1). For 2-4 TBT, the $S_0 \rightarrow S_2$ and $S_0 \rightarrow S_3$ transitions have extremely low oscillator strength (f). They involve mixed contributions from (HOMO-1)–LUMO and HOMO–(LUMO+1) transitions and are mainly polarized in a direction perpendicular to that of the $S_0 \rightarrow S_1$ one. Those transitions which imply electronic states with the same symmetry should be assigned to the $1A_g \rightarrow nA_g$ transitions. Such a change in the electronic symmetry as compared to that of the $1A_g \rightarrow 1B_u$ transition should explain the large decrease in the anisotropy signal observed at the blue edge of the lowest energy band. Interestingly, for 1TBT, the $S_0 \rightarrow S_2$ transition which exhibits a noticeable f could not be assigned to a pure $1A_g \rightarrow 2A_g$ transition but presumably to a weighted mixing of the $1A_g \rightarrow 2B_u$ and $1A_g \rightarrow 2A_g$ transitions.

Hence, from quantum-chemical calculations two important conclusions can be drawn. All thiophene-based oligomers adopt a trans-distorted conformation with low inter-ring torsion angles at ground state. The two lowest-energy transitions exhibit distinctive electronic symmetries: a strongly allowed $1A_g \rightarrow 1B_u$ one which is mainly oriented along the aromatic segment and a weakly allowed $1A_g \rightarrow 2A_g$ transition with a transition dipole moment perpendicular to the long axis of the chromophore.

The HOMO-LUMO gap relates linearly to the cosine of interring twist angle, as expected when orbital energies are proportional to the degree of orbital overlap, which is proportional to the cosine of the angle between the orbitals. As $\cos \theta = 1$, at an interring twist angle of zero (i.e. in a planar system), there is maximum overlap of molecular orbitals. Therefore the planar oligothiophenes are expected to display smaller HOMO-LUMO gap than their twisted counterparts owing to a better orbital overlap in the planar configuration. Therefore it is important to understand to what extent the bending influences the oligothiophene properties such as HOMO-LUMO gaps.

Chapter 5. Photophysical properties of molecules

5.1.2 Fluorescence properties of nTBT. Dependence on Solvent and Temperature.

The photophysical parameters of the nTBT series in various solvents of increasing polarity are reported in Table 3.

	λ_{abs} / nm	λ_{fluo} / nm	Δv_{st} / cm^{-1}	Φ_{fluo}	τ_{fluo} / ns	k_r / 10^9 s^{-1}	k_{nr} / 10^9 s^{-1}	M_f / D	$\frac{k_r}{k_f^{SB}}$
1TBT									
HEX	355	<u>388</u> , 409	2396	0.16	0.52	0.31	1.62	4.5	0.82
BUA	359	<u>391</u> , 412	2280	0.21	0.56	0.37	1.41	5.0	
THF	361	<u>392</u> , 413	2191	0.22	0.57	0.39	1.37	5.2	
DMF	363	<u>395</u> , 414	2232	0.23	0.61	0.38	1.26	5.1	
2TBT									
HEX	418	<u>478</u> , 511	3003	0.38	0.72	0.53	0.86	8.1	0.76
BUA	424	<u>482</u> , 517	2838	0.40	0.73	0.55	0.82	8.3	
THF	425	<u>484</u> , 519	2868	0.37	0.73	0.51	0.86	8.1	
DMF	431	<u>489</u> , 522	2752	0.40	0.72	0.56	0.83	8.6	
3TBT									
HEX	445	<u>507</u> , 544	2748	0.33	0.61	0.54	1.10	8.9	0.50
BUA	451	<u>513</u> , 551	2680	0.39	0.71	0.55	0.86	9.2	
THF	452	<u>515</u> , 553	2706	0.37	0.72	0.51	0.88	8.9	
DMF	459	<u>522</u> , 559	2629	0.36	0.73	0.49	0.88	8.9	
4TBT									
HEX	454	<u>519</u> , 554	2759	0.37	0.61	0.61	1.04	9.8	0.46
BUA	462	<u>524</u> , 563	2561	0.47	0.69	0.68	0.77	10.5	
THF	465	<u>527</u> , 567	2530	0.45	0.68	0.66	0.81	10.4	
DMF	469	<u>534</u> , 571	2595	0.47	0.73	0.64	0.72	10.5	

Table 3 : Spectroscopic data of nTBT in various solvents

As expected, all molecules are poorly solvatochromic. On going from apolar (hexane) to highly polar solvents (DMF), the bathochromic shifts corresponding to the absorption and fluorescence bands do not exceed 700 cm^{-1} . Such slight spectral effects confirm the very weak dipole moments for both ground and excited states. There is also a relatively weak influence of the solvent on the fluorescence quantum yield (Φ_f) whose value abruptly increases on going from 1TBT to the other derivatives. This effect is similar to that observed for α -oligothiophenes [201] where Φ_f increases quasi-monotonically up to six thiophenes and then remains stable. The increase in emissivity with the number of repeating units should be related to the progressive stabilization of the relaxed S_1 level within the singlet and triplet

Chapter 5. Photophysical properties of molecules

manifolds [201-204]. Hence, the competing nonradiative deactivation processes such as intersystem-crossing are reduced. The decrease of the nonradiative rate constants (k_{nr}) on going from 1TBT to the other derivatives is in agreement with the proposed mechanism. Interestingly, the incremental addition of repeating units leads to an increasing trend of the radiative rate constants (k_r) whose average value is about $0.36 \pm 0.04 \text{ ns}^{-1}$ for 1TBT and reaches a value of $0.65 \pm 0.03 \text{ ns}^{-1}$ for 4TBT. This moderate increase of k_r indicates a slight change in the electronic configuration of the emissive state certainly due to the extension of the emissive segment over one repeating unit.

Figure 5.5 shows the normalized absorption and fluorescence spectra of the oligomers in 2-MTHF at 293 K (solution) and 77 K (glassy matrix).

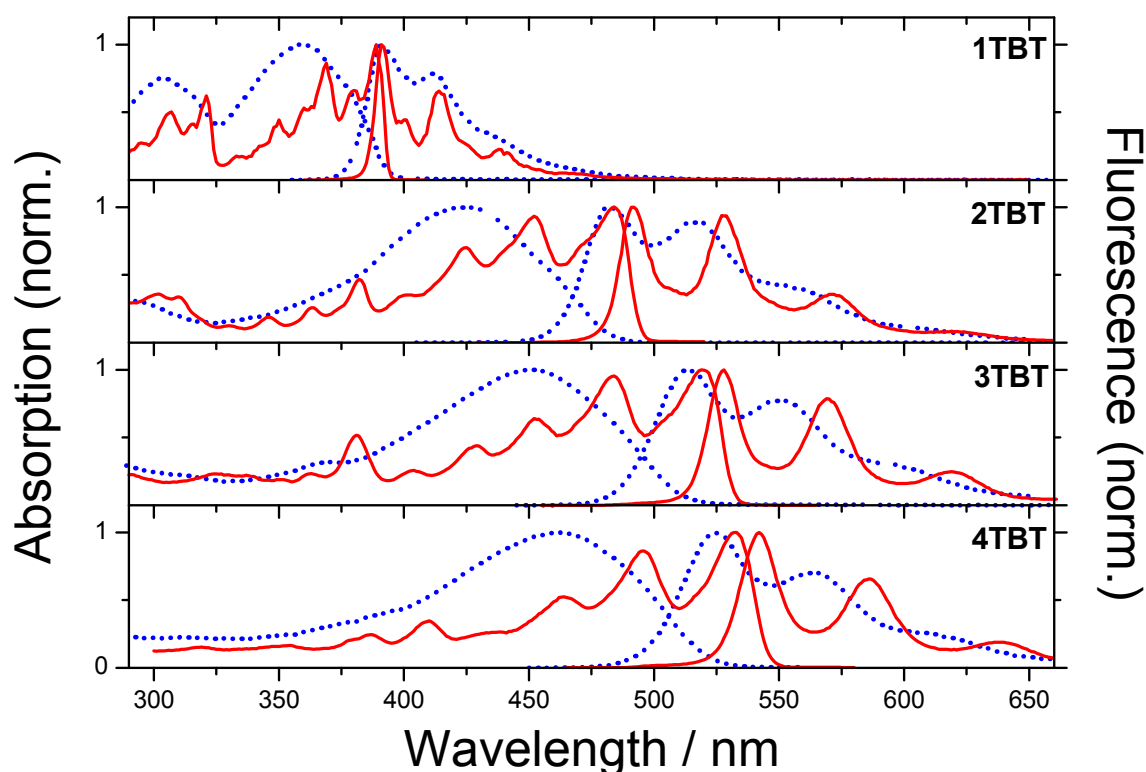


Figure.5.5: shows the normalized absorption and fluorescence spectra at room temperature (dotted blue lines) and in glassy matrix at 77K (solid red lines) for nTBT in 2-MTHF.

Chapter 5. Photophysical properties of molecules

At room temperature, one clearly observes a complete breakdown of the mirror symmetry rule for all compounds since the $S_0 \rightarrow S_1$ absorption band which is devoid of any fine structure contrasts to the well-defined vibronic progression observed in the fluorescence spectrum. The splitting periodicity of each emission band is in the 1400-1500 cm^{-1} range which should be assigned to one of the $\nu(\text{C}=\text{C})$ stretching vibrational modes of the bithiophene sequence in the conjugated segment [201,205-206]. Such a spectral feature should be ascribed to a photoinduced conformational change between the ground and the first excited state. Indeed for oligothiophene derivatives, it has been demonstrated [207] that even though the fully planar geometry corresponds to an absolute minimum energy, the torsional barriers relative to inter-ring rotations are relatively low at ground state ($< 1\text{-}2 \text{ kcal mol}^{-1}$) [ref 7-60 PCCP]. The population of distorted conformations becomes possible at room temperature. The average conformation then induces the broadening and the shift of the $S_0 \rightarrow S_1$ absorption band to higher energy. Upon excitation, these flexible oligomers undergo a fast geometrical relaxation process dominated by a collective twisting of the aromatic rings towards the fully planar structure. For instance, Lanzani *et al.* [206] showed that the characteristic time constant relative to the inter-ring torsional relaxation was about 4 ps for the quaterthiophene. In glassy matrix of 2-MTHF (77K), all inter-ring rotations are strongly hampered which prevents any conformers inter-conversion. As a consequence, the mirror image relationship between absorption and emission spectra is restored (see Figure 5.5) and associated with a drastic decrease of the Stokes shift as compared to that observed at room temperature.

It should be stressed that, even though the incremental addition of repeating units leads to a gradual increase of the torsional degrees of freedom, the fluorescence decays recorded in solution clearly remain monoexponential at all monitoring wavelengths and do not contain any contribution of long-lived components that could stem from distinctive populations of emitting conformers. This is a clear indication that all excited nTBT relax to a

Chapter 5. Photophysical properties of molecules

very stable configuration. The excited-state should indeed exhibit a strong quinoid character [201,208-209] which leads to a rigid structure with a high degree of coplanarity. Moreover, the amplitude of geometrical changes between the average conformation at ground state and the planar structure at equilibrium excited state can be evaluated by comparison of the radiative rate constant (k_r) with the Strickler-Berg rate constant k^{SB} calculated from equation 5.2.[210] :

$$k_f^{SB} = \frac{64\pi^4}{3h} n^3 \nu_f^3 M_{ge}^2 \quad (\text{Eq.5.2})$$

where n , h , ν_f and M_{ge} correspond respectively to the refractive index of the solvent, the Planck constant, the maximum fluorescence wavenumber and the transition moment relative to the electronic transition from the ground (g) to the non-relaxed S_1 state (e). This transition dipole moment can be calculated according to the expression [211-212]:

$$M_{ge}^2 = \frac{3hc10^3 \ln 10}{8\pi^3 N_A n} \int \epsilon(\nu_a) d(\ln \nu_a) \quad (\text{Eq.5.3})$$

N_A is Avogadro's number and $\epsilon(\nu_a)$ corresponds to the molar extinction coefficient of the $S_0 \rightarrow S_1$ band at wavenumber ν_a . Moreover for this calculation, we assume that the overall absorption band is due to a single electronic transition as suggested by the excitation anisotropy spectrum. The values of M_{ge} calculated in n-butylacetate for all oligomers are reported in Table 1. Note that these experimental values are nicely correlated ($R^2 > 0.992$) with the corresponding oscillator strengths relative to the vertical $S_0 \rightarrow S_1$ transitions (see Table 2). In the same manner, the fluorescence electronic transition dipole moment, M_f , can be derived from the radiative rate ($k_r = \Phi_f/\tau_f$) according to the equation 5.4 [213]:

$$k_r = \frac{64\pi^4}{3h} n^3 \nu_f^3 M_f^2 \quad (\text{Eq.5.4})$$

Chapter 5. Photophysical properties of molecules

The calculated values of M_f in various solvents are gathered in Table 3. As previously observed, no solvent induced effect is detected since M_f remains insensitive to the nature of the solvent. According to equations 5.2 and 5.4, it should be noted that the ratio between k_r and k^{SB} leads to that of the squared M_f and M_{ge} . Hence, if no change of the electronic or molecular geometry occurs at S_1 state, a ratio of unity should be obtained. However, as shown in Table 3, a progressive deviation from unity is observed when increasing the size of the oligomer. This gradual deviation from unity denotes that the excited-state dynamics inducing the planarization process involves a growing number of interannular torsional modes due the increase of repeating units.

5.1.3. Two-photon absorption (2PA) measurements

The concept of the two-photon absorption (2PA) process was first proposed by M.Goppert-Mayer in 1931 in her doctoral dissertation. 2PA involves a simultaneous absorption of two photons lead to a transition between a lower and higher energy level of an atom or molecule. Extending the charge delocalization along a π -conjugated relay strongly impacts the 2PA cross-section of the chromophore. Therefore 2PA spectroscopy can be used here as a relevant probe to investigate the structure/electronic properties relationships of our oligomers. The 2PA cross sections were measured by 2PA induced fluorescence method using a femtosecond pulsed laser as excitation source. The brief detail of this technique is explained in chapter 2. Figure 5.7 shows the one and two-photon absorption spectra of oligomers in n-butylacetate. Table 4 gathers the 2PA data of all derivatives.

	λ_{abs} / nm	λ_{2PA} / nm	δ / GM
1TBT	359	700	2 ± 1
2TBT	424	720	112 ± 22
3TBT	450	760	500 ± 100
4TBT	462	770	802 ± 160

Table 4: 2PA properties for nTBT in BUA

Chapter 5. Photophysical properties of molecules

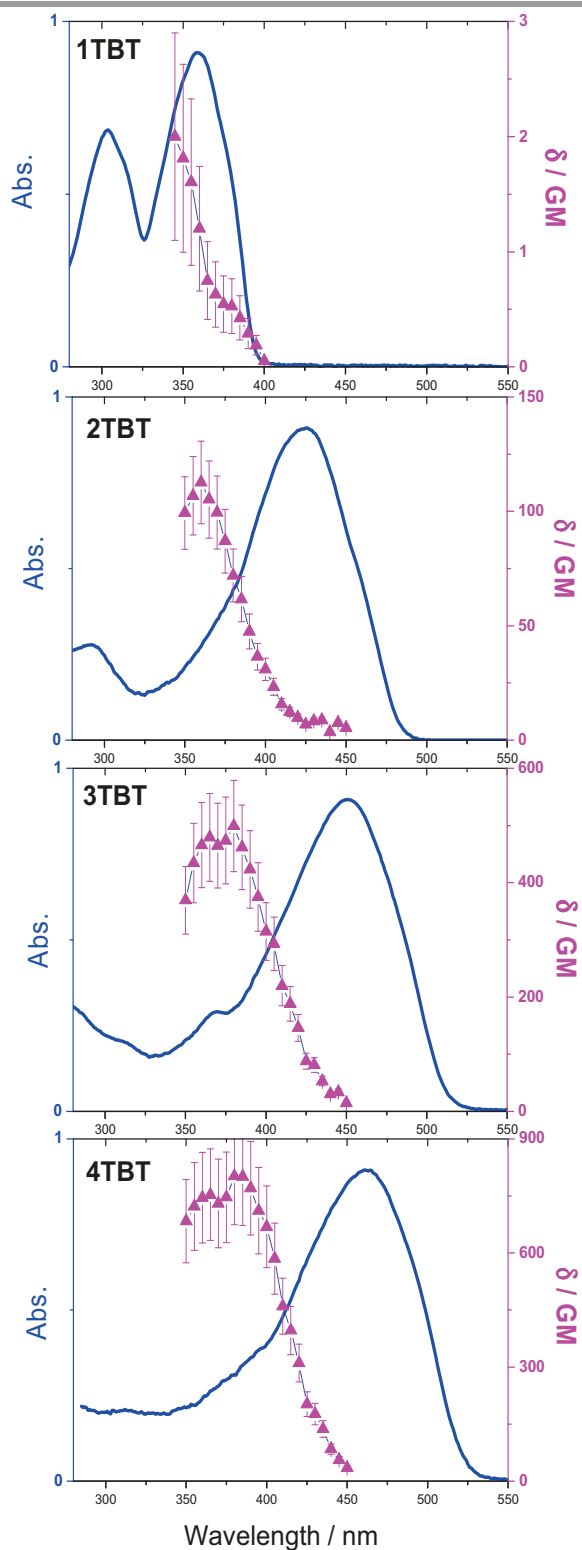


Figure.5.7: One (blue solid line) and two photon (pink triangle) absorption spectra of nTBt in Butyl Acetate.

Chapter 5. Photophysical properties of molecules

The 2PA spectra are plotted against half the excitation wavelength to allow a direct comparison with the one-photon absorption spectra. For centrosymmetric chromophores, the two-photon excitation from S_0 state to the lowest excited state S_1 (i.e. the $1A_g \rightarrow 1B_u$ transition) is forbidden according to dipole selection rules. Therefore, one can clearly observe that the main 2PA peak does not coincide with the one-photon absorption maximum. This 2PA peak corresponds to the two-photon excitation from S_0 to S_2 states (i.e. $1A_g \rightarrow 2A_g$). However, 2PA spectrum of 1TBT shows a weak long wavelength band in the spectral region corresponding to the $S_0 \rightarrow S_1$ transition. This indicates a symmetry breaking in the parity selection rules probably due to a vibronic coupling between S_1 and S_2 levels as it was previously observed for small centrosymmetric molecules such as fluorene-based chromophores [214-215]. By increasing the length of the oligomer, the position of 2PA peaks slightly shifts to the low energy region from 700 nm to 770 nm ($\sim 1300 \text{ cm}^{-1}$) whereas the two-photon absorption maximum (δ) increases drastically in range of two orders of magnitude from $2 \pm 1 \text{ GM}$ for 1TBT up to 802 ± 160 for 4TBT. Moreover δ increases almost linearly with the number of repeating units with no saturation effect as illustrated in Figure 5.8.

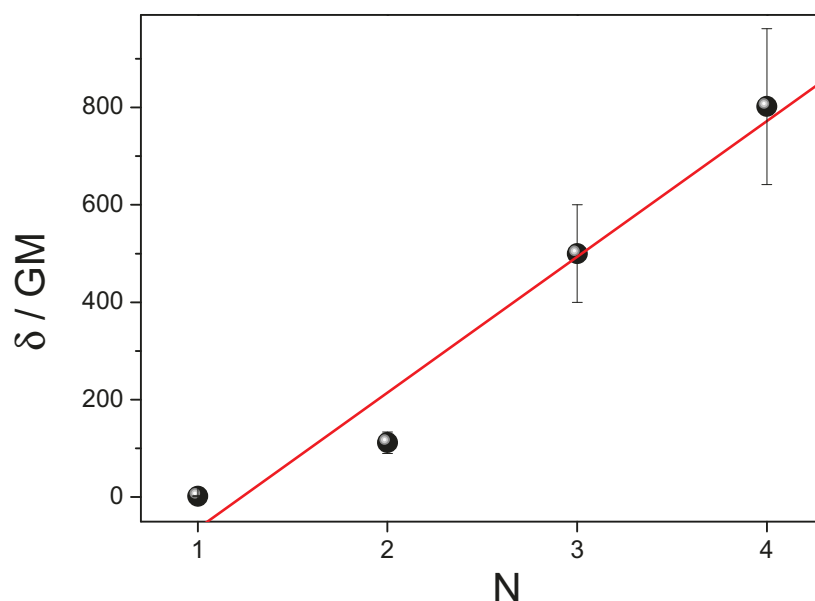


Figure 5.8: Two photon absorption cross section values as a function of number of repeating units in Butyl Acetate (BUA).

Chapter 5. Photophysical properties of molecules

This feature is consistent with the fact that the magnitude of the two-photon absorption cross section is associated with the effective π -conjugation length which corresponds to the distance over which the charges are delocalized.

5.1.4. Conclusion

The structural properties of an oligo(phenylenethienylene)s series were investigated in detail using linear and two-photon absorption spectroscopy. The ground states properties of the molecules are evidenced by UV-Visible absorption spectroscopy, free electron model and Time dependent-Density Functional Theory (TD-DFT). The broad nature of absorption spectra at room temperature reveals the large population of rotational isomers in its ground states. This is further confirmed from the absence of mirror image relationship between absorption and fluorescence spectra at room temperature which ascertains a strong change of the inter-ring torsional flexibility between ground and emitting states. While at low temperature the inter-ring-rotations are freezed and thus the mirror relationship is preserved. Indeed, in excited state, the oligomer undergoes a severe structure rigidification irrespective to the oligomer size which leads to a relaxed S_1 state with a planar quinoidal-like geometry evidenced from fluorescence measurements. Furthermore, the structural or geometrical changes between the ground state (average conformation) and excited state (planar structure) are evaluated by Strickler-Berg rate constant k^{SB}

The incremental addition of conjugated repeating units induces a bathochromic shift of the absorption band which is well predicted in the frame of the particle in a box model. The excitation anisotropy spectra and TDDFT calculations indicate that the longest wavelength absorption band is dominated by a strongly dipole-allowed electronic transition (i.e. $1A_g \rightarrow 1B_u$) or S_0-S_1 , which is mainly polarized in a direction parallel to the longest axis of the oligomer and implies a charge delocalization all over the aromatic rings. This also indicates the presence of a weakly allowed transition located at the blue edge of the main

Chapter 5. Photophysical properties of molecules

absorption band which was assigned to the $1A_g \rightarrow 2A_g$ transition. According to the dipole selection rules for centrosymmetric molecules, this latter transition is two-photon allowed as opposed to the S_0-S_1 one. Thus the centrosymmetric nature of these molecules is revealed.

Moreover, the two-photon absorption properties of the oligomers have been measured in connection with the growing size of the derivatives. The dimension has a strong influence on the two-photon absorption cross section since δ drastically increases from 2 ± 1 GM for 1TBT to 802 ± 160 GM for 4TBT.

5.2. Photophysical properties of TBT-Switch-TBT (FC62)

To understand the effect of conjugation with photochromic molecules, we have studied the absorption and fluorescence spectroscopy of FC62 and compared with that of 1TBT.

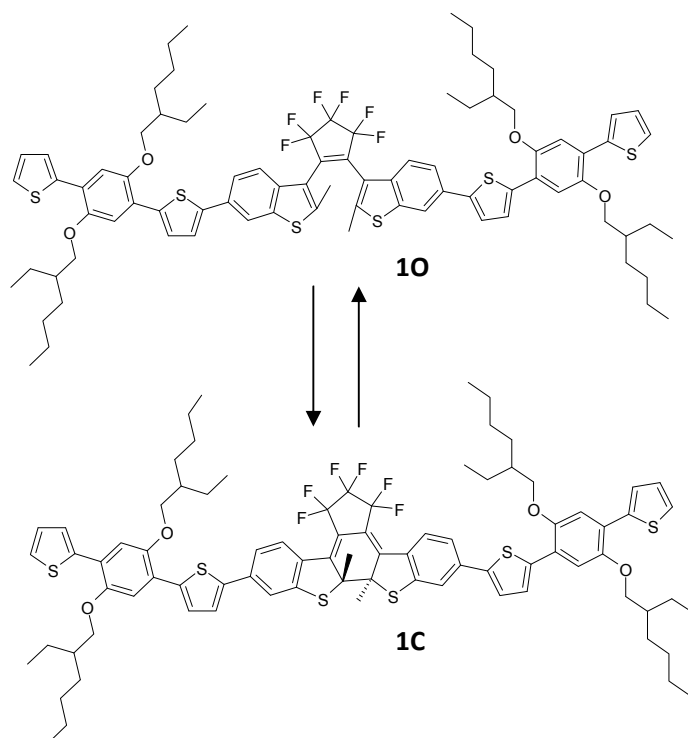


Figure.5.9: Scheme of FC62 molecules in its open and closed conformation

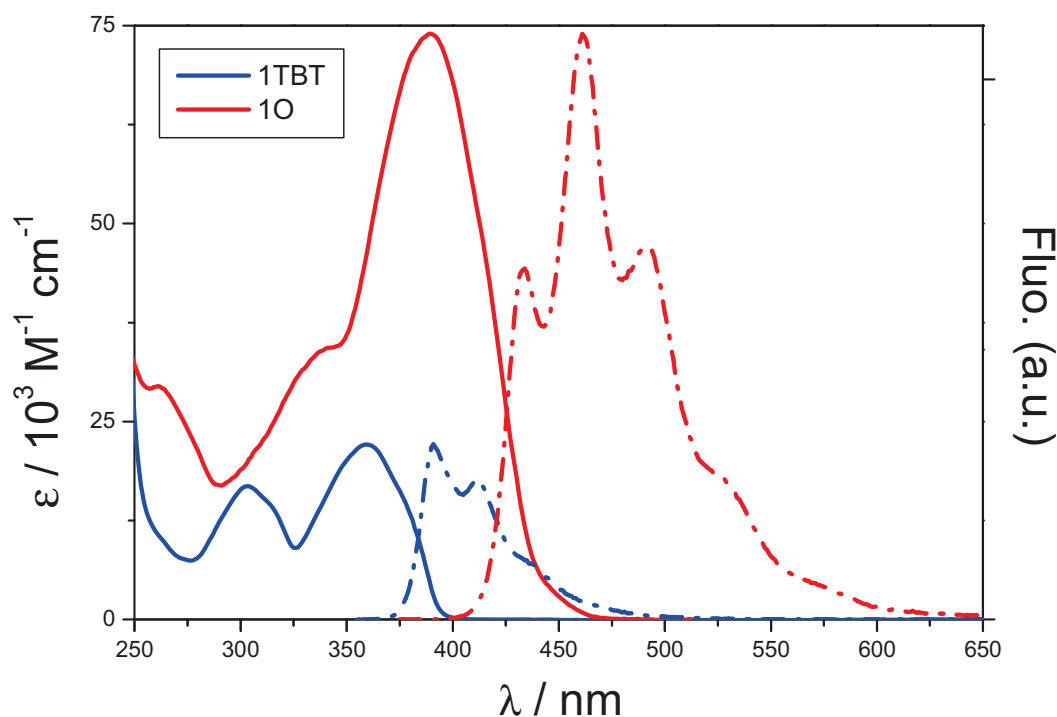


Figure 5.10: Absorption and fluorescence spectra of the compounds (FC62 and 1TBT) in hexane.

Figure 5.10 shows the absorption and fluorescence spectra of 1O (open conformation) and 1TBT. The latter compound corresponds to the external part of the arms of the photochromic system. The low energy side of the absorption spectrum of 1O is dominated by an intensive band with a maximum located at 390 nm and a ϵ_{\max} of $73980 \text{ M}^{-1} \text{ cm}^{-1}$. A distinctive shoulder at 337 nm is also observed at the blue edge of this band. The longest wavelength absorption band of 1TBT is clearly blue shifted with respect to that of 1O and its maximum extinction coefficient (i.e. $22100 \text{ M}^{-1} \text{ cm}^{-1}$) is much lower than half ϵ_{\max} of 1O. These important differences with the spectral feature of the model chromophore should be ascribed to a more extended electronic delocalization that should include the benzothiophenyl group. This assumption is also confirmed when comparing the fluorescence spectra of both dyes in hexane (Figure 5.10). It clearly appears that both structured emission bands do not match together. The fluorescence spectrum of 1O is strongly shifted to the red

Chapter 5. Photophysical properties of molecules

region by about 4000 cm^{-1} as compared to 1TBT. Moreover, contrary to 1TBT, the maximum fluorescence intensity of 1O is located on the 0,1 vibronic band. According to the Franck-Condon principle, this effect should be assigned to a significant structural distortion on going for ground state to excited one [105].

Hex	λ_{abs} / nm	λ_{fluo} / nm	Φ_f	τ_f / ns	Φ_r
1O	390	433, <u>462</u> , 493	0.28	0.71	0.11
1C	575	-	-	-	0.04

Table 5: Spectroscopic data of 1O (open conformation) and 1C (closed conformation) in hexane (apolar).

The main spectroscopic and photochromic data of 1O and 1C are gathered in Table 5, and their spectral changes are shown in Figure 5.11.

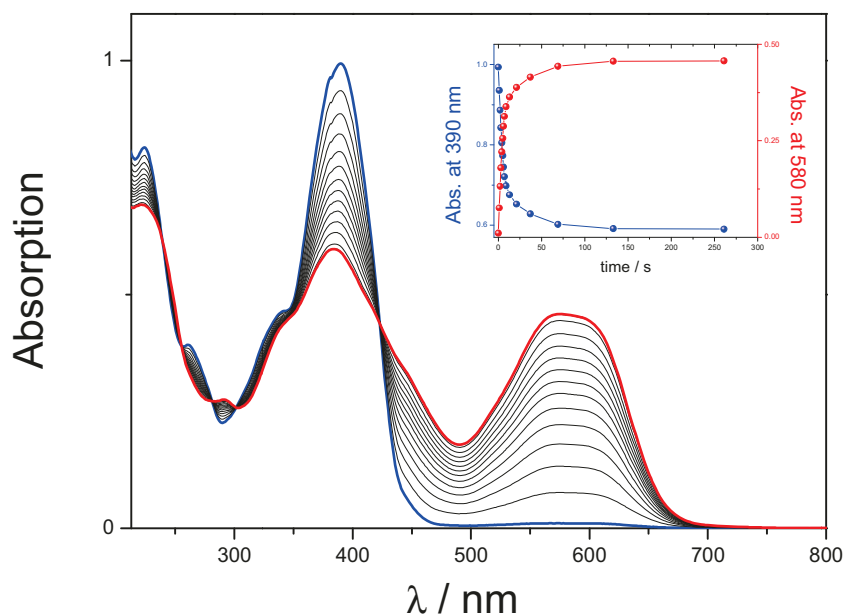


Figure 5.11: Evolution of the absorption of 1O in hexane ($c: 1.33 \times 10^{-5}\text{ M}$) upon irradiation at 365 nm ($P_{365\text{ nm}}: 12\text{ mW}$). Inset: Absorption time dependent relations at 390 nm and 580 nm.

Chapter 5. Photophysical properties of molecules

In apolar medium, the cyclization quantum yield (0.11) is three times lower than that of the bis(1-benzothiophen-3-yl) hexafluorocyclopentene (BTCP) which corresponds to the exact photochromic core of our TBT-based system [172]. The decrease of the cyclization efficiency has been previously observed for thiophene substituted derivatives when going from the monomer to oligomer substituents. It was then proposed that substituent electron donating ability as well as the large extension of the π -conjugation along the branches which leads to a decrease of excited singlet energy were responsible for the decrease of the reaction quantum yield. This substituent effect affects all the more the backward reaction since the ring-opening quantum yield is divided by a factor 9 as compared to that of BTCP.

5.3. Conclusion

In conclusion, the photophysical properties of (oligo(phenylenethienylene)s) conjugated molecules and (FC62) photochromic molecules were investigated. In the first part, the structural properties of oligo(phenylenethienylene)s were studied using one and two photon absorption spectra. From these studies we found that the molecules are centrosymmetric and can undergo different conformations. In ground state, there is a large population of rotational isomers but in excited state the oligomer undergoes a severe structure rigidification irrespective to the oligomer size which leads to a relaxed S_1 state with a planar quinoidal-like geometry. It is also clear that by increasing the length of conjugation, the electrons are delocalized along the molecular line evidenced by a red shift in absorption band. A bathochromic shift of absorption band is observed in FC62 (open conformation) compared to 1TBT. This is due to a more extended electronic delocalization that should include the benzothiophenyl group in FC62.

Summary

We have explored the possibilities to realize a Graphene Based Hybrid structures (GBHs) by the functionalization of a graphene layer on both sides.

After the introduction chapter 1 and the description of the experimental techniques used in this work (chapter 2), in chapter 3, we have studied the epitaxial graphene on SiC(0001) and focused on its functionalization using metals. We have evidenced and characterized by Scanning Tunneling Microscopy (STM) and Spectroscopy (STS) that the gold deposition following by annealing leads to the intercalation of gold atoms between the top graphene layer and the buffer layer bonded to the substrate. Several types of intercalation process has been evidenced in this work, the formation of aggregates of individual gold atoms (DP), the formation of a continuous gold layer for which a p-type doping was evidenced by STS measurements and two other phases showing different structures. “The free standing nature” of the intercalated gold atoms was examined by differential charge density plot and projected density of states (PDOS) calculations. This was further investigated by X-ray photoelectron spectroscopy (XPS). Moreover, with the help of calculated STM images we came to the conclusion that gold atoms are intercalated as isolated individual atoms. We have studied in detail how these gold atoms modified the band structure of graphene. Previously observed standing wave pattern on DP for the bias voltage corresponding to unoccupied states from +0.7 to +1eV where interpreted as an extension of the Van Hove singularities using Fourier Transform Scanning Tunneling Spectroscopy (FT-STs) which has been confirmed by Angle-resolved photoemission spectroscopy (ARPES). ARPES measurements revealed also a mass renormalization around the Dirac point and an increase of the Fermi velocity (up to 20%), which has been attributed to the modification of the hopping potential due to the decoupling of the graphene layer from the buffer layer. This was supported by roughness analysis of graphene. This band structure modification has been discussed in the framework of the superconductivity following the theory developed for the Graphite intercalation compounds.

Summary

In the following of these studies, the goal was to strongly dope the graphene in order to put the Fermi level at the Van Hove singularities. For that we have studied the functionalization of graphene by depositing electron donor molecules (chapter 4). We deposited highly electron donor molecules, TetraThiofullvalene (TTF) on pristine and gold intercalated graphene. We have studied the conformation of these molecules in their self-organization process and their ability to transfer a charge to the graphene layer. Unlike previous studies done mainly using liquid STM and graphite surface, we have evidenced an edge-on conformation, which hinder the charge transfer to the graphene layer. However two conformations, laying flat and edge-on, have been observed in the same supramolecular layer. These conformations are the results of a subtle balance between the interdigitation of the lateral alkyl chain and the molecule-substrate interaction. This balance was illustrated by the strong modification of the self-assembling process observed by comparing pristine and gold intercalated graphene substrate. In the last part of this chapter we presented preliminary results of the reactivity of graphene with photochromic molecules along with the conjugated one.

In the last chapter 5, structural properties of conjugated molecules and photochromic molecules along with the conjugated one were studied using photophysical measurements.

References

References:

1. K. S. Novoselov, A. K. Geim, S. V. Morozov, D. Jiang, Y. Zhang, S. V. Dubonos, I.V. Grigorieva, A. A. Firsov, *Science* **306**, 666 (2004).
2. P. R. Wallace, *Phys. Rev.* **71**, 622 (1947).
3. G. W. Semenoff, *Phys. Rev. Lett.* **53**, 2449 (1984).
4. D. P. Divincenzo and E. J. Mele, *Phys. Rev. B* **29**, 1685 (1984).
5. A. K. Geim, and K. S. Novoselov, *Nat. Mater.* **6**, 183 (2007).
6. A. H. Castro Neto, F. Guinea, N. M. R. Peres, K. S. Novoselov, and A. K. Geim, *Rev. Mod. Phys* **81**, 109 (2009).
7. Eva Y Andrei , Guohong Li and Xu Du, *Rep. prog. Phys.* **75**, 056501 (2012).
8. K. S. Novoselov, S. V. Morozov, T. M. G. Mohinddin, L. A. Ponomarenko, D. C. Elias, R. Yang, I. I. Barbolina, P. Blake, T. J. Booth, D. Jiang, J. Giesbers, E. W. Hill, and A. K. Geim, *Phys. stat. sol (b)* **244**, 4106 (2007).
9. A.M.J. Schakel, *Phys. Rev. D* **43**, 1428 (1991).
10. Katsnelson, M.I. Zitterbewegung, *Eur. Phys. J. B* **51**, 157 (2006).
11. M. I. Katsnelson, K.S. Novoselov, A.K. Geim, *Nat. Physics* **2**, 620 (2006).
12. J. Tworzydło, B. Trauzettel, M. Titov, A. Rycerz, and C.W.J. Beenakker, *Phys. Rev. Lett.* **96**, 246802 (2006).
13. L. Jiao, L. Zang, X. Wang, G. Diankov, and H. Dai, *Nature* **458**, 877 (2009).
14. D.V. Kosynkin, A.L. Higginbotham, A. Sinitskii, J.R. Lomeda, A. Dimiev, B.K. Price and J. M. Tour, *Nature* **458**, 872 (2009).
15. Y. Hernandez, V. Nicolosi, M. Lotya, F. M. Blighe, Z. Sun, S. De, I. T. McGovern, B. Holland, M. Byrne, Y.K Gun'ko, J. J. Boland, P. Niraj, G.Duesberg, S. Krishnamurthy, R. Goodhue, J.Hutchison, V.Scardaci, A.C. Ferrari, J. N. Coleman, *Nat. Nanotech* **3** (9), 563 (2008).
16. A. K. Geim, *Science* **324**,1530 (2009).
17. C. Gómez-Navarro, J. C. Meyer, R. S. Sundaram, A. Chuvilin, S. Kurasch, M. Burghard, K. Kern, and U. Kaiser, *Nano Lett.* **10**, 1144 (2010).

References

18. S. Stankovich, D. A. Dikin, R. D. Piner, K.A. Kohlhaas, A. Kleinhammes, Y. Jia, Y. Wu, S. T. Nguyen, R. S. Ruoff, *Carbon* **45**, 1558 (2007).
19. C. Oshima and A. Nagashima, *J. Phys.: Condens. Matter* **9**, 004 (1997).
20. J. Wintterlin and M.L. Bocquet, *Surf. Sci.* **603**, 1841 (2009).
21. N. A. Kholin, E. V. Rut'kov, and A. Y. Tontegode, *Surf. Sci.* **139**, 155 (1984).
22. E. V. Rut'kov, and A. Y. Tontegode, *Surf. Sci.* **161**, 373 (1985).
23. A. N'Diaye, J. Coraux, T. Plasa, C. Busse, T. Michely, *New J. Phys.* **10**, 043033 (2008).
24. I. Pletikosić, M. Kralj, P. Pervan, R. Brako, J. Coraux, A. T. N'Diaye, C. Busse, and T. Michely, *Phys. Rev. Lett.* **102**, 056808 (2009).
25. S.-Y. Kwon, C. V. Ciobanu, V. Petrova, V. B. Shenoy, J. Bareno, V. Gambin, I. Petrov, S. Kodambaka, , *Nano Lett.* **9**, 3985 (2009).
26. A. B. Preobrajenski, M. L. Ng, A. S. Vinogradov, and N. Mårtensson, *Phys. Rev. B* **78**, 073401 (2008).
27. H. Zi-pu, D.F. Ogletree, M.A. van Hove, and G.A. Somorjai, *Surf. Sci.* **180**, 433 (1987).
28. T. Aizawa, Y. Hwang, W. Hayami, R. Souda, S. Otani, and Y. Ishizawa, *Surf. Sci.* **260**, 311 (1992).
29. T. A. Land, T. Michely, R. J. Behm, J. C. Hemminger, and G. Comsa, *Surf. Sci.* **264**, 261 (1992).
30. M. Sasaki, Y. Yamada, Y. Ogiwara, S. Yagyu, and S. Yamamoto, *Phys. Rev. B* **61**, 15653 (2000).
31. B. Lang, *Surf. Sci.* **53**, 317 (1975).
32. P.W. Sutter, J.I. Flege, E.A. Sutter, *Nat. Mater* **7**, 406 (2008).
33. M. C. Wu, Q. Xu, D. W. Goodman, *J. Phys. Chem. B* **98**, 5104 (1994).
34. S. Marchini, S. Günther, J. Wintterlin, *Phys. Rev. B*, **76**, 075429 (2007).
35. A.L. Vázquez de Parga, F. Calleja, B. Borca, M.C.G. Passeggi, Jr., J.J. Hinarejo, F. Guinea, R. Miranda, *Phys. Rev. Lett.* **100**, 056807 (2008).

References

36. X. Li, W. Cai, J. An, S. Kim, J. Nah, D. Yang, R. Piner, A. Velamakanni, I. Jung, E. Tutuc, S.K. Banerjee, L. Colombo, R.S. Ruoff, *Science* **324**, 1312 (2009).
37. S. Bae, H. Kim, Y. Lee, X. Xu, J.-S. Park, Y. Zheng, J. Balakrishnan, T. Lei, H. R. Kim, Y. I. Song, Y.-J. Kim, K. S. Kim, B. Özyilmaz, J.-H. Ahn, B. H. Hong, and S. Iijima, *Nature Nanotechnol.* **5**, 574 (2010).
38. D.G. Castner, B.A. Sexton, G.A. Somorjai, *Surf. Sci.* **71**, 519 (1978).
39. C. F. McConville, D. P. Woodruff, and S. D. Kevan, *Surf. Sci.* **171**, L447 (1986).
40. L. Papagno, M. Conti, L.S. Caputi, J. Anderson, and G.J. Lapeyre, *Surf. Sci.* **219**, L565 (1989).
41. T. Aizawa, R. Souda, Y. Ishizawa, H. Hirano, T. Yamada, and K. Tanaka, *Surf. Sci.* **237**, 194 (1990).
42. A. Nagashima, N. Tejima, and C. Oshima, *Phys. Rev. B* **50**, 17487 (1994).
43. A. M. Shikin, D. Farías, and K. H. Rieder, *Euro phys. Lett.* **44**, 44 (1998).
44. A.M. Shikin, D. Farías, V.K. Adamchuk, and K.-H. Rieder, *Surf. Sci.* **424**, 155 (1999).
45. D. Farías, A. M. Shikin, K.-H. Rieder and Yu. S. Dedkov, *J. Phys.: Condens. Matter* **11**, 8453 (1999).
46. A. M. Shikin, G. V. Prudnikova, V. K. Adamchuk, F. Moresco, and K.-H. Rieder, *Phys. Rev. B* **62**, 13202 (2000).
47. Y. S. Dedkov, A. M. Shikin, V. K. Adamchuk, S. L. Molodtsov, C. Laubschat, A. Bauer, and G. Kaindl, *Phys. Rev. B* **64**, 035405 (2001).
48. A. Varykhalov, J. Sánchez-Barriga, A. M. Shikin, C. Biswas, E. Vescovo, A. Rybkin, D. Marchenko and O. Rader, *Phys. Rev. Lett.* **101**, 157601 (2008).
49. K. S. Kim, Y. Zhao, H. Jang, S. Y. Lee, J. M. Kim, K. S. Kim, J.-H. Ahn, P. Kim, J.-Y. Choi, and B. H. Hong, *Nature* **457**, 706 (2009).
50. A. Reina, X. Jia, J. Ho, D. Nezich, H. Son, V. Bulovic, M.S. Dresselhaus, J. Kong, *Nano Lett.* **9**, 30 (2009).
51. A. J. Van Bommel, J. E. Crombeen, and A. Van Tooren, *Surf. Sci.* **48**, 463 (1975).
52. L. Simon, J. L. Bishop, L. Kubler, *Phys. Rev. B* **16**, 11653 (1999).

References

53. K. V. Emtsev, F. Speck, Th. Seyller, and L. Ley, *Phys. Rev. B* **77**, 155303 (2008).
54. X. Wu, Y. Hu, M. Ruan, N. K. Madiomanana, J. Hankinson, M. Sprinkle, C. Berger, and W. A. de Heer, *Appl. Phys. Lett.* **95**, 223108 (2009).
55. M. Orlita, C. Faugeras, P. Plochocka, P. Neugebauer, G. Martinez, D. K. Maude, A. -L. Barra, M. Sprinkle, C. Berger, W. A. de Heer, and M. Potemski, *Phys. Rev. Lett.* **101**, 267601 (2008).
56. M. Sprinkle, D. Siegel, Y. Hu, J. Hicks, A. Tejada, A. Taleb-Ibrahimi, P. Le Fèvre, F. Bertran, S. Vizzini, H. Enriquez, S. Chiang, P. Soukiassian, C. Berger, W. A. de Heer, A. Lanzara, and E. H. Conrad, *Phys. Rev. Lett.* **103**, 226803 (2009).
57. Th. Seyller, A. Bostwick, K. V. Emtsev, K. Horn, L. Ley, J. L. McChesney, T. Ohta, J. D. Riley, E. Rotenberg, and F. Speck, *Phys. Stat. Sol. B* **245**, 1436 (2008).
58. C. Berger, Z. Song, T. Li, X. Li, A. Y. Ogbazghi, R. Feng, Z. Dai, A. N. Marchenkov, E. H. Conrad, P. N. First, and W. A. de Heer, *J. Phys. Chem. B* **108**, 19912 (2004).
59. I. Forbeaux, J.-M. Themlin and J.-M. Debever, *Phys. Rev. B* **58**, 16396 (1998).
60. A. Bostwick, T. Ohta, J. L. McChesney, K. V. Emtsev, T. Seyller, K. Horn, and E. Rotenberg, *New J. Phys.* **9**, 385 (2007).
61. C. Riedl, U. Starke, J. Bernhardt, M. Franke, and K. Heinz, *Phys. Rev. B* **76**, 245406 (2007).
62. P. Mallet, F. Varchon, C. Naud, L. Magaud, C. Berger, and J.-Y. Veillen, *Phys. Rev. B* **76**, 041403(R) (2007).
63. A. Bostwick, T. Ohta, T. Seyller, K. Horn, and E. Rotenberg, *Nature Phys.* **3**, 36 (2007).
64. T. Ohta, A. Bostwick, T. Seyller, K. Horn, and E. Rotenberg, *Science* **313**, 951 (2006).
65. S. Y. Zhou, G.-H. Gweon, A. V. Fedorov, P. N. First, W. A. de Heer, D.-H. Lee, F. Guinea, A. H. Castro Netto, and A. Lanzara, *Nature Mater.* **6**, 770 (2007).
66. C. Riedl, C. Coletti, T. Iwasaki, A. A. Zakharov, and U. Starke, *Phys. Rev. Lett.* **103**, 246804 (2009).

References

67. F. Banhart, J. Kotakoski, and A. V. Krashennnikov, *ACS Nano* **5**, 8442 (2011).
68. N. Emery, C. Herold, M. d'Astuto, V. Garcia, C. Bellin, J. F. Mareche, P. Lagrange, and G. Loupiau, *Phys. Rev. Lett.* **95**, 087003 (2005).
69. T. Weller, M. Ellerby, S. Saxena, R. Smith, and N. Skipper, *Nat. Phys.* **1**, 39 (2005).
70. T. Valla, J. Camacho, Z.-H. Pan, A.V. Fedorov, A. C. Walters, C. A. Howard, and M. Ellerby, *Phys. Rev. Lett.* **102**, 107007 (2009).
71. M. Bianchi, E. D. L. Rienks, S. Lizzit, A. Baraldi, R. Balog, L. Hornekær and Ph. Hofmann, *Phys. Rev. B.* **81**, 041403R (2010).
72. L. Meng, R. Wu, H. Zhou, G. Li, Yi Zhang, L. Li, Y. Wang, and H.-J. Gao, *Appl. Phys. Lett.* **100**, 083101 (2012).
73. R. Larciprete, S. Ulstrup, P. Lacovig, M. Dalmiglio, M. Bianchi, F. Mazzola, L. Hornekær, F. Orlando, A. Baraldi, P. Hofmann, and S. Lizzit, *ACS Nano* **6** (11), 9551 (2012).
74. A. M. Shikin, V. K. Adamchuk, and K.-H. Rieder, *Phys. Solid State* **51**, 2390 (2009).
75. A. G. Starodubov, M. A. Medvetski, A. M. Shikin, and V. K. Adamchuk, *Phys. Solid State* **46**, 1340 (2004).
76. J. Sánchez-Barriga, A. Varykhalo, M.R. Scholz, O. Rader, D. Marchenko, A. Rybkin, A.M. Shikin, E. Vescovo, *Diamond & Related Materials* **19**, 734 (2010).
77. J. Coraux, A. T. N'Diaye, N. Rougemaille, C. Vo-Van, A. Kimouche, H.-X. Yang, M. Chshiev, N. Bendiab, O. Fruchart, A. K. Schmid, *J. Phys. Chem. Lett.* **3**, 2059 (2012).
78. N. Rougemaille, A. T. N'Diaye, J. Coraux, C. Vo-Van, O. Fruchart, and A. K. Schmid, *Appl. Phys. Lett.* **101**, 142403 (2012).
79. S. Rusponi, M. Papagno, P. Moras, S. Vlaic, M. Etzkorn, P. M. Sheverdyaeva, D. Pacile, H. Brune, C. Carbone, *Phys. Rev. Lett.* **105**, 246803 (2010).
80. J.-H. Chen, C. Jang, S. Xiao, M. Ishigami, and M. S. Fuhrer, *Nat. Nano* **3**, 206 (2008).

References

81. A. Sandin, T. Jayasekera, J. E. Rowe, Ki. W. Kim, M. B. Nardelli, and D. B. Dougherty, *Phys. Rev. B* **85**, 125410 (2012).
82. A. L. Walter, K.-J. Jeon, A. Bostwick, F. Speck, M. Ostler, T. Seyller, L. Moreschini, Y. S. Kim, Y. J. Chang, K. Horn, and E. Rotenberg, *Appl. Phys. Lett.* **98**, 184102 (2011).
83. B. Premlal, M. Cranney, F. Vonau, D. Aubel, D. Casterman, M. M. DeSouza, and L. Simon, *Appl. Phys. Lett.* **94**, 263115 (2009).
84. I. Gierz, T. Suzuki, R. T. Weitz, D. S. Lee, B. Krauss, C. Riedl, U. Starke, H. Hochst, J. H. Smet, C. R. Ast, and K. Kern, *Phys. Rev. B* **81**, 235408 (2010).
85. C. Virojanadara, A. A. Zakharov, S. Watcharinyanon, R. Yakimova, and L. I. Johansson, *New J. Phys.* **12**, 125015 (2010).
86. C. Virojanadara, S. Watcharinyanon, A. A. Zakharov, and L. I. Johansson, *Phys. Rev. B* **82**, 205402 (2010).
87. K. V. Emtsev, A. A. Zakharov, C. Coletti, S. Forti, and U. Starke, *Phys. Rev. B* **84**, 125423 (2011).
88. I. Gierz, C. Riedl, U. Starke, C. R. Ast, and K. Kern, *Nano Lett.* **8**, 4603 (2008).
89. J. L. McChesney, A. Bostwick, T. Ohta, T. Seyller, K. Horn, J. Gonzalez, and E. Rotenberg, *Phys. Rev. Lett.* **104**, 136803 (2010).
90. Z. -H. Pan, J. Camacho, M. H. Upton, A. V. Fedorov, C. A. Howard, M. Ellerby, and T. Valla, *Phys. Rev. Lett.* **106**, 187002 (2011).
91. M. Xue, G. Chen, H. Yang, Y. Zhu, D. Wang, J. He, and T. Cao, *J. Am. Chem. Soc.* **134**, 6536 (2012).
92. L. A. Ponomarenko, F. Schedin, M. I. Katsnelson, R. Yang, E. W. Hill, K. S. Novoselov and A. K. Geim, *Science* **320** (5874), 356 (2008).
93. G. Binnig, H. Rohrer, Ch. Gerber, *Phys. Rev. Lett.* **50**, 120 (1983).
94. D. Bonnell, *Scanning Tunneling Microscopy and spectroscopy: Theory, techniques and applications*, Wiley (1993)
95. L. Peterson, *Scanning Tunneling Microscopy studies of electronic structure of of Metal surfaces*. PhD thesis, University of Aarhus, Denmark (1999).

References

96. J. Tersoff and D.R. Hamann, Phys. Rev. Lett. **50**, 1998 (1983).
97. C. J. Chen, Introduction to Scanning Tunneling Microscopy, (Oxford University Press) (1993).
98. J.A. Stroscio and W. J. Kaiser, Scanning Tunneling Microscopy, Academic Press, San Diego (1993).
99. S. Hüfner, Photoelectron Spectroscopy: Principles and applications, Springer-Verlag, Berlin (1995).
100. S. Hüfner and F. Reinert, New J. Phys. **7**, 97 (2005).
101. C. N. Berglund and W. E. Spicer, Phys. Rev. **136**, 1030 (1964).
102. A. Damascelli, Z. Hussain, and Z.-X. Shen, Rev. Mod. Phys. **75**, 473 (2003).
103. Synchrotron Soleil Paris www.synchrotron-soleil.fr/
104. T. Owen, Fundamentals of modern UV-Visible spectroscopy (2000).
105. B. Valeur, Molecular Fluorescence: Principles and Applications, Wiley (2001).
106. M. Göppert-Mayer, Ann. Phys. **401**, 273 (1931).
107. W. Kaiser, C. G. B. Garrett, Phys. Rev. Lett. **7**, 229 (1961).
108. Y. R. Shen, The Principles of Non Linear Optics; Wiley-VCH Verlag GmbH: New York (1984).
109. B. J. Orr, J. F. Ward, Mol. Phys. **20**, 513 (1971).
110. M.Rumi, J. E. Ehrlich, A. Heikal, J. W. Perry, S. Barlow, Z. Y. Hu, McCord-Maughon, D. Parker, T. C. H. Rockel, S. Thayumanavan, S. R. Marder, D. Beljonne, J. L. Brédas, J. Am. Chem. Soc. **122**, 9500 (2000).
111. C. Xu, W.W. Webb, J. Opt. Soc. Am. B **13**, 481 (1996).
112. J. Kedzierski, P.-L. Hsu, P. Healey, P. W. Wyatt, C. L. Keast, M. Sprinkle, C. Berger, W. A. de Heer, IEEE Trans. Electron Devices **55**, 2078 (2008).
113. G. Gu, S. Nie, R. M. Feenstra, R. P. Devaty, W. J. Choyke, W. K. Chan, and M. G. Kane, Appl. Phys. Lett. **90**, 253507 (2007).
114. M. Seul and D. Andelman, Science **267** (1995).
115. G. M. Rutter, J. N. Crain, N. P. Guisinger, P. N. First, and J. A. Stroscio, J. Vac. Sci. Technol. A **26**, 938 (2008).

References

116. P. Lauffer, K. V. Emtsev, R. Graupner, Th. Seyller, L. Ley, S. A. Reshanov and H. B. Weber, *Phys. Rev. B* **77** 155426 (2008).
117. C. Weeks, J. Hu, J. Alicea, M. Franz, and R. Wu, *Phys. Rev. X* **1**, 021001 (2011).
118. C. Riedl, C. Coletti, U. Starke, *J. Phys. D: Appl. Phys.* **43**, 374009 (2010).
119. W. Lu, W.C. Mitchel, J.J. Boeckl, T. R. Crenshaw, W.E. Collins, R.P.H. Chang, and L.C. Feldman, *J. Electron. Mater.* **38**, 6, 731 (2009).
120. M.H. Oliveira Jr., T. Schumann, F. Fromm, R. Koch, M. Ostler, M. Ramsteiner, Th. Seyller, J. M. J. Lopes, H. Riechert, *Carbon* **52**, 83 (2013).
121. D. Stoltz, S. E. Stoltz and L. S. O. Johansson, *J. Phys.: Condens. Matter* **19**, 266006 (2007).
122. C. Virojanadara, L.I. Johansson, *Surf. Sci.* **600**, 436 (2006).
123. J.H. Park, W.C. Mitchel, H.E. Smith, L. Grazulis, K.G. Eyink, *Carbon* **48** 1670 (2010).
124. Y. Kitsudo, A. Iwamoto, H. Matsumoto, K. Mitsuhara, T. Nishimura, M. Takizawa, T. Akita, Y. Maeda, Y. Kido, *Surf. Sci.* **603**, 2108 (2009).
125. H.-G. Boyen, A. Ethirajan, G. Kastle, F. Weigl, and P. Ziemann, *Phys. Rev. Lett.* **94**, 016804 (2005).
126. M. Buttner and P. Oelhafen, *Surf. Sci.* **600** 1170 (2006).
127. T. Bhuvana G. V. Pavan Kumar, C. Narayana and G. U. Kulkarni, *Nanotechnology* **18**, 145702 (2007).
128. M. Cranney, F. Vonau, P. B. Pillai, E. Denys, D. Aubel, M. M. De Souza, C. Bena, and L. Simon, *Europhys. Lett.* **91**, 66004 (2010).
129. P. T. Sprunger, L. Petersen, E. W. Plummer, E. Lægsgaard and F. Besenbacher, *Science* **275**, 1764 (1997).
130. L. Simon, F. Vonau and D. Aubel, *J. Phys.: Condens. Matter.* **19**, 355009 (2007).
131. K. McElroy, R. W. Simmonds, J. E. Hoffman, D-H. Lee, J. Orenstein, H. Eisaki, S. Uchida and J. C. Davis, *Nature* **422**, 592 (2003).
132. F. Vonau, D. Aubel, G. Gewinner, S. Zabrocki, J. C. Peruchetti, D. Bolmont and L. Simon, *Phys. Rev. Lett.* **95**, 176803 (2005).

References

133. G. M. Rutter, J. N. Crain, N. P. Guisinger, T. Li, P. N. First and J. A. Stroscio, *Science* **317**, 219 (2007).
134. I. Brihuega, P. Mallet, C. Bena, S. Bose, C. Michaelis, L. Vitali, F. Varchon, L. Magaud, K. Kern and J.Y. Veuillen, *Phys. Rev. Lett.* **101**, 206802 (2008).
135. L. Simon, C. Bena, F. Vonau, D. Aubel, H. Nasrallah, M. Habar and J. C. Peruchetti *Eur. Phys. J. B* **69**, 351(2009).
136. Supplementary information:
<http://www.is2m.uha.fr/index.php?langue=fr&it1=rec&it2=po3&it3=eq7>
137. R. Grassi, T. Low, and M. Lundstrom, *Nano Lett.* **11**, 4574 (2011).
138. M. N. Nair, M. Cranney, F. Vonau, D. Aubel, P. L. Fevre, A. Tejada, F. Bertran, A. Taleb-Ibrahimi and L. Simon, *Phys. Rev. B* **85**, 254421 (2012).
139. T. Weller, M. Ellerby, S. Saxena, R. Smith, and N. Skipper, *Nat. Phys.*, **1**,39 (2005).
140. M. Xue, T. Cao, D. Wang, Y. Wu, H. Yang, S. Dong, J. He, F. Li and G. F. Chen, *Sci. Rep.* **2**, 389 (2012).
141. G. Profeta, M. Calandra, and F. Mauri, *Nat. Phys.* **8**, 131 (2012).
142. O. Vafek, *Nat. Phys.* **8**, 111 (2012).
143. R. S. Markiewicz, *J. Phys. Chem. Solids* **58**, 1179 (1997).
144. R. Nandkishore, L. S. Levitov, A. V. Chubukov, *Nat. Phys.* **8**,158 (2012).
145. K. C. Rahnejat, C. A. Howard, N. E. Shuttleworth, S. R. Schofield, K. Iwaya, C. F. Hirjibehedin, Ch. Renner, G. Aeppli, and M. Ellerby, *Nat. Commun.* **2**, 558 (2011).
146. M. Calandra and F. Mauri, *Phys. Rev. B* **76**, 161406(R) (2007).
147. C.-H. Park, L. Yang, Y.-W. Son, M. L. Cohen, and S. G. Louie, *Nat. Phys.* **4**, 213 (2008).
148. C. Bena and L. Simon, *Phys. Rev. B* **83**, 115404 (2011).
149. G. Li, A. Luican, J. M. B. Lopes dos Santos, A. H. Castro Neto, A. Reina, J. Kong, and E. Y. Andrei, *Nat. Phys.* **6**, 109 (2010).
150. T. Valla and Z. Pan, Superconductivity and electron phonon coupling in graphite intercalation compounds, *Physics and applications of Graphene-Experiments*, Dr. S. Mikhailov (Ed.), InTech (2011).

References

151. G. Grimvall, *The Electron-phonon interaction in metals*, North-Holland, New York (1981).
152. J. Shi, S.-J. Tang, B. Wu, P.T. Sprunger, W. L. Yang, V. Brouet, X. J. Zhou, Z. Hussain, Z.-X. Shen, Z. Zhang, and E.W. Plummer, *Phys. Rev. Lett.* **92**, 186401 (2011).
153. A. A. Kordyuk, S. V. Borisenko, A. Koitzsch, J. Fink, M. Knupfer and H. Berger, *Phys. Rev. B* **71**(21): 214513 (2005).
154. R.C. Dynes, *Solid state communications* **10**, 615 (1972).
155. F. Marsiglio, J.P. Carbotte, *Superconductivity* (2008).
156. W.W. Fuller-Mora, S.A. Wolf, V.Z. Kresin, *J. Supr. Cond.* **7**, 3 (1994).
157. N. W. Ashcroft and N.D. Mermin, *Solid state physics*, Saunders College (1976).
158. A. Gorgues, P. Hudhomme, M. Salle, *Chem. Rev.* **104**, 5151(2004).
159. J. L. Segura, N. Martín, *Angew. Chem. Int. Ed.* **40**, 1372 (2001).
160. M. Bendikov, F. Wudl, D. F. Perepichka, *Chem. Rev.* **104**, 4891 (2004).
161. N. Martín, *Chem. Commun.* **49**, 7025 (2013).
162. M. Gonzalez, J. L. Segura, C. Seoane, N. Martín, J. Garín, J. Orduna, B. Villacampa, R. Alcalá, V. Hernandez and J. T. Lopez Navarrete, *J. Org. Chem.* **66**, 8872 (2001).
163. J-I. Yamada, H. Akutsu, H. Nishikawa and K. Kikuchi, *Chem. Rev.* **104**, 5057 (2004).
164. D. Choudhury, B. Das, D.D. Sarma, C.N.R. Rao, *Chem. Phys. Lett.* **497**, 66 (2010).
165. R. Voggu, B. Das, C Sekhar Rout and C. N. R. Rao, *J. Phys.: Condens. Matter.* **20**, 472204 (2008).
166. J. T. Sun, Y. H. Lu, W. Chen, Y. P. Feng, and A. T. S. Wee, *Phys. Rev. B* **81**, 155403 (2010).
167. T. C. Leung, C. L. Kao, W. S. Su, Y. J. Feng and C.T. Chan, *Phy. Rev. B* **68**, 195408 (2003).
168. S-Long Lee, Yi-Chen, H-Jen Wu and C-H Chen, *Langmuir* **28**, 382 (2012).

References

169. M. M. S. Abdel-Mottaleb, E. G. Nadal, M. Surin, H. Uji-I, W. Mamdouh, J. Veciana, V. Lemaury, C. Rovira, J. Cornil, R. Lazzaroni, D. B. Amabilino, S. De Feyter and F. C. De Schryver, *J. Mater. Chem.* **15**, 4601 (2005).
170. J. Puigmartí-Luis, A. Minoia, S. Lei, V. Geskin, B. Li, R. Lazzaroni, S. De Feyter, and D. B. Amabilino, *Chem. Sci.* **2**, 1945 (2011).
171. H. Inokuchi, G. Saito, P. Wu, K. Seki, T. B. Tang, T. Mori, K. Imaeda, T. Enoki, Y. Higuchi, K. Inaka, and N. Yasuoka, *Chem. Lett.* 1263 (1986).
172. M. Irie, *Chem. Rev.* **100**, 1685 (2000).
173. S. Kobatake, K. Uchida, E. Tsuchida, M. Irie, *Chem. Comm.* **23**, 2804 (2002).
174. R. B. Woodward and R. Hoffmann, *J. Am. Chem. Soc.* **87**, 395 (1965).
175. R. Shokri, M.-A. Lacour, T. Jarrosson, J.-P. Lère-Porte, F. Serein-Spirau, K. Miqueu, J.-M. Sotiropoulos, F. Vonau, D. Aubel, M. Cranney, G. Reiter, L. Simon, *J. Am. Chem. Soc.* **135**, 5693 (2013).
176. N. Katsonis et al., *J. Am. Chem. Soc.* **130**, 386 (2008).
177. R. Arai et al., *J. Am. Chem. Soc.* **130**, 9371 (2008).
178. N. Katsonis et al., *Adv. Mater.* **18**, 1397 (2006).
179. S.V. Snegir et al., *J. Phys. Chem. Lett.* **2**, 2433 (2011).
180. Z.-G. Zhang, S. Zhang, J. Min, C. Chui, J. Zhang, M. Zhang, Y. Li, *Macromolecules* **45**, 113 (2012).
181. A. Facchetti, M. Mushrush, H. E. Katz, T. J. Marks, *Adv. Mater.* **15**, 33 (2003).
182. S. Sumalekshmy, C. J. Fahrni, *Chem. Mater.* **23**, 483 (2011).
183. Y. Morel, A. Irimia, P. Najechalski, Y. Kervella, O. Stephan, P. L. Baldeck, C. Andraud, *J. Chem. Phys.* **114**, 5391(2001).
184. J. E. Ehrlich, W. L. Wu, I.-Y. S. Lee, Z.-Y. Hu, H. Röckel, S. R. Marder, and J. W. Perry, *Opt. Lett.* **22**, 1843 (1997).
185. W. H. Zhou, S. M. Kuebler, K. L. Braun, T. Y. Yu, J. K. Cammack, C. K. Ober, J. W. Perry, and S. R. Marder, *Science* **296**, 1106 (2002).
186. B. H. Cumpston, S. P. Ananthavel, S. Barlow, D. L. Dyer, J. E. Ehrlich, L. L. Erskine, A. A. Heikal, S. M. Kuebler, I. Y. S. Lee, D. McCord-Maughon,

References

- J. Q. Qin, H. Rockel, M. Rumi, X. L. Wu, S. R. Marder, and J. W. Perry, *Nature* **398**, 51 (1999).
187. W. Denk, J. H. Strickler, W. Webb, *Science* **248**, 73 (1990).
188. R. Xia, J.-P. Malval, M. Jin, A. Spangenberg, D. Wan, H. Pu, T. Vergote, F. Morlet-Savary, H. Chaumeil, P. Baldeck, O. Poizat, O. Soppera, *Chem. Mater.* **24**, 237 (2012).
189. S. Kawata, H. B. Sun, T. Tanaka, and K. Takada, *Nature* **412**, 697 (2001).
190. H. -B. Sun, S. Kawata, *Two-Photon Photo polymerization and 3D Lithographic Micro fabrication*; Springer-Verlag ed. Berlin, **170** (2004).
191. A. Spangenberg, J.-P. Malval, H. Akdas-Kilig, J.-L. Fillaut, F. Stehlin, N. Hobeika, F. Morlet-Savary, O. Soppera, *Macromolecules* **45** (3), 1262 (2012).
192. J.-P. Malval, M. Jin, F. Morlet-Savary, H. Chaumeil, A. Defoin, O. Soppera, T. Scheul, M. Bouriau, P. L. Baldeck, *Chem. Mater.* **23**, 3411 (2011).
193. M. Williams-Harry, A. Bhaskar, G. Ramakrishna, T. Goodson, M. Imamura, A. Mawatari, K. Nakao, H. Enozawa, T. Nishinaga, M. Iyoda, *J. Am. Chem. Soc.* **130**, 3252 (2008).
194. H. Rath, J. Sankar, V. PrabhuRaja, T.K. Chandrasekhar, A. Nag, D. Goswami, *J. Am. Chem. Soc.* **127**, 11608 (2005).
195. H. Kuhn, C Kuhn, *Chem. Phys. Lett.* **204**, 206 (1993).
196. H. Kuhn, *J. Chem. Phys.* **17**, 1198 (1949).
197. L. O'Neill, H. J. Byrne, *J. Phys. Chem. B* **109**, 12685 (2005).
198. S. Aloise, Z. Pawlowska, C. Ruckebusch, M. Sliwa, J. Dubois, O. Poizat, G. Buntinx, A. Perrier, F. Maurel, P. Jacques, J.-P. Malval, L. Poisson, G. Abe Piani, *J. Phys. Chem. Chem. Phys.* **14**, 1945 (2012).
199. A. Facchetti, M.-H. Yoon, C. L. Stern, G. R. Hutchison, M. A. Ratner, T. J. Marks, *J. Am. Chem. Soc.* **126**, 13480 (2004).
200. Y. Sakamoto, S. Komatsu, T. Suzuki, *J. Am. Chem. Soc.* **123**, 4643 (2001).
201. R. S. Becker, J. Seixas de Melo, A. L. Maçanita, F. Elisei, *J. Phys. Chem.* **100**, 18683 (1996).

References

202. I. L. Zheldakov, J. M. Wasylenko, C. G. Elles, *Phys. Chem. Chem. Phys.* **14**, 6211 (2012).
203. J. S. de Melo, L. M. Silva, L. G. Arnaut, R. S. Becker, *J. Chem. Phys.* **111**, 5427 (1999).
204. J. S. de Melo H. D. Burrows, M. Svensson, M. R. Andersson, A. P Monkman, J. *Chem. Phys.* **118**, 1550 (2003).
205. J. Gierschner, H. G. Mack, H. J. Egelhaaf, S. Schweizer, B. Doser, D. Oelkrug, *Synth. Met.* **138**, 311(2003).
206. G. Lanzani, M. Nisoli, S. De Silvestri, R. Tubino, *Chem. Phys. Lett.* **251**, 339 (1996).
207. M. Belletête, N. Di Césare, M. Leclerc, G. Durocher, *Chem. Phys. Lett.* **250**, 31 (1996).
208. J. Pina, J. S Seixas de Melo, *Phys. Chem. Chem. Phys.* **11**, 8706 (2009).
209. G. Macchi, B. M. Medina, M. Zambianchi, R. J. Tubino, G. CornilBarbarella, J. Gierschner, F. Meinardi, *Phys. Chem. Chem. Phys.* **11**, 984 (2009).
210. S. J. Strickler, R. A. Berg, *J. Chem. Phys.* **37**, 814 (1962).
211. I. B. Berlman, O. J. Steingraber, *J. Chem. Phys.* **43**, 2140 (1965).
212. I. B. Berlman, *J. Chem. Phys.* **52**, 5616 (1970).
213. J. B. Birks, *Photophysics of Aromatic Molecules*; Wiley-Interscience: New York, 1970.
214. M. Jin, J. P. Malval, D. L. Versace, F. Morlet-Savary, H. Chaumeil, A. Defoin, X. Allonas. J. P. Fouassier, *Chem. Comm.* **48**, 6540 (2008).
215. K. D. Belfield, M. V. Bondar, F. E. Hernandez, O. V. Przhonska, S. Yao, *J. Phys. Chem. B* **111**, 12723 (2007).